UNIVERSIDAD DE LA REPÚBLICA
FACULTAD DE INGENIERÍA

Modelling and analysis of neurons coupled by electrical synapses

TESIS PRESENTADA A LA FACULTAD DE INGENIERÍA DE LA
UNIVERSIDAD DE LA REPÚBLICA POR

Federico Davoine

EN CUMPLIMIENTO PARCIAL DE LOS REQUERIMIENTOS
PARA LA OBTENCIÓN DEL TÍTULO DE
MAGÍSTER EN INGENIERÍA ELÉCTRICA.

DIRECTORES DE TESIS
Dr. Pablo Monzón ...... Facultad de Ingeniería, Universidad de la República
Dr. Sebastián Curti ...... Facultad de Medicina, Universidad de la República

TRIBUNAL
Dr. Fernando Silveira ... Facultad de Ingeniería, Universidad de la República, Uruguay
Dr. Federico Lecumberry Facultad de Ingeniería, Universidad de la República, Uruguay
Dr. Ruben Budelli .... Facultad de Ciencias, Universidad de la República, Uruguay
Dr. Juan Carlos Martínez .. Centro de Investigación y de Estudios Avanzados del Instituto Politécnico Nacional, México

DIRECTOR ACADÉMICO
Dr. Pablo Monzón ...... Facultad de Ingeniería, Universidad de la República

Montevideo
Tuesday 4th March, 2014

Agradecimientos

Esta sección es la más complicada de escribir, dado que no es fácil (al menos para mí) plasmar en papel nombres (excluyendo otros, por simple descuido) y agradecimientos (que siempre quedan cortas o mal expresadas).

Quiero agradecer a:

la Agencia Nacional de Innovación e Investigación, por haberme apoyado con una beca de maestría,

mis orientadores de tesis, Sebastián Curti y Pablo Monzón por haber creído en que este trabajo interdisciplinario era posible y apoyarme a lo largo del mismo. Era arriesgado apostar a esta nueva experiencia, dado que hay pocos antecedentes de estudiantes de la maestría en ingeniería eléctrica realizando modelado en neurociencias. Espero que la contribuciones de esta tesis estén a la altura de las expectativas y que permitan seguir nuevas líneas de trabajo,

Ricardo Marotti, quien me enseñó mucho acerca del trabajo científico y con quien publiqué mi primer artículo en revista,

Antonio Roque, por darme la oportunidad de participar en la escuela latinoamericana en neurociencia computacional, que significó un cambio cualitativo en mi trabajo

mis compañeros y amigos de fing, en particular a Gabriel Eirea, Cecilia Stari, Amelia Ferrari y al megagrupo de la sala 10-extendida, por tener la (des)dicha de contar con mi presencia a diario,

mis amigos que viven lejos, en especial a los rioplatenses de la LASCON y a los de La Plata Bassin,

Maggie, Noe, Fer, Vale, Ceci, Javi, Leandro y dd, por lograr mantener amistades invariantes en el tiempo

mis padres y mi hermano, muy especialmente, por apoyarme durante todos estos años.

This page has been intentionally left blank

Resumen

El objetivo de esta tesis es analizar el rol de las propiedades intrínsecas de las neuronas en la comunicación a través de sinapsis eléctricas. Las neuronas del nervio trigeminal del mesencéfalo constituyen un excelente modelo experimental para estudiar la comunicación entre neuronas, debido a su fácil acceso experimental y su sencilla morfología. Sin embargo, el análisis de neuronas reales está limitado por restricciones experimentales que impiden explorar todos los aspectos del modelo.

En el marco de esta tesis, se construye un modelo matemático basado en registros electrofisiológicos realizados por Sebastián Curti en la Facultad de Medicina de la Universidad de la República. El modelo consiste en un sistema de ecuaciones diferenciales, que puede ser representado por un circuito eléctrico con componentes no lineales. Algunas de las ecuaciones diferenciales son obtenidas de bibliografía y se realizan algunos ajustes menores de parámetros. Por otro lado, durante la tesis evaluamos que se necesitaba más información para reproducir algunas de las características más importantes del comportamientos de las neuronas, como la duración del potencial de acción. Por eso, se debieron realizar nuevos registros experimentales, que permitieron refinar el modelo.

El modelo permite evaluar la respuesta de la neurona ante diferentes estímulos (corrientes o voltajes impuestos por un electrodo), posibilitando nuevos "experimentos" que no son posibles en un laboratorio. Se analizan diversas alternativas de modelado (variando corrientes iónicas y morfología) usando información experimental para validarlos. Luego, el modelo es utilizado para entender algunas características inusuales de la comunicación entre neuronas. En primer lugar, se estudia la transferencia subumbral (i.e.: sin potenciales de acción) entre neuronas acopladas por sinapsis eléctricas. Se utiliza un modelo reducido, que es linealizado para obtener una expresión analítica de la transferencia, cuyo comportamiento es coherente con los resultados experimentales. Asimismo, se realizan simulaciones numéricas para analizar el rol en la sincronización de las propiedades intrínsecas de las neuronas. Se muestra que las mismas propiedades que determinan el comportamiento subumbral son relevantes para mejorar la sincronización entre neuronas. Finalmente, esta tesis no sólo contribuye con nuevos modelos y respuestas, sino con nuevas preguntas, que deberán ser estudiadas usando modelos experimentales también.

Esta tesis hace uso de diversas herramientas utilizadas por la ingeniería eléctrica

(comportamiento en frecuencia de sistemas, ecuación del cable, cadenas de Markov, algoritmos evolutivos, etc) para modelar y analizar un sistema biológico. Se realizan diversos aportes, por ejemplo: modelado completo de las corrientes de sodio, así como de la modulación de otra corriente; explicación de la preferencia en frecuencia de la transferencia subumbral entre neuronas; estudio de la sincronización en función de las propiedades de los osciladores y de su acople.

Algunos resultados preliminares de este trabajo han sido presentados en congresos internacionales.

Abstract

The objective of this thesis is to analyze the role of the intrinsic properties of neurons in the communication through electrical synapses. Mesencephalic trigeminal neurons constitute an excellent experimental model to study the communication between neurons, because of its easy experimental access experimental and simple morphology. However, the analysis of real neurons is limited by experimental constraints that do not allow to explore all aspects of the model.

Within the context of this thesis, a mathematical model is built, based on electrophysiological recordings made by Sebastian Curti at the School of Medicine of Universidad de la República. The model consists of a set of differential equations, which can be represented by a nonlinear electrical circuit. Some of the differential equations are obtained from literature and only some minor parameters' adjustments are made. Moreover, during the thesis we have found that more data was needed in order to explain some of the most important features of the behavior of neurons, such as the duration of the action potential. Therefore, more experimental recordings were made, allowing to refine the model.

The model allows to evaluate the response of the neuron to different stimuli (currents or voltages imposed by an electrode), making possible to make new "experiments" that are not possible in a laboratory. Alternatives models are analyzed (varying ionic currents and morphology) using experimental information to validate them. Then the model is used to understand some unusual features of the communication between neurons. First, it is studied the subthreshold transfer function (i.e. without action potentials) between neurons coupled by electrical synapses. A reduced model is used and then linearized, in order to derive an analytical expression of the transfer function, whose behaviour is consistent with experimental results. Moreover, numerical simulations are performed to analyze the rol of the intrinsic properties of neurons in their synchronization. It is shown that the same properties that determine the subthreshold behavior are relevant to improve synchronization between neurons too. Finally, this thesis contributes not only with new models and answers, but with new questions, which should be studied using experimental models as well.

This thesis applies several tools used for electrical engineering (frequency response of systems, cable equation, Markov chains, evolutionary algorithms, etc.)

to model and analyze a biological system. Among the contributions of this thesis are: the complete modeling of the sodium currents and other ionic current (and its modulation); the explanation preference subthreshold frequency transfer between neuronfor example and its coupling.

Some preliminary results of this work have been presented at international conferences.

Contents

Contents

This page has been intentionally left blank

Chapter 1

Introduction

1.1 Motivation

By definition, Neuroscience is an interdisciplinary area, where biologists, physicians, physicists, engineers and psychologists work together, applying their specific skills to answer questions. One specific branch of Neuroscience, called Computational Neuroscience, deals with mathematical models of neural systems at any level, from molecules to large regions of the brain. In this context, this thesis is aimed to apply some modelling and analyzing tools from engineering to a biological system: a sensorial neuron from the rat mesencephalon (henceforth called "Mes V neurons"). The main objective behind that is to understand how neurons coupled by electrical synapses cooperate by synchronizing their behaviours.

Traditionally, chemical synapses have been thoroughly studied, because of its ubiquity in the nervous system and their amazing properties, such as plasticity, that allow them to be basis of high-level functions in the brain [145]. On the other hand, electrical synapses have received less attention historically, given that they are more rare in mammals brains [14] and perceived as more "primitive" (in part because they appeared earlier in evolution) [123]. Their strength has been observed as almost constant [57, 137], impeding them to be a source of complexity in neural circuits. On the contrary, they have been always studied as "synchronizing" connections [6, 40, 54, 56, 59, 118, 136], given that they tend to keep zero difference within the membrane potentials of coupled neurons [149], even though they may also desynchronize transiently neural circuits [31, 180], mainly because of their "low-pass filter" properties [59, 79].

Recently, pioneering research has challenged the traditional statement that "electrical synapses function as low-pass filters", finding that the subthreshold communication between coupled neurons may display frequency preference in mesencephalic trigeminal neurons [33], acting as band-pass filters. In addition to that, it was seen that the efficiency of such frequency preference not only depends on the coupling strength, but also on the membrane properties: in particular, some ionic

channels. These findings generate new questions: why and how the membrane properties determine the frequency response? Do these properties influence the synchronization between neurons? How?

This thesis is an attempt to contribute with some answers, even though new questions are generated too. The objective is to create a biologically realistic mathematical neuron model, with differential equations representing the behaviour of the real neuron. This mathematical model will complement the experimental one, in order to develop an intelligible theory [110] about how coupled neurons communicate. Therefore, it is aimed to produce a mathematical model able to interact, to talk, with the experimental one.

There are several single-neuron models' categories in Computational Neuroscience [70, 165]:

1. **Detailed Compartmental Models:** Morphologically realistic neurons that reconstruct anatomical data, fundamental to understand complex neurons (such as Purkinje [145]), where spatial information is relevent.

2. **Reduced Compartmental Models:** Trade-off between morphology and mathematical complexity, used also when spatial information is not completely known but can be roughly approximated.

3. **Single-Compartment Models:** The last frontier between single neuron dynamical detail and abstract high-level models, used extensively by hybrid (experimental and theoretical) researchers.

4. **Cascade Models:** Used for medium and large neural networks, each individual neuron is modelled as a function implementing an specific function, such as linear filters, nonlinear transformations, etc.

5. **Black-box Models:** The highest level of abstraction models a neuron by its probability distribution $p(R|S)$: the probability of response R given a stimulus S

Only the first three categories are able to interact fluently with an experimental model, whereas the remaining two are more suitable for large neurons computations. On the other hand, only approximate information about Mes V neuron morphology is available, making impossible to use a detailed compartmental model. Thus, the model developed in this thesis is a reduced compartmental model, though a single-compartment version will be used to make same mathematical calculations. The NEURON simulator [21] in Python will be used to build the model, while Python libraries Numpy, Scipy and Matplotlib will be utilized to analyze and plot the data.

1.2   Thesis contributions

Given that the objective of this thesis is to response some questions, the first contributions are their answers and/or steps made to reach them:

- The first complete model of Mes V sodium currents was developed, using Markov chains.

- Another ionic current, called I_h was modelled too, from experimental recordings.

- Single-neuron activity modulation by cyclic GMP is analyzed, with results fully compatible with experimental results.

- It is developed the first complete model of Mes V neuron, able to explain both subthreshold and spiking.

- Frequency preference of subthreshold communication between neurons is explained, both analytically and numerically, in agreement with experimental recordings.

- The dependence of the level of synchronization between spiking neurons is studied, finding that it may improve by changing/modulating the membrane properties of coupled neurons.

- The sensorial information processing is simulated for the first time, finding two behaviours: coincidence detection and contrast increase

Some preliminary results of this work have been presented at international conferences:

1. Sebastián Curti, Federico Davoine and Francisco R. Morales. cGMP modulates membrane excitability in mesencephalic trigeminal neurons of the rat. *Neuroscience 2013*, San Diego, USA. November 2013.

2. Federico Davoine, Sebastián Curti and Pablo Monzón. Modeling of sodium currents from mesencephalic trigeminal neurons by system identification and sensitivity analysis. *22th Annual Computational Neuroscience Meeting: CNS2013*, Paris, France. July 2013.

3. Sebastián Curti, Federico Davoine, James Nagy, Gregory Hoge and Alberto Pereda. Properties of electrical synapses between Mesencephalic Trigeminal (MesV) neurons. *Neuroscience 2011*, Washington, USA. November 2011.

1.3   Document structure

This thesis is organized in an incremental level of complexity. First, some cellular neuroscience and modelling tools are presented, to then use them to build model parts. The full model is assembled later and employed to simulate some Mes V

neuron's behaviours.

The chapter 2 constitutes a brief introduction to single-neuron models, aimed to people with background on differential equations but without deep biological knowledge. Model building starts in the chapter 3, where experimental recordings of two ionic currents (sodium and hyperpolarization-activated) are used to develop mathematical models of them. The quality of experimental data is analyzed carefully and several models alternatives are presented. The complete neuron model is finished in chapter 4, adding ionic channels from bibliography and approximate morphological data, obtained from transmission line theory applied to experimental recordings. A reduced single-compartment model is studied both analytically and numerically in chapter 5, in order to explain the resonance of the subthreshold communication between coupled neurons. The synchronization of neurons is discussed in chapter 6, using mathematical tools and simulations, establishing connections to the previous chapter. Finally, some conclusions are presented in the chapter 7, as well as some future work proposals.

Three final appendix present: model parameters A, the basic structure of the evolutionary algorithm used B and the state-space modelling of the sodium current C.

Chapter 2

Modelling biological neurons

2.1 Introduction

This introductory chapter presents roughly some basic biological concepts that will be used extensively along this thesis, and may be skipped by people with a general background on neuroscience. First, a basic electrical model of the cellular membrane is introduced. Then, some single neuron models are presented, with their advantages and disadvantages. In particular, the behaviour of the neuron during an action potential is studied using conductance-based models, that will be employed as the components of the neuron model developed in this work. Finally, mathematical models of electrical and chemical synapses are introduced, in order to understand how neurons get connected between them.

2.2 Excitability

Neurons are cells specialized in information processing and transmission, by electrical or chemical means. They can generate electric signals, based on the movement of dissociated ions through the cell membrane, such as sodium (Na^+), potassium (K^+), calcium (Ca^{2+}) and chloride (Cl^-). These movements create electric currents that may change the *membrane potential*, defined as: $V_m \equiv V_{in} - V_{out}$, where V_{in} and V_{out} are the voltages inside and outside the cell. Although all the cells have membrane potentials, only neurons present an outstanding feature: they can fire action potentials, also called spikes. The following sections are aimed to roughly explain the biological mechanisms that generate that behaviour.

2.2.1 Equilibrium

Although the net electric charge in biological molecules is zero, there are local charge differences that produce small voltages. In particular, the cellular membrane, that is made of a lipid bilayer, acts as a leaky capacitor, because it does not allow the free movement of ions. If $[C]_{in}$ and $[C]_{out}$ denote the concentration

Chapter 2. Modelling biological neurons

of some ion (in molecules/cm^3) inside and outside the cell, respectively, the equilibrium potential difference between both sides of the membrane can be calculated using the Nernst equation [92]:

$$E_C = V_{in} - V_{out} = \frac{RT}{zF} ln \frac{[C]_{in}}{[C]_{out}} \quad (2.1)$$

where R is the universal gas constant (8.315 mJ/(K· mol)), F is the Faraday constant (96.480 C/mol), z the valence of the ion (without dimensions: +1 for Na$^+$, K$^+$, +2 for Ca^{2+} and -1 for Cl$^-$) and T the absolute temperature (in K). The Nernst equation is only valid at equilibrium, given that it is derivated from the assumption that the net charge difference is constant between both sides of the membrane[1]

Even though Equation (2.1) is valid for only one ion, it is extraordinarily useful for understanding the basic electric behaviour of neurons and it will be extensively used throughout this thesis. Let's take the Na$^+$ ion as an example. According to Table 2.1, there is usually more sodium outside the cell than inside. Given that its valence is z=+1, its equilibrium potential for the squid axon is E_{Na}=+55 mV. The opposite can be said about the potassium ion, whose equilibrium potential is E_K=-75 mV. From the electrical point of view, these equilibrium potentials act as DC voltage sources, that promote the inward movement of Na$^+$ ions and outward of K$^+$.

On the other hand, there is a net equilibrium potential of the cell, that is called *resting membrane potential*, and results from the different concentrations of ions and the selective permeability of the membrane[2]. It is usually established at a quite negative value (from -55 to -70 mV) by a balance between Na$^+$ and K$^+$. These voltages are close to the Cl$^-$ equilibrium potential, ion that can flow quite freely at that voltage, contributing to the electric stabilization of the cell.

2.2.2   Ionic channels

Until now the cellular membrane is just a barrier for the ions. However, it is not as simple as that, because there are several complex protein structures on it, such as pumps and channels. The first ones contribute to maintain the concentration gradient between the inside and outside, like the Na$^+$-K$^+$ pump, that exchanges 3

---

[1]In general, there are two currents flowing through the membrane: the diffusion current J_{diff} due to the concentration gradient and the drift current J_{drift} due to the electric field. In equilibrium, the sum of them equals zero: $J_{diff} + J_{drift} = 0$. More details can be read in classic bibliography [92, 145].
[2]If the main ions are Na$^+$, K$^+$ and Cl$^-$, the resulting membrane potential can be calculated by means of the Goldman-Hodgkin-Katz equation: $V_{rest} = \frac{RT}{F} ln \frac{P_K[K^+]_{out}+P_{Na}[Na^+]_{out}+P_{Cl}[Cl^-]_{in}}{P_K[K^+]_{in}+P_{Na}[Na^+]_{in}+P_{Cl}[Cl^-]_{out}}$, where $[P]$ is the permeability of each ion (cm/s) [92].

	Inside (mM)	Outside (mM)	Equilibrium potential (mV)
Squid axon			
K^+	400	20	-75
Na^+	50	440	+55
Cl^-	40 to 150	560	-66 to -33
Ca^{2+}	0.4	10	+145
Typical mammalian cell			
K^+	140	5	-89.7
Na^+	5 to 15	145	+90.7 to +61.1
Cl^-	4	110	-89
Ca^{2+}	1 to 2	2.5 to 5	+136 to +145

Table 2.1: Ion concentrations and resulting equilibrium potentials for the squid axon and a mammalian cell. In general terms, both cell types share the same features (more potassium inside; more sodium, chloride and calcium outside), but there is a big variability in values. Taken from [92].

sodium ions from inside with 2 potassium from outside. Channels are pores that allow ions to flow through the membrane, driven by the voltage difference between the membrane potential and the specific equilibrium potential of each ion. Even though ionic pumps may regulate the excitability of certain neurons [48], their low transport rate (around 100 ions per second for the Na^+-K^+ pump [94]) does not allow them to have fast effects on the membrane potential. Conversely, more than one million molecules can flow through ionic channels [32], making them the basic tools to generate electric signals in neurons.

There are several types of ionic channels. Some of them are *voltage-gated*, because their opening and closing are determined by gates that get *activated* (opened) or *inactivated* (closed) depending on the membrane potential. Other type of channels are sensible to chemical agents, such as neurotransmitters and second-messengers. In all the cases, the channels open and close in a stochastic manner. However, it is possible to calculate the total current I through a large population of identical channels i as:

$$I_i = g_i \left(V - E_i \right) \tag{2.2}$$

where g_i is the conductance (in Siemens or Ω^{-1}), V is the membrane potential and E_i is the reversal potential, i.e.: the voltage when the current changes of sign. Given that most channels are selective to specific ions [71], the reversal potential is usually the equilibrium potential of that ion (E_K, E_{Na}, etc). The voltage difference between the membrane and the reversal potentials is commonly called *driving force*.

Both I_i and g_i are widely used as intensive properties, dividing them by the

area of the membrane in cm^2 (current is also reported in papers in A/F, where F is the unit of capacitance). The conductance g_i may be constant, voltage-dependent or vary with both voltage and time. The nonlinearity of most ionic channels is the basis of the complexity of neurons' dynamics.

2.2.3 Equivalent circuit

To sum up, the cellular membrane is a lipid bilayer that acts as a capacitor, whereas the ionic channels are selective pores that can be represented as nonlinear conductances allowing to pass current driven by the difference between the instantaneous membrane potential and a constant DC voltage called reversal potential. All this information can be represented in an equivalent circuit, shown in Figure 2.1. According to it, the total current I flowing through the membrane is $I = I_C + I_{Na} + I_K + I_{Ca} + I_{Cl}$, where $I_C = C\dfrac{dV}{dt}$ is the capacitive current, whose dynamics is usually several times faster than the ionic currents' ones. By convention, the total current I will be positive if it is in the outward direction. Therefore, membrane potential is governed by:

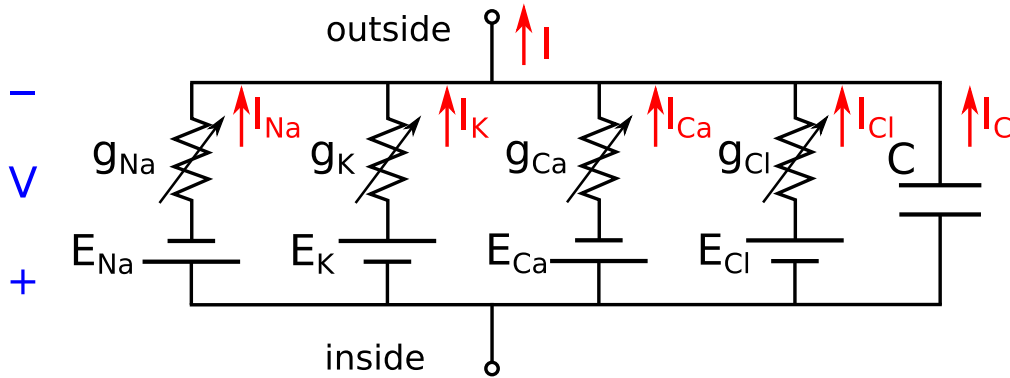$$C\frac{dV}{dt} = I_C + I_{Na} + I_K + I_{Ca} + I_{Cl} \tag{2.3}$$

Figure 2.1: Equivalent circuit of the cell membrane. Each parallel branch represents an ionic current, whose DC sources are the reversal potentials. The capacitor C is the membrane capacitance.

The differential equation (2.3) explains the membrane potential deflections of the neuron, given a total current I. There is a convention for the voltage changes, based on the action potential shape:

- Depolarization: if $V > V_{rest}$ and $\frac{dV}{dt} > 0$

- Repolarization: if $V > V_{rest}$ and $\frac{dV}{dt} < 0$

- Hyperpolarization: if $V < V_{rest}$

Equation (2.3) is valid for a *single-compartment*: a cellular membrane area that could be considered as isopotential without spatial coordinates. In some cases, a neuron is modelled as a set of connected compartments, whose voltages are governed by a partial differential equation in both time and spatial coordinates. This topic will be explained more deeply in Section 4.4.1, in the context of the model developed in this thesis.

2.2.4 Membrane excitability types

Although there is a large diversity of neuronal types, their behaviours can be classified in two main types[3], according to their frequency response to current step stimuli [73, 165]:

- **Class 1 neurons** can fire at arbitrarily low frequency, depending on the injected current amplitude.

- **Class 2 neurons** can fire only within certain frequency range whose minimum is a fixed nonzero value.

The difference between these two classes lies in how tonic spiking starts. For certain small injected current, both neuron types do not fire, given that the resting potential is a stable equilibrium point. The resting potential loses its stability for some value of the injected current and the neuron enters to a limit cycle of repetitive firing. However, while class 1 neurons pass from the stable equilibrium point to a limit cycle through a saddle-node bifurcation, class 2 start spiking through a Hopf bifurcation [88, 163]. One of the main differences between these two processes is that class 1 neurons pass suddenly from equilibrium to constant amplitude spikes, whereas class 2 present small amplitude oscillations (with almost constant

---

[3]There is also a third less common excitability type, called class 3, that is not able to present tonic spiking. In this case, the resting state is always a stable equilibrium point, regardless the injected current strength [88].
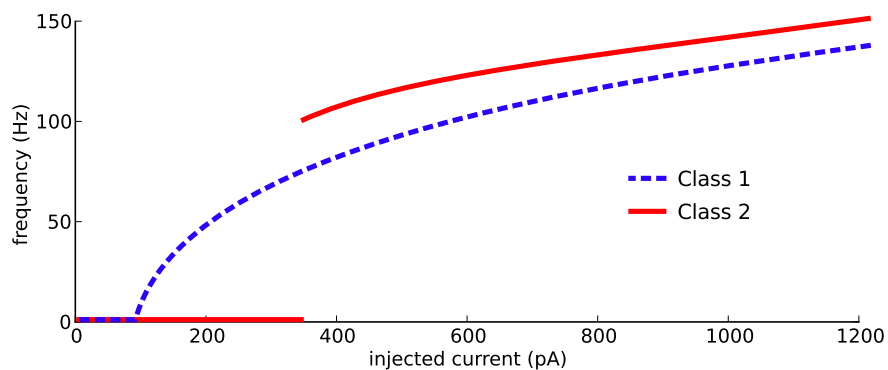

Figure 2.2: Schematic representation of frequency-current curves for different excitability types. Class 1 neurons present continuous curves, unlike class 2, that jump from equilibrium to high-frequency spiking.

frequency) before they start to fire.

A neuron may pass from being class 1 to class 2, and viceversa, depending on their membrane properties. Some of them will be studied later in this thesis, in chapters 5 and 6, within the context of mesencephalic trigeminal neurons.

2.3 Single neuron models

2.3.1 Conductance-based models

In a pioneering series of papers published in 1952, Hodgkin and Huxley developed an amazingly accurate model of the squid giant axon [74], based on experimental data [75–78], from *voltage-clamp* and *current-clamp* protocols: i.e.: setting either membrane potential or net current through it. Their model, that is still the basis of mathematical neuroscience, is also known as conductance-based model, because it is based on ionic currents that they were able to isolate and describe. They discovered that the main ions involved in action potential initiation and propagation in the squid axon are sodium and potassium, and that the resulting currents can be described by equations like (2.2), where g_{Na} and g_K are both voltage and time dependent, via *gating variables*. Each gating variable represents the fraction of gates that are in a given state. The simplest case is the potassium ion, for which they defined an activation variable n that represents the fraction of gating particles that are in the open state:

$$g_K = \overline{g}_K n^4 \tag{2.4}$$

where $\overline{g}_K$ is the maximum potassium conductance. Due to the exponent 4 (that was intended to fit the experimental data), Hodgkin and Huxley guessed that there are four gating particles that have to be open to completely open the channel[4]. According to them, the activation variable, n, satisfies the following first order differential equation:

$$\frac{dn}{dt} = \alpha_n \left(1 - n\right) - \beta_n n \tag{2.5}$$

where, α_n and β_n are the forward and backward rate coefficients between the closed and the open state, and depend on the membrane potential V. By defining the *asymptotic activation curve* n_∞ and the time constant τ_n as

$$n_\infty = \frac{\alpha_n}{\alpha_n + \beta_n}, \ \tau_n = \frac{1}{\alpha_n + \beta_n} \tag{2.6}$$

---

[4]More details in Section 3.3

Equation (2.5) can be expressed as:

$$\frac{dn}{dt} = \frac{n_\infty - n}{\tau_n} \tag{2.7}$$

The activation (and inactivation) variables for other currents are usually modelled using equations like (2.7), because of their intuitive biophysical interpretation: for a fixed voltage V, the activation variable tends to reach its asymptotic value $n_\infty = n_\infty(V)$, with a time constant $\tau_n = \tau_n(V)$. The main strength behind this kind of model for ionic currents is that it can be tested experimentally by applying voltage steps to the cell, a standard procedure for an electrophysiology lab. Moreover, $n_\infty = n_\infty(V)$ is usually a sigmoid-like (also called Boltzmann) function:

$$n_\infty(V) = \frac{1}{1 + e^{\frac{-\left(V - V_{1/2}\right)}{k_n}}}, \tag{2.8}$$

where $V_{1/2}$ is the half-value of the curve and k_n its slope at this value. Currents with half-values around the resting potential are called "low-threshold", whereas those far above it (> -20 mV, approx.) are said to be "high-threshold". The slope sign may be positive or negative, making the state variable n to be more open (more activated) or closed (more inactivated) as it gets away from the resting potential.

On the other hand, the time constant $\tau_n = \tau_n(V)$ can depend on voltage according to diverse shapes (constant, exponential, etc). Its value at different voltages gives the speed of the state-variable dynamics.

When the neuron get depolarized, the variable n increases till certain value, according to (2.7), opening the potassium channels permanently. However, sodium channels are *transient*: they become inactivated after some time. Therefore, Hodgkin and Huxley modeled them using two variables:

$$g_{Na} = \overline{g}_{Na} m^3 h \tag{2.9}$$

where both variables are governed by nonlinear first-order differential equation, such as Equation (2.7). m stands for activation and h for inactivation, because m_∞ increases with depolarization ($k_m > 0$), whereas h_∞ decreases ($k_h < 0$). The time constant of the activation τ_m is faster than the inactivation one τ_h. This model will be discussed later, in Section 3.3.
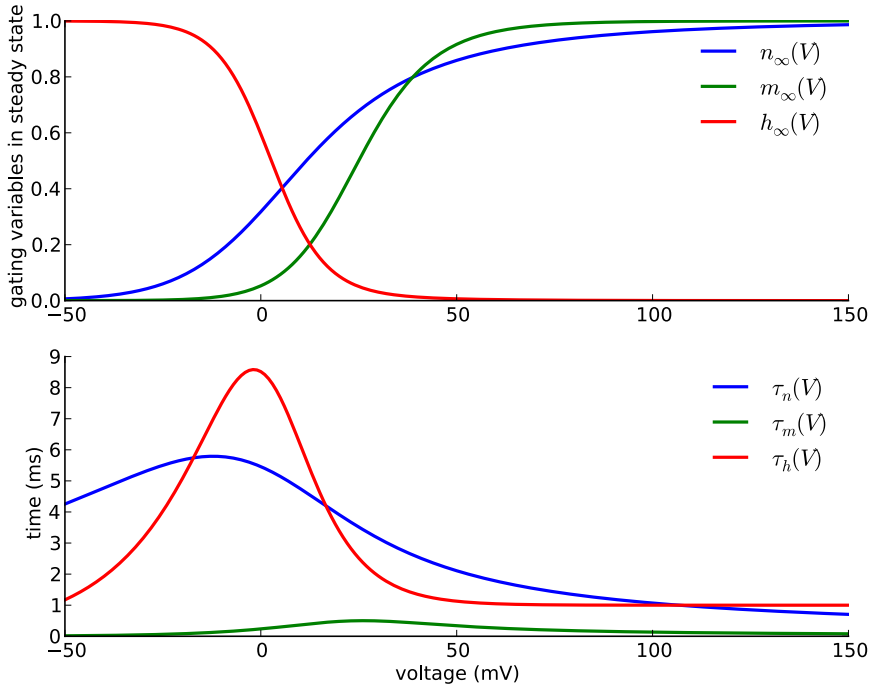
Figure 2.3: Top: asymptotic curves for the gating variables of potassium activation n_∞, sodium activation m_∞ and inactivation h_∞ variables. Bottom: the corresponding time constants. Note that sodium activation time constant is several times faster than the potassium one.

Finally, Hodgkin and Huxley added a linear term called *leak* to model the remaining current, that is carried mainly by Cl^{-1} [92]:

$$I_L = g_L \left(V - E_L \right) \tag{2.10}$$

In conclusion, the Hodgkin and Huxley model for the squid axon accounts for three ionic currents: potassium, sodium and leak. Action potentials can be explained by the interaction between these currents, as Figure 2.4 explains. Let suppose that some external positive current I_{app} is applied to a section of the cellular membrane, at t = 20 ms. After that, the following sequence of events happens:

1. As the membrane potential gets depolarized ($\frac{dV}{dt} > 0$), sodium and potassium activation variables m and n start to grow, whereas sodium inactivation h starts to decrease. However, the time constant τ_m is faster than the other two (Figure 2.3), producing a net increase of inward sodium current, that produces further depolarization of the membrane, in a positive feedback loop.

2. If the membrane potential reaches a certain *threshold*, voltage scales up extremely fast, generating a very large depolarization (around 100 mV) in a short time interval (less than 1 ms) [74].

3. With such a big depolarization, two different mechanisms start to operate causing repolarization: sodium inactivation variable h decreases to zero and potassium activation n starts to grow, producing a net outward current that makes $\frac{dV}{dt} < 0$.

4. Sodium current goes to zero quickly, leaving only the potassium current alive, that produces an hyperpolarization for some milliseconds.

5. Finally, potassium channels get desactivated (n goes to zero), making the neuron to come back to the beginning.

And, depending on the properties of the ionic channels and the applied current, the neuron can fire again or remain silent.

On the other hand, if the applied current is below threshold there is no action potential, but a *spikelet* (see at t = 5 ms in Figure 2.4), whose depolarization is smaller than the spike and with slower dynamics. In this case, the neuron is said to be in *subthreshold regime*, given that there is an atractive equilibrium point (resting potential) that remains stable.

Hodgkin and Huxley formalism ("HH formalism" from now on) has been extensively adopted by neurophysiologists to model several neuronal types: sensory neurons [11,22], pyramidal cells [7,60], deep cerebellar nucleus cells [166], Purkinje cells [91,127] and a large etc. Although more detailed models of channel dynamics have been developed based on Markov chains [23, 24, 148], the basic structure of detailed neuron models still remains the same.
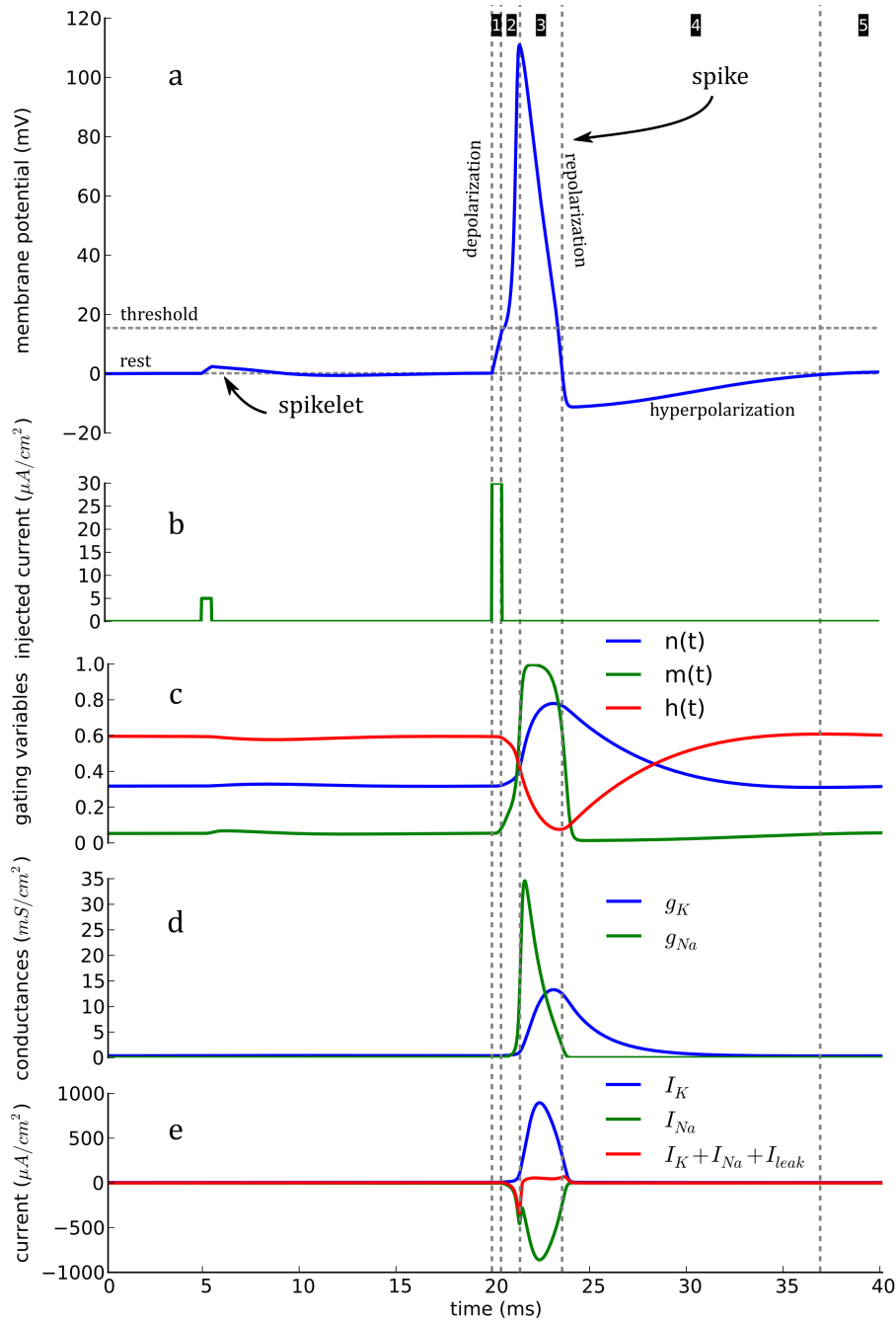
Figure 2.4: Action potential generation according to the Hodgkin and Huxley model. At t = 20 ms, a brief current pulse is injected into the cell, causing a depolarization (Figure a; note that V = 0 denotes resting potential) that produce a step increase in sodium activation variable m (b). As a consequence, the sodium conductance g_{Na} jumps to a maximum (c), producing an net inward (negative, by convention) ionic current, carried by sodium ions (d). Sodium channels start to inactivate some time later, due of the decrease of h. Simultaneously, potassium channels get activated, generating outward current that first cancels and then surpases the inward sodium current. As a result, the net ionic current becomes positive, causing an after-hyperpolarization that lasts some milliseconds.

On the other hand, at t = 5 ms a small current pulse is injected into the cell, not generating a spike, but a subthreshold response.

2.3.2 Simplified models

Conductance-based models are extremely useful, given that they are based on the real membrane mechanisms. However, for some applications that involve a large number of neurons, simpler models are needed, in order to compute them. Therefore, some mathematical models have been developed to model neural activity. In this section, the most popular models will be presented, in order to complete the whole panorama of single neuron modelling. For more extensive review of these models, please consult [88, 165].

Integrate-and-fire models

The simplest model has been proposed by Lapicque in 1907 [1], just assuming that the cellular membrane is a leaky insulator, modeled as a resistor and a capacitor in parallel. At the time, ionic channels were not yet described, so it was a good approximation of a neuron if spike generation mechanisms are not relevant. Later, Knight added to the model a reset mechanism [104] to model spiking in neuron populations:

$$C\frac{dV}{dt} = -g_L\left(V - E_L\right) + I_{ext}(t), \quad \text{if } v \leq V_{\text{threshold}}, \text{ then } V \leftarrow V_{\text{reset}} \quad (2.11)$$

where C, g_L and E_L denote the membrane capacitance, leak conductance and reversal potential, respectively. This model is known as *leaky integrate-and-fire* (LIF), because the neuron integrates the injected current I_{ext} till some threshold $V_{\text{threshold}}$, and then "fires" a instantaneous spike (delta function). Then, the membrane potential is reset to a subthreshold voltage V_{reset}, where the integration starts again. $I_{ext}(t)$ models any external current: synaptic inputs, electrodes, etc.

The great advantage of this model is that it is cheaper computationally and has less parameters than conductance-based models. It is also possible to solve it analytically under certain conditions, allowing to make theoretical calculations of networks dynamics. In particular, it is straightforward to obtain the firing frequency in terms of the injected current and tune the parameters to get the firing rate of some neuronal type [34, 98]. The model can be also extended easily, just adding ionic currents [15] or using a time-varying threshold $V_{\text{threshold}}$ [25].

In general, integrate-and-fire neuron models can be described as:

$$C\frac{dV}{dt} = -g_L\left(V - E_L\right) + I_{ext}(t) + \Psi(V) \quad (2.12)$$

where $\Psi(V)$ is a function of membrane potential that defines different models:

- Leaky integrate-and-fire: $\Psi(V) = 0$

- Quadratic integrate-and-fire (QIF): $\Psi(V) = A\,(V - V^*)^2 + g_L\,(V - E_L) - I_T$, where I_T is the rheobase current [67][5]

- Exponential integrate-and-fire (EIF): $\Psi(V) = g_L \Delta_T exp\left(\frac{V - V^*}{\Delta_T}\right)$, where Δ_T is a parameter called "slope factor", that measures the sharpness of spike initiation [50]

Unlike LIF, QIF and EIF are authentic *spiking models*, because membrane potential can diverge, "generating" a spike. For this reason, all these models need to be reset after reaching a threshold. The parameters of QIF and EIF can be obtained from approximating the asymptotic subthreshold dynamics [90]:

$$C\frac{dV}{dt} = I - I_\infty(V) \tag{2.13}$$

where all the information about ionic currents is contained in the steady state current-voltage function $I_\infty(V)$, widely used in neurophysiology as I-V curve. The choice of the integrate-and-fire model depends on the researcher's needs. For example, QIF has been showed to present a more realistic frequency response than LIF [17], but it is computationally more expensive [87]. In fast spiking behaviour, QIF tends to take more time to fire a spike than EIF [50].

Izhikevich model

Integrate-and-fire neuron models are the most computationally efficient for simulations but quite poor to reproduce a large range of biological behaviours. Thus, Izhikevich developed a model for the cortical neurons that is an excellent trade-off between computational cost and flexibility in terms of possible neurocomputational properties. It consists in a modified QIF model, with a membrane recovery variable u that represents the inactivation of sodium channels and the activation of the potassium ones [86]:

$$\begin{cases} \dfrac{dv}{dt} = & 0.04v^2 + 5v + 140 - u + I_{inj} \\ \dfrac{du}{dt} = & a(bv - u) \end{cases} \tag{2.14}$$

like the "classic" integrate-and-fire models, it requires a reset after each spike:

if $v \geq 30$ mV, then

$$\begin{cases} v \leftarrow c \\ u \leftarrow u + d \end{cases}$$

The simplicity of the model contrasts with its amazing versatility, given that it was shown to reproduce twenty different neuronal behaviours just by changing

---

[5]The QIF model is equivalent to another popular model, called *theta model* and developed by Ermentrout and Kopell [43], where a phase variable is introduced instead of voltage.

the parameters a, b, c and d [90]. For this reason, it has been adopted for making realistic simulations of large cortical networks [89, 150, 177, 192].

Other simplified models

Several other mathematical models have been developed for studying neuronal dynamics. They are in between the simplicity of integrate-and-fire models and the detailed description of conductance-based models. Thus, they are used for studying single neuron dynamics or small networks, because of their computational cost. Here, we briefly mention only the two most important.

The first one is the FitzHugh-Nagumo [46], that consists in a two dimensional differential equation inspired on the van der Pol oscillator. One variable represents the membrane potential, while the other is a recovery variable, similar to the Izhikevich model. The main difference between them is that FitzHugh model is cubic rather than quadratic. In 1962, Nagumo implemented the model analogically, using tunnel diodes [85].

In 1981, Morris and Lecar derived a simplified model that is actually a conductance based model with reduced dimensionality, given that it only accounts for one calcium and one potassium channel, and the leak [131]. It has been used for modeling several types of cells, from the original barnacle giant muscle fiber [131] to lobster stomatogastric ganglion [162] and pyramidal [141] cells. Although it was presented as a 3-dimensional model, the assumption of instantaneous dynamics of the calcium channel reduces one dimension, allowing to use phase plane analysis to analyze the model [109].

2.4 Electrical and chemical synapses modelling

Until now, the mechanisms of single neuron activity have been briefly reviewed. However, neurons never work alone: they constitute complex networks that are connected by functional contacts, called synapses. There are two types of synapses: electrical and chemical.

2.4.1 Electrical synapses

The first ones are the most primitive kind of contact between neurons: they just allow ions to flow between two neurons through specialized channels located on the cellular membranes, called *gap junctions*, made by proteins called connexins [145]. Thus, both cells have to be in physical contact to be connected by gap junctions. The ions flow through them passively, driven by the voltage difference between the two neurons. If 1 denotes the "presynaptic" neuron and 2 the "postsynaptic" one, the current passing from neuron 1 to 2, I_{12}, is:

$$I_{12} = g_{j12}\left(V_1 - V_2\right) \tag{2.15}$$

where V_1 and V_2 are the membrane potentials of the respective cells, and g_{j12} is the junctional conductance. In the case of rectifying gap junctions [53], the strength of the synapse is asymmetrical $g_{j12} \neq g_{j21}$ [49].

Equation (2.15) can be introduced as a external current in any of the single neuron models reviewed in the previous section. Note that the transmission of information has no delay and no threshold, given that the current corresponds to the instantaneous voltage difference between the neurons. Its functional role will be discussed later in this thesis (see chapters 5 and 6).

2.4.2   Chemical synapses

Chemical synapses are the most extended functional contact among neurons. Unlike electrical synapses, they are always asymmetrical and the pre and postsynaptic cellular membranes are not in contact, but separated by an empty space called synaptic cleft. They operate through a complex process of unidirectional signal transduction, based on some particles called *neurotransmitters* stored in small packages (vesicles) in the presynaptic terminal. The process of communication can be summarized in the following sequence [145]:

1. An action potential arrives to the presynaptic terminal, leading to the enter of calcium through voltage-gated channels (calcium concentration is 10.000 times higher outside the cell).

2. The increase of intracellular calcium triggers a process called exocytosis, that ends with the fusion of the synaptic vesicles with the presynaptic membrane. Neurotransmitters inside these vesicles are released to the synaptic cleft.

3. After that, neurotransmitters diffuse in the empty space between pre and postsynaptic cellular membranes, until reaching specific receptors in the postsynaptic neuron.

4. After the binding of the neurotransmitter and the receptor, two things may happen, with different time-scales:

   - if the receptor is *ionotropic*, it opens and allows current to flow to the postsynaptic neuron
   - if the receptor is *metabotropic*, it triggers a chain of chemical agents that ends with the opening of ionic channels in the postsynaptic cell

5. Depending on the type of synapse, the currents can be *excitatory* (EPSC: excitatory postsynaptic current) or *inhibitory* (IPSC), because they depolarize or hyperpolarize the postsynaptic neuron, respectively.

6. After some milliseconds, if there is no more stimuli in the presynaptic terminal, the neurotransmitter is captured by the presynaptic cell and postsynaptic receptors get closed, ending the PSC.

In conclusion, a chemical synapse is triggered by an action potential in the presynaptic cell and generates some electrical currents in the postsynaptic one[6]. This can be modelled as a postsynaptic current I_{syn} according to the following equation [165]:

$$I_{syn} = g_{syn} \left(V_2 - E_{syn} \right) \tag{2.16}$$

where all the terms, except E_{syn} are time-dependent and valid for $t > t_s$, being t_s the time of the release of neurotransmitter. As usual, V_2 indicates the postsynaptic membrane potential.

From the equation, it can be seen that E_{syn} determines if the synapse is excitatory or not. When E_{syn} is above (below) the resting potential $V_{2\text{rest}}$, the resulting current is depolarizing (hyperpolarizing).

g_{syn} represents the change in postsynaptic conductance, that last just some milliseconds after t_s and can be described according to a single exponential decay:

$$g_{syn}(t) = \overline{g}_{syn} exp \left(-\frac{t - t_s}{\tau} \right) \tag{2.17}$$

or an alpha-function:

$$g_{syn}(t) = \overline{g}_{syn} \frac{t - t_s}{\tau} exp \left(-\frac{t - t_s}{\tau} \right) \tag{2.18}$$

Given the complexity of the chemical transmission, it can be modulated in several ways. In particular, the synaptic plasticity is the basis of the memory formation and learning, throughout the change of the strength of the synapses (g_{syn}) [145].

---

[6]Actually, it can also generate chemical changes through second messengers. For a more detailed explanation, please consult classical Neuroscience bibliography [92, 145].

2.5   Summary

This chapter has reviewed basic concepts of cellular neuroscience. The neuron membrane was modelled as an electrical circuit, whose components are DC-voltage sources (due to ionic charge imbalance in equilibrium), a capacitor (the lipid bilayer) and (usually nonlinear) conductances.

Then, mathematical models of these components were examined. Conductance-based models were presented using the Hodgkin and Huxley formulation of the sodium and potassium channels for the giant-squid axon. Given that this kind of models is biologically pausible, it will be used extensively in this thesis to model mesencephalic trigeminal neurons according to experimental data and bibliography. The simplified models presented later will be useful to get some theoretical results that may be discussed. Finally, functional connections between neurons (electrical and chemical synapses) were presented, because they will be used to analyze how neurons cooperate.

Chapter 3

Characterization of sodium and hyperpolarization-activated currents

3.1 Introduction

This thesis is centered on the modeling and analysis of rat mesencephalic trigeminal neurons. Given that it is needed to model single neuron activity with some level of detail, the best choice is a conductance-based model, such as the Hodgkin and Huxley model that was reviewed in the Chapter 2.

The basic elements of a conductance-based model are its ionic channels. Some of them have been thoroughly addressed in bibliography [42, 80, 101, 133, 156, 170, 185, 188] and will be reviewed in the Chapter 4. In this chapter, two relevant currents will be modelled from experimental data, obtained by procedures described elsewhere [33]: the hyperpolarization-activated I_h and the sodium I_{Na}[1].

Indeed, sodium current modelling was not an objective at the beginning of this thesis, but became one after failing to produce reasonable simulations. Then, experimental data was generated to feed the mathematical model. On the other hand, I_h modelling comes from another research line at the lab, and was taken as an opportunity to refine the model and not a central goal of the thesis.

All the experimental data presented in this thesis were measured at the Mes V neuron soma, using the patch clamp method, in the whole-cell configuration. In this setup, the recording pipette is connected to the interior of the neuron through a small hole, without any contact with the extracellular medium [145]. In this configuration, two main options were used: current-clamp and voltage-clamp, that set either current through the membrane or its voltage.

---

[1]The sodium current is usually seen as the sum of three components: see Section 3.3

3.2 Hyperpolarization-activated current and its modulation by cyclic GMP

3.2.1 Introduction

The hyperpolarization-activated current I_h is a non-selective cation current, permeable to both potassium and sodium ions, with a reverse potential E_h between E_K and E_{Na}. As its name suggests, this current gets activated for voltages below resting membrane potential, without presenting inactivation. Given that E_h is generally above resting potential, I_h acts as an inward current, contributing to repolarize membrane potential. It has been reported in many cell types [55,81,115,122,128] and linked with two main roles: rhythm generation and control of dendritic integration and firing [111,181].

In Mes V neurons, I_h was first described by Khakh and Henderson [101], fitting its activation by a standard HH first order process, finding that $V_{1/2}$ = -94 mV and k = -8.4 mV, that was able to explain the conspicuous "inward rectification" (repolarization at hyperpolarized voltages) present in these neurons. Figure 3.1 shows an example of that: after the injection of a negative current and voltage hyperpolarization, I_h starts to grow, because of an increase of both driving force and activation, producing a late repolarization, called "voltage sag". When the injected current is turn to zero, I_h channels are still open, depolarizing the membrane above the resting potential and producing one or more "rebound" spikes.

Later, Tanaka et al [170] studied I_h again, in order to explain a low-frequency resonance at membrane potentials below -65 mV. Interestingly, comparing rats of 2-3 days with those of 10-12, they found that half-maximal activation potential $V_{1/2}$ presents a positive shift (from -113 to -105 mV) and that specific maximum conductance (conductance per unit area) doubles.

Both papers provide an experimental description of I_h current, but with few information about its activation time constant. In addition to that, the very hyperpolarized value of $V_{1/2}$ makes I_h quite unsuitable to affect Mes V neurons behaviour. However, it has been shown that I_h can be modulated by a shift on its half maximal activation voltages by cyclic nucleotides (such as cyclic GMP and cyclic AMP) [66] or neurotransmitters (like serotonin or nitric oxide) [68,69,103], that interact with Mes V neurons [107, 140]. Thus, another experimental characterization of I_h was taken out by Sebastián Curti at the School of Medicine, allowing us to create a new model of this current. I_h is computed by substracting current recordings in presence of cesium Cs^{2+} (an I_h blocker) 2 mM (millimolar) to those in control conditions and in presence of 0.5 mM cyclic GMP (cGMP).
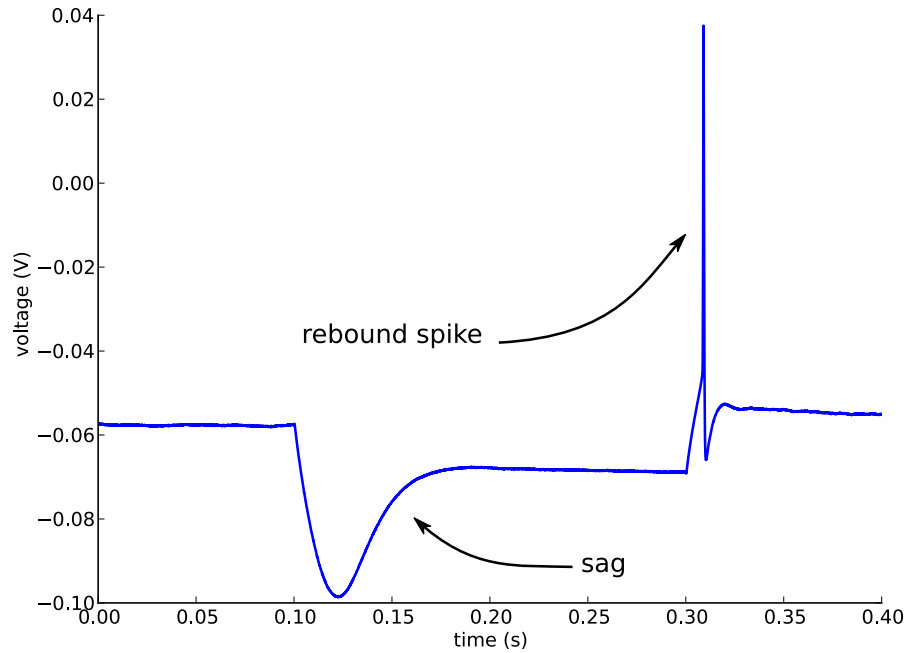
Figure 3.1: Experimental voltage response to a injected negative current. After a rapid hyper-polarization, I_h starts to operate, generating a voltage "sag" that repolarizes the membrane potential. At t = 0.3 s the injected current is shutdown, allowing the membrane potential to return to resting value. However, I_h is still open, acting as an inward current that produces a "rebound spike".

3.2.2 Modelling from experimental recordings

According to previous articles, I_h current can be modelled by a first order process:

$$I_h = \overline{g}_h . s . (V - E_h) \qquad (3.1)$$

where s is governed by a standard HH equation (2.6). The full description of the model will require finding the parameters of the reverse potential E_h, steady-state activation s_∞ and time constant τ_h.

The reverse potential E_h can be obtained by the stepping up voltage from a holding potential where I_h is almost totally activated (-100 mV). The resulting current, shown in Figure 3.2, displays an artifact at the moment of the step, because of the inability of the electronic recording equipment to control voltage when the current change abruptly, generating a rebound spike.

Without taking into account the artifact, the current response is almost step-like and its value is linear with the command voltage, as shown in the Figure 3.3. If I_h is modeled according to the HH formalism and its kinetics are slow, the value of the post-step current $I_h = g_h\,|_{V=-100mV} \cdot (V - E_h)$, where $g_h\,|_{V=-100mV}$ is the channel conductance at V = -100 mV and the slope of Figure 3.3. Hence, the reverse potential E_h can be obtained as the voltage where I_h is zero: $E_h =$
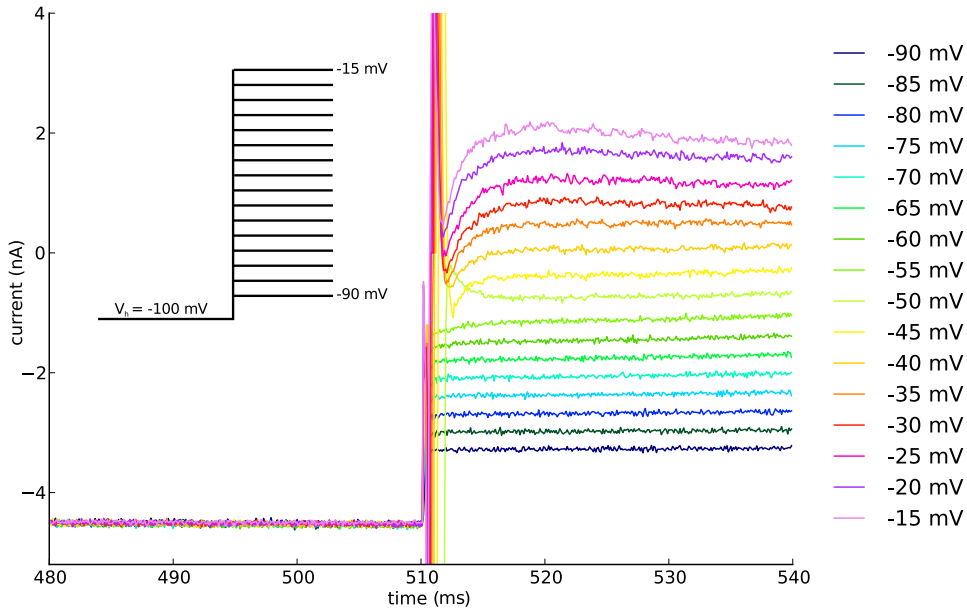
Figure 3.2: Experimental recorded currents used to obtain E_h. The protocol, shown in inset, consists in a prepulse to a very hyperpolarized voltage, where I_h is almost fully activated and then stepping up voltage. At the time of the step, there is an artifact that comes from a spike.

-40.2 mV, similar to the value obtained by Tanaka et al [170] in the same cell type.

The steady-state activation curve $s_\infty = s_\infty (V)$ can be obtained using the same idea used to obtain the reversal potential: after a long voltage step (whose value V_1 ranges from -125 to -40 mV), voltage is stepped to a fixed value[2] $V_2 = $ -70 mV. Given the slow kinetics of I_h, the conductance of the channels does not change instantaneously, keeping its previous value $s_{\infty 1} = s_{h\infty}(V = V_1)$, resulting in a current that can be expressed as:

$$I_h = \overline{g}_h.s_{\infty 1}.(V_2 - E_h), \quad V_1 = -125, -120, \ldots - 40 \text{ mV}, \quad V_2 = -70 \text{ mV} \quad (3.2)$$

The main advantage of equation (3.2) is that the only difference between current traces is the steady-state activation value $s_{\infty 1}$, because the driving force is the same. According to that, Figure 3.4 shows how the I_h current traces saturates for values below -110 mV and above -55 mV, as a result of the sigmoid-like activation.

Hence, the steady-state activation curve $s_\infty(V = V_1)$ can be simply calculated by normalizing the current:

$$s_\infty(V = V_1) = \frac{I_h}{\overline{g}_h (V_2 - E_h)} \quad (3.3)$$

Figure 3.5 displays the mean steady-state activation values and their standard errors, as well as sigmoid fittings. In presence of cGMP, I_h becomes activated at

---

[2]This value of V_2 is chosen for keeping a substantial driving force while not hyperpolarizing too much the cell, in order to avoid damaging.

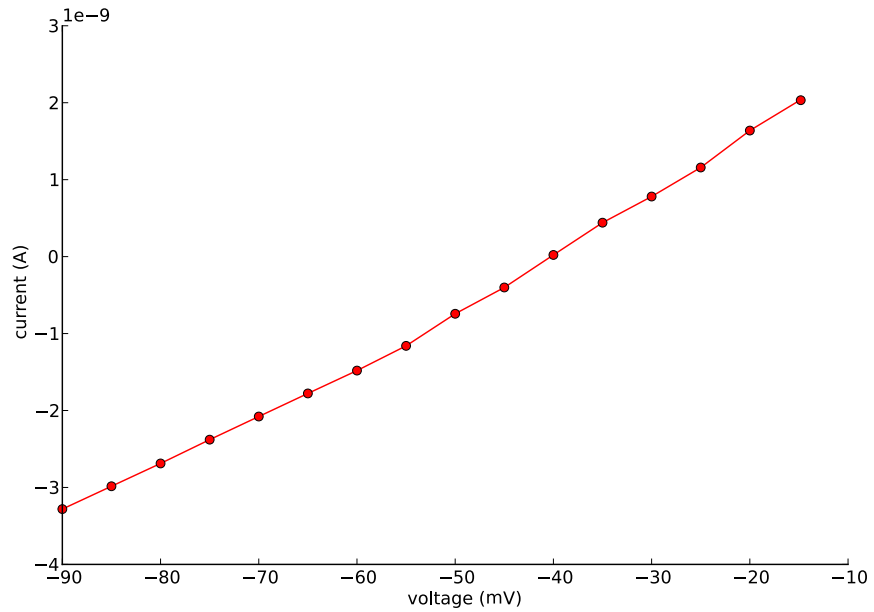## 3.2. Hyperpolarization-activated current and its modulation by cyclic GMP

Figure 3.3: Mean current response after applying a voltage step, according to the protocol shown in Figure 3.2. The relationship is linear, indicating the ohmic response of the I_h current.
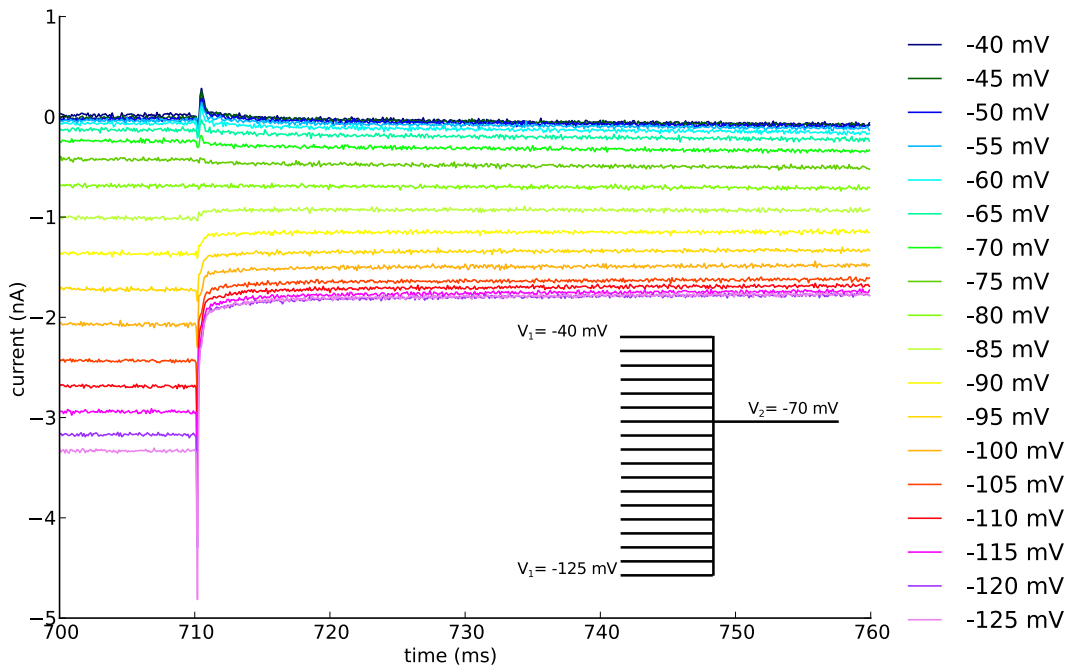

Figure 3.4: Tail currents in control conditions. The recording protocol is displayed in the inset. Note the saturation of the current at both extremes of the voltage range.
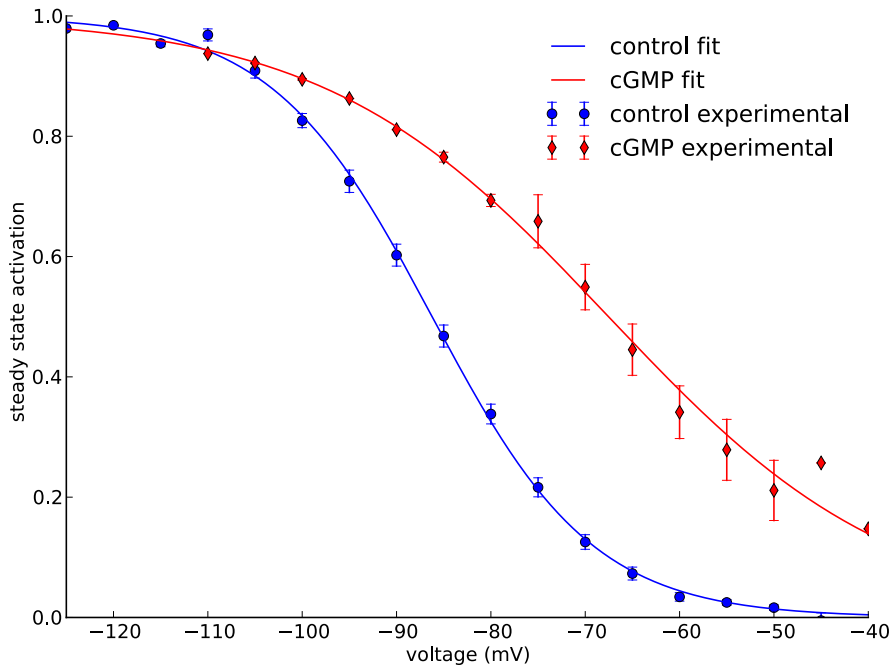
Figure 3.5: I_h steady state activation curves, in control conditions (n=8) and in presence of cGMP (n=4). Experimental data is shown as the mean value and standard error of several recordings, for each voltage. Continuous lines are sigmoid fits.

more depolarized values, going from 2.6% in control conditions to 30.5% at -55 mV, with many consequences in Mes V neuron behaviour, as it will be discussed in the following chapters.

Finally, the description of I_h is completed by finding its time constant $\tau_h = \tau_h(V)$. The experimental protocol consists in applying hyperpolarizing voltage steps from a holding potential where I_h is supposed to be largely deactivated (-50 mV), recording the resulting current. Figure 3.6 shows that recordings near resting membrane potential in control conditions are distorted by an artifact, due to the low activation of I_h. On the other hand, the recordings below -70 mV behave as expected, with a single-exponential time course and saturation at very low voltage values.

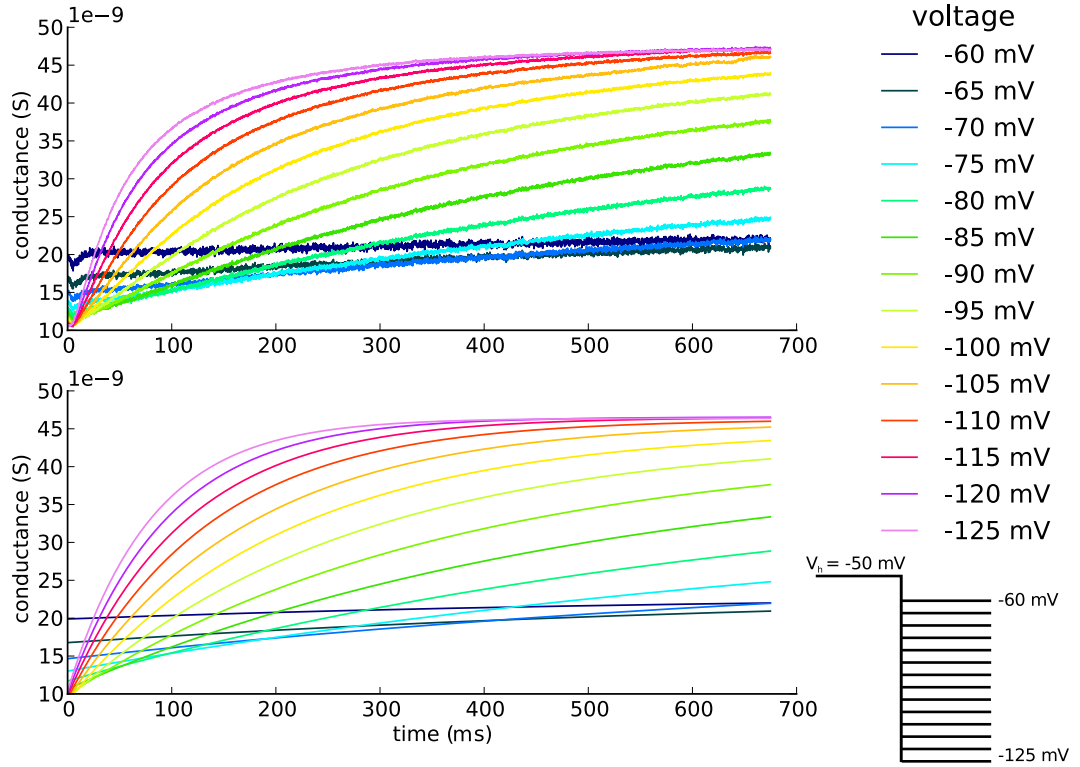## 3.2. Hyperpolarization-activated current and its modulation by cyclic GMP

Figure 3.6: Experimental recordings (top) and fittings traces (bottom) for hyperpolarized voltage steps (colour references are the same), in control conditions and cGMP for one cell, used to get the time constants. The experimental protocol is shown in the inset (bottom-right).

Figure 3.7 shows the time constants means and the corresponding standard errors obtained from fitting several cells. Unlike control time constants, cGMP ones show small standard error in the whole voltage range, because of its larger activation (see Figure 3.5). Interestingly, cGMP does not only shift the steady-state activation curve, but it also makes I_h faster. Both experimental time constants can be fit by bell-shaped curves: a lorentzian for control conditions and a gaussian for cGMP:

$$\text{Control: } \tau_h(V) = \frac{A}{1 + \frac{V-m}{\gamma}^2} + \tau_{h\min} \tag{3.4}$$

$$\text{cGMP: } \tau_h(V) = A.e^{-\left(\frac{V-m}{\gamma}\right)^2} + \tau_{h\min} \tag{3.5}$$

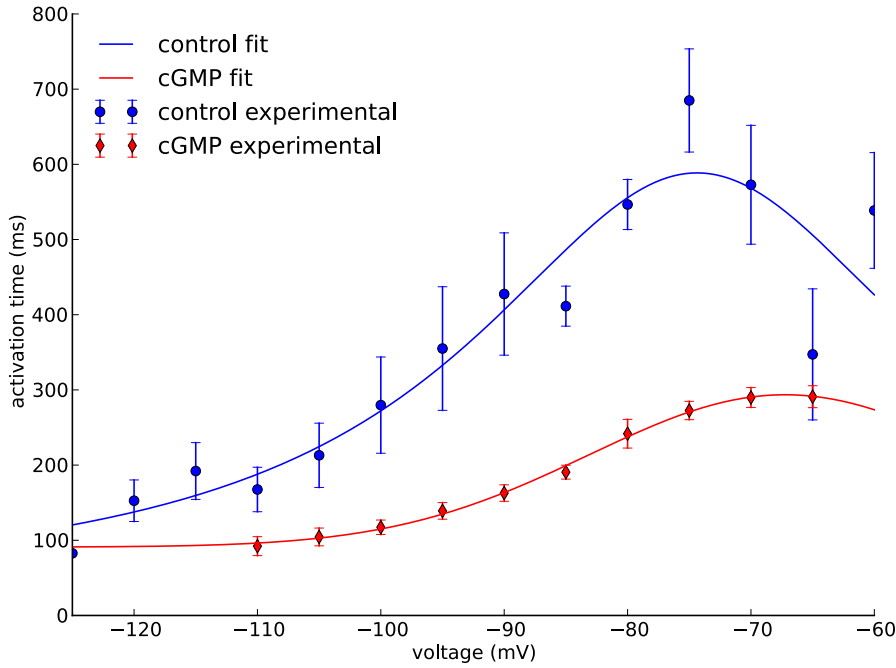The resulting parameters can be found in Table 3.1.

Figure 3.7: Hyperpolarization-activated current time constants for both control conditions (n=8) and cGMP (n=4). The lines denote fittings according to equations (3.4-3.5)

	$V_{1/2}$	k	A	m	γ	$\tau_{h\min}$
Control	-86.2 mV	8.5 mV	560.9 ms	-74.4 mV	22.5 mV	27.7 ms
cGMP	-67.5 mV	15.1 mV	202.7 ms	-67.2 mV	22.4 mV	90.9 ms

Table 3.1: Fitting parameters for I_h current. The first two columns are the half-activation voltage and slope of steady-state activation s_∞ (sigmoid function), whereas the following ones correspond to the time constants τ_h (described by equations (3.4-3.5).

3.3 Sodium currents

3.3.1 Introduction

Even though sodium currents are less diverse than potassium ones [27,71], there are three completely different sodium currents, all of them present in Mes V neurons:

- **transient** I_{NaT}: the sodium current studied by Hodgkin and Huxley [74], it is responsible of the large inward current that depolarizes the neuron during the action potential. It presents an almost instantaneous activation and fast inactivation.

- **persistent** I_{NaP}: a low-threshold current with instantaneous activation and almost no inactivation.

- **resurgent** I_{NaR}: this unusual current can be measured after repolarizing the membrane to around -40 mV, if before it was kept very depolarized (at

around +30 mV) during some time (approximately 20 ms) [4, 146].

The persistent sodium current I_{NaP} has been extensively studied in Mes V neurons, because of its role on subthreshold resonance [42] (that will be studied in the next chapter) and in spike initiation [95]. It has been modelled as an instantaneously activated current, whose half-activation voltage $V_{1/2}$ is close to the resting potential [41, 188]. The I_{NaP} current has been shown to display an extremely slow inactivation (with a time constant of around 2 seconds [186]) that can be neglected during short-time protocols.

Unluckily, the remaining sodium currents (transient and resurgent) have not been completely modelled in Mes V neurons. For the transient current, only Enomoto et al [41] measured the sigmoid-like steady-state curves according to HH formalism, finding $V_{1/2}$=-32.9 mV and k=6.1 mV for activation and $V_{1/2}$=-61.9 mV and k=-9.5 mV for inactivation. However, there are no reports of the time constants of both processes. On the other hand, they also measured the resurgent current, finding that it is maximum when repolarizing to -40 mV, but without making a mathematical model of it.

Given that the transient sodium current is the main responsible of the action potential, it is fundamental to have a complete model of it. Previous complete models of Mes V neurons [113, 133, 186] have used I_{NaT} equations found in other cell types [13], but without checking their validity. Therefore, Sebastián Curti made experimental recordings of the sodium currents, in order to provide data for a more suitable model, according to procedures described elsewhere [33], with some technical adjustments made due to the fact that the transient sodium current gets large values in few hundreds of microseconds. The most important one is that the extracellular sodium concentration was decreased to 26 mM (normal concentration is $[Na]_{ext}$ = 150 mM), in order to decrease the driving force $\Delta V = V - E_{Na}$ by obtaining a smaller reverse potential E_{Na} = 32.8 mV (instead of 78 mV).

Currents in control conditions were recorded under voltage clamp configuration and then substracted with recordings in presence of tetrodotoxin (TTX, a sodium channel blocker [71]) 0.5 μM, in order to get the sodium currents. During the voltage clamp, membrane potential was stepped up, from holding potentials of -70, -55 or -50 mV to depolarized values (this is usually called *activation protocol*). Sodium currents appear clearly in all the recordings, as an inward current with rapid activation and inactivation, both voltage-dependent. However, unlike I_h, the sodium current presents a rapid activation to large values that can destabilize the voltage clamp. Thus, it is important to be cautious when analyzing experimental recordings, given that several errors may happen.

3.3.2 Experimental errors' analysis

The sodium current recordings present an artifact at the beginning of the voltage step, due to two factors. The first one is the charge of the pipette capacitance C_p, whose current i_{Cp} is proportional to the voltage derivative[3]: $i_{Cp} = C_p \frac{dV}{dt}$. Thus, the abrupt change in voltage leads to an almost infinite derivative, making capacitive current extraordinarily large. This current would be zero if the control and TTX conditions were exactly equal, because they would be substracted, but that does not happen in reality. The second experimental drawback is that voltage clamp is only achieved after some *finite* time: for example from 200 to 600 μs in the experiment shown in Figure 3.9, where membrane potential was simultaneously recorded by another electrode. Therefore, the voltage derivative is not infinite (but it is still large), but new artifacts arise from the more complex shape in voltage curve. In some cases, there is even a small overshot after reaching the command voltage.

In addition to that, Figure 3.9A shows that there could be a small error between the command voltage and the measured one in steady-state [116], due to the "series resistance" R_S, that represents the extracellular fluid resistance between ground and the membrane [92]:

$$V_m = V_{clamp} - I_{clamp}R_S \qquad (3.6)$$

where I_{clamp} denotes the current injected to the neuron to set its membrane potential V_{clamp}, according to the schematic representation of the voltage clamp circuit (see Figure 3.9C). Usually, the series resistance is reduced as much as possible while recording, by applying a percentage of compensation $f_{\text{compensation}}$ (in these recordings, around 80%) via software. Hence, the maximum resistance series error e_S is:

$$e_S(\text{max}) = I_{clamp}(\text{max})R_s\left(1 - f_{\text{compensation}}\right) \qquad (3.7)$$

According to Figure 3.9D, $e_S(\text{max})$ overestimates the voltage clamp error, probably because it is usually reached before 1.0 ms, when the membrane potential is not stable yet. On the other hand, the steady-state current underestimates the error, given that the current becomes smaller as the step voltage increases, but the experimental error remains almost constant. As a conclusion, neither maximum nor steady-state currents can be used for getting a reliable estimation of the voltage clamp error in the cases where there is no recording of the membrane potential.

There are two more criteria to analyze voltage clamp quality when recording sodium currents [147]:

1. The currents recorded in the region -50 to -20 mV, by steps in 5 mV (or less) increments, have to be smoothly graded. This range is chosen because it is approximately the region where sodium current activates and the driving force is quite large (do not forget that reverse potential for sodium is

---

[3]The tip of the pipette was painted with a polymer called Sylgard, to decrease the value of C_p and reduce the capacitive current i_{Cp} [191].
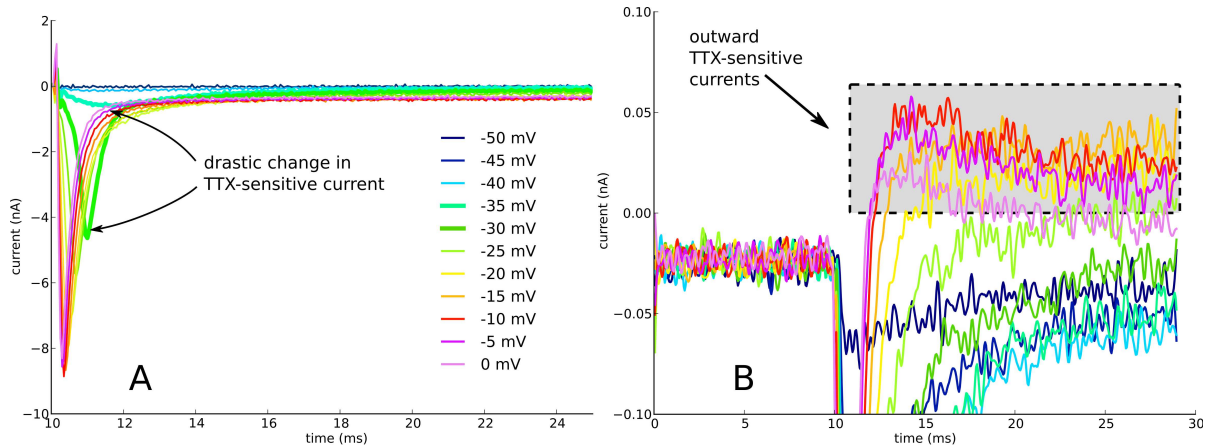
Figure 3.8: Voltage clamp errors from different recordings. Left: TTX-sensitive currents become outward for voltage commands above -20 mV, being transient above -10 mV. Right: drastic change in TTX-sensitive current between -35 and -30 mV.

positive). A large and rapid inward current could lead to a longer time to get the membrane voltage stabilized, distorting the current traces, as Figure 3.8-A displays between -35 and -30 mV voltage steps.

2. TTX-sensitive currents should not have any transient outward current, like those shown in Figure 3.8-B. As discussed before, the series resistance R_S produces a small error e_S in clamped voltage due to the current flow through it. Given that the voltage drop in the series resistance is proportional to the amount of current (assuming that R_S remains constant), there is more voltage drop in control recordings than in TTX ones, given that inward current is larger in the first case. Therefore, effective membrane voltage is larger for control recordings. The difference in depolarization between the two conditions could lead to a larger activation of an outward current, that does not appear in control recordings (because it is hidden by the inward sodium current) but it is visible when substracting control and TTX recordings.

Finally, only 1 in 7 neurons fulfills all the voltage clamp quality criteria and will be used in the next section for developing models. Its current traces are shown in the Figure 3.10, along with a simulation of the model by del Negro and Chandler [133]. Actually, this best quality recording was recorded by reducing the number of sodium channels with 10 nM TTX (concentration not enough to block all of them). In addition to that, hepes was used as a buffer.

There were several more recordings that were also discarded before being analyzed, due to several reasons: large baseline drifts, non adequate spatial control of voltage (spikes were generated in the axon hillock, that was not clamped), drastic changes in series resistance, death of cells after some time, etc. Even though it is not possible to demonstrate that these valid recordings are representatitive of the
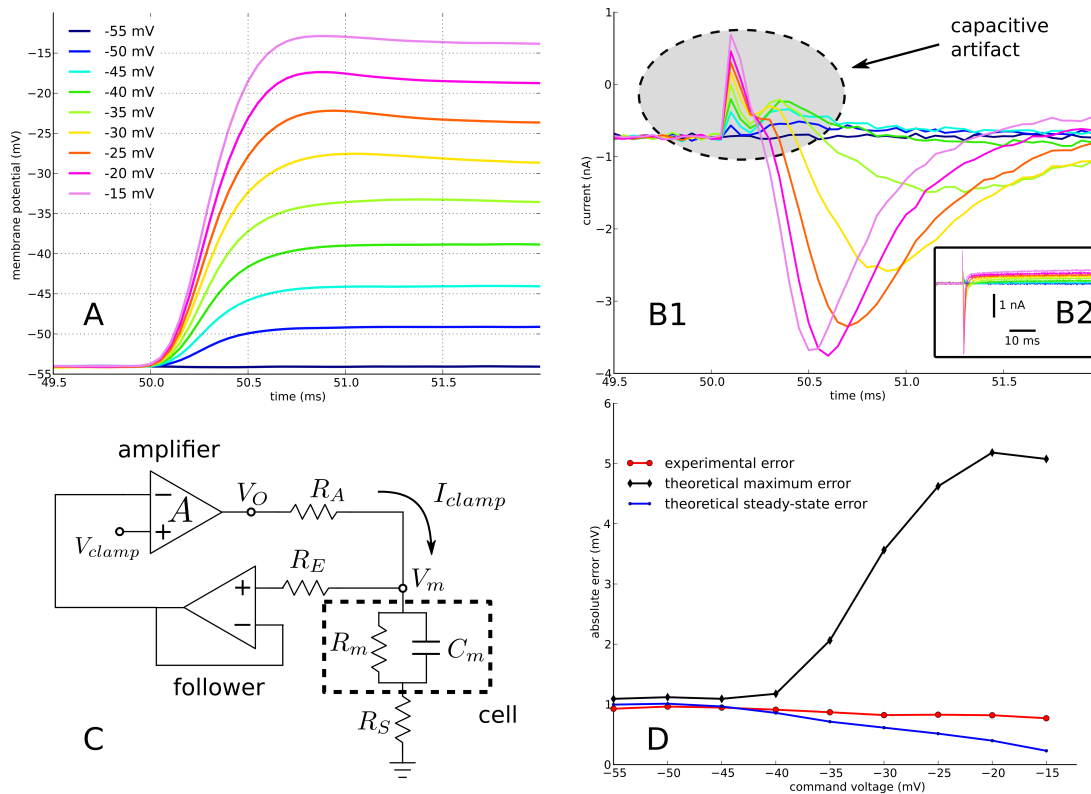
Figure 3.9: In one experiment, the membrane potential was recorded with a electrode, while applying voltage clamp experiment with another one that recorded the resulting current. Figure A shows the actual membrane potential when a voltage command (colour code in legend) was applied to step it up at 50.0 ms. The resulting current (B) displays a capacitive artifact discussed at the beginning. According to the simplified circuit of the voltage clamp protocol shown in C [92], the error between command voltage and membrane potential is proportional to the applied current. However, figure D demonstrate that the experimental error remains quite constant in voltage, taking approximately the value of the maximum theoretical one when there is almost no current.

sodium currents, they are pretty similar to those presented by Enomoto et al [41] and completely different from those expected from the model by del Negro and Chandler, as Figure 3.10 shows. Therefore, these valid current traces at least can be useful to extract some basic data not available from literature, such as the time constants.

3.3.3   Modelling from experimental recordings

The traditional way of modelling the transient sodium current has been using the HH formalism, according to expressions similar to equation (2.9) [13, 51, 100, 155]. The theoretical interpretation of this model, made by Hodgkin and Huxley is similar to that commented in the previous chapter for the potassium current (see section 2.3.1): each ionic channel has "gates" controlled by "gating particles". In
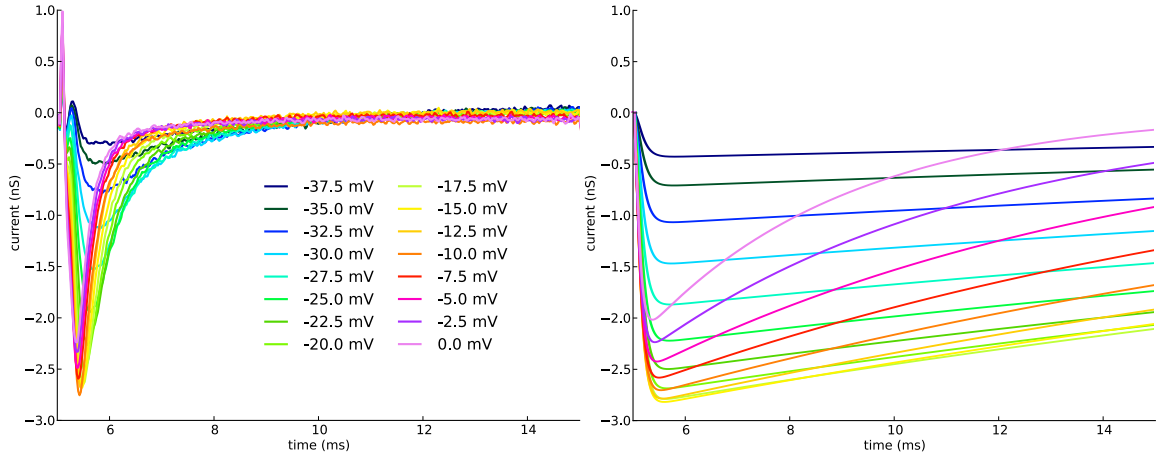
Figure 3.10: Current traces from experimental recordings (left) and previous HH model by Del Negro and Chandler [133] (right).

the case of the sodium channel, there should be four "gating particles": three m particles controlling activation and one h particle for inactivation, each one undergoing first-order transitions between two forms [92]:

$$\text{``1}-\text{m''} \underset{\beta_m}{\overset{\alpha_m}{\rightleftharpoons}} \text{``m''}: \quad \frac{dm}{dt} = \alpha_m(1-m) - \beta_m m$$

$$\text{``1}-\text{h''} \underset{\beta_h}{\overset{\alpha_h}{\rightleftharpoons}} \text{``h''}: \quad \frac{dh}{dt} = \alpha_h(1-h) - \beta_h h$$

where the kinetic rates $\alpha_{m,h}$ and $\beta_{m,h}$ depend on the membrane potential V.

Amazingly, the HH model for the sodium current can be also represented by the kinetic model shown in Figure 3.11, with three closed states $C_{1,2,3}$, four inactivated $I_{1,2,3,4}$ and only one open O [167]. All the inactivated states have zero h gates, but a different number of m ones. Similarly, the difference between the closed states and the open one is the same, but all of them have one h gate. Vertical rates from (to) inactivated states $I_{1,2,3,4}$ are equal, because they all represent the same conformational change: a gate h becomes available (unavailable). On the other hand, horizontal rates are not equal, because they represent interactions between states with different m gates. For example, the transition from the farthest closed state C_1 to C_2 happens if only one in three (kinetically undistiguishable) m gates becomes available: that is the reason of the $3\alpha_m$ rate. However, going from C_3 to O implies that the remaining unavailable m gate of C_3 becomes available, leading to the α_m rate. The same can be said for the reverse transitions: O goes to C_3 by dropping only one of its three m gates [92].

Now, let remember the definition of an voltage-gated ionic channel: a pore on the membrane that allows specific ions to cross from outside to inside the cell, depending on the membrane potential. Actually, the "pore" consists of an integral membrane protein, made of several protein subunits whose movements can

33

be controlled by voltage [120]. Recordings from individual channels have shown that they open and close stochastically, depending on the membrane potential [71]. Therefore, the kinetic representation of Figure 3.11 can be interpreted as a memoryless Markov model [65] of a single sodium channel, where each state represents the probability of a given conformational form [154]. For example, O indicates the probability of the channel to be in the open state. Consequently, the rates represent the transition probability from one state to another. The occupancy of each state can be found by solving the corresponding master equation, like this one for the O state:

$$\frac{dO}{dt} = \alpha_m C_3 + \alpha_h I_4 - (3\beta_m + \beta_h)O \tag{3.8}$$

Another outcome of the stochastic model is that the sum of the states occupancies must be one. For the model in Figure 3.11, that means: $C_1 + C_2 + C_3 + I_1 + I_2 + I_3 + I_4 + O = 1$. Therefore, a Markov model with N states may have only $N-1$ indenpendent master equations.

The deterministic HH model can be interpreted as the Markov model in the limit of a large number of channels (whole cell recordings), where each state becomes the *fraction* of channels occupying it [36]. In this case, a macroscopic current can be expressed as:

$$I = \gamma \cdot N \cdot O \left(V - E_{Na} \right) \tag{3.9}$$

where γ is the single channel conductance and N the number of channels.

Conceptually, Markov models are closer than HH models to the real operation of ionic channels, given that it would be possible to map each state to a conformational form of the proteins, determined by molecular dynamics [161]. For this reason, Markov models have to satisfy some physical constraints:

- Exponential transition rates: According to thermodynamics, the transition rate between two states depends exponentially on the free energy barrier
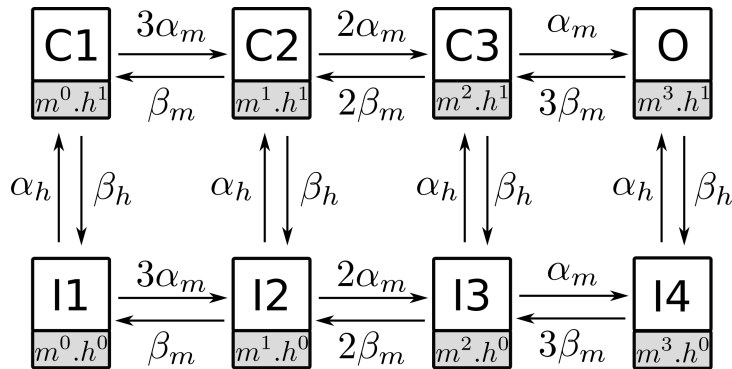

Figure 3.11: Kinetic representation of the HH model for the sodium channel. $C_{1,2,3}$, $I_{1,2,3,4}$ and O represent closed, inactivated and open (conductive) states, respectively.

between them $\Delta G(V)$: $k = k_0 e^{-\frac{\Delta G(V)}{RT}}$, where R is the universal gas constant and T the absolute temperature. For a given voltage V the free energy barrier can be approximated as $\Delta G(V) \simeq a + bV$, with a and b constants (b can be zero). [37]

- Microscopic reversibility (detailed balance [65]): At thermodynamical equilibrium, without an external source of energy (such as ATP), the transition rates between two states have to be equal. For systems with loops, the product of the rates in the clockwise direction around a loop is equal to the product on the other direction. [153]

On the other hand, Markov models are computationally more expensive than simpler deterministic HH equations [135, 183]. In addition to that, its kinetic constants cannot be easily obtained from experimental data [20, 28] and it is difficult to identify them with the biophysical changes at the molecular level [45]. Therefore, there is a trade-off between the complexity and intelligibility of Markov models, that may makes them unsuitable to be used in cases where there is no need of such high levels of detail.

One of the first Markov models of sodium current was developed to better understand its recovery from inactivation in hippocampal neurons [105]. This model was later expanded [102, 148], in order to explain the sodium resurgent current, that appears when membrane potential is repolarized after depolarization. The idea is simple: in addition to the "standard" closed, inactivated and open states, there should be an open "blocked" state OB whose only exit is through the open state (see Figure 3.12). At resting potential, the most occupied states are the closed and inactivated ones. The open state's occupancy increases rapidly after a sudden depolarization, decaying to its neighbouring states: C_5, I_6 and OB. Unlike C_5 and I_6, OB can only be depleted by passing through O, generating a transient current identified as "resurgent".
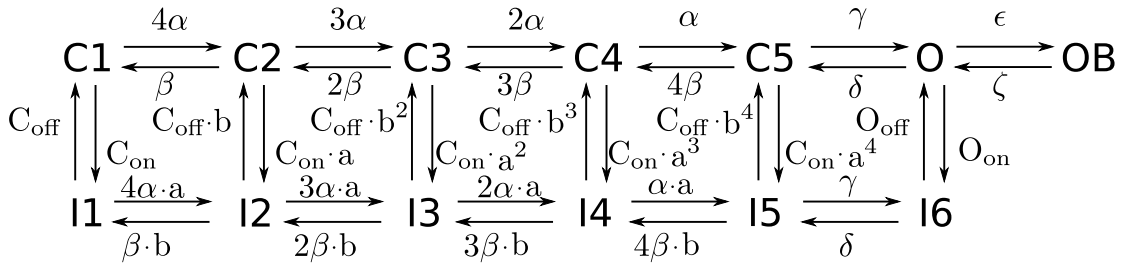

Figure 3.12: Markov model of the sodium current [102]

Furthermore, this Markov model accounts for the persistent sodium current too [116], that results from the steady-state occupancy of the O state.

Although there are other Markov models of the sodium current [10, 96, 125], the version shown in Figure 3.12 is the most extensively used in bibliography

[47, 97, 102, 116, 148]. Then, it was used as a template to the sodium current of Mes V neurons, whose complete details can be read in appendix C. In fact, there was a good agreement between the state-space model and data, but the increased complexity of the model is not compensated by any new astounding feature. Then, the Markov model of the Mes V sodium channel will not be included in the full neuron model, but a simpler HH one. In general, a HH model of the sodium current can be written as:

$$I_{Na} = \bar{g}_{Na} m^q h (V - E_{Na}) \tag{3.10}$$

with $q \in \mathbb{N}$ (usually q=1 or 3). The variables m and h are governed by standard HH differential equations.

The first step is to describe the inactivation variable h. The voltage clamp protocol to do that consists in applying long prepulses of varying voltages V_1 and then stepping it up to a very depolarized voltage V_2 (Figure 3.13(A) and (B)), where m is assumed to be saturated ($m_{\infty 2} = 1$). Given that the inactivation is slower than the activation ($\tau_m \gg \tau_h$), it can be assumed that $h(t) \simeq h_{\infty 1}$ during some time $t \gg \tau_{h2}$, after the step onset. Then, the sodium current is approximately described by:

$$I_{Na} \simeq \bar{g}_{Na} m(t)^q h_{\infty 1} (V_2 - E_{Na}) \tag{3.11}$$

where the subscripts 1 and 2 denote that the functions $h_{\infty}(V)$ and $\tau_h(V)$ are evaluated at $V = V_1$ and $V = V_2$, respectively. Now, it is straightforward to compute the steady-state inactivation curve $h_{\infty}(V)$ from the equation (3.11), as the normalized quotient between the peak current (where $m \simeq 1$) and the driving force:

$$h_{\infty}(V) = \frac{I_{Na}}{\bar{g}_{Na} m_1^q (V_2 - E_{Na})} \simeq \frac{I_{Na}}{\bar{g}_{Na}(V_2 - E_{Na})} \tag{3.12}$$

The resulting $h_{\infty}(V)$ (not normalized in Figure 3.13 (C)) is a sigmoid-like function, as expected, with a half-maximum voltage $V_{1/2}$ = -76.6 mV and slope k = -8.6 mV. Although the slope is close to previously reported values, the value of $V_{1/2}$ is very hyperpolarized compared to the values found by Wu et al [186] and Enomoto et al [41]:

	$V_{1/2}$ (mV)	k (mV)
Experimental recordings	-76.6	-8.6
Wu et al [186]	-60.1	-7.1
Enomoto et al [41]	-61.9	-9.5

Table 3.2: Comparisson between reported values of the sodium steady-state inactivation function $h_\infty = h_\infty(V)$.

On the other hand, the inactivation time constant $\tau_h(V)$ can be found fitting the experimental data shown in Figure 3.10 (A). In this case, the time constants from some non selected neurons (because of the quality control on the *activation protocol*) are also displayed in Figure 3.13 (F), as a control. Interestingly, these four neurons presented faster inactivation times, but saturated at the same value as the selected neuron: $\tau_{h\min}(V) = 0.3$ ms. The time constants can be fit by:

- Selected neuron ("with hepes" in (F)): $\tau_h(V) = 0.3 + 11.1 e^{-\left(\frac{V+55.1}{17}\right)^2}$

- Non selected neurons ("without hepes" in (F)): $\tau_h(V) = 0.3 + 5 e^{-\frac{V+50}{10}}$

However, given that the only valid *activation protocol* current traces comes from the selected neuron, the full characterization of the sodium current will continue with the corresponding τ_h, by dividing the current traces (Figure 3.10 (A)) by the inactivation variable $h(V_2, t)$:

$$h_2(t) = h_{\infty 2} + (h_{\infty 1} - h_{\infty 2}) e^{-\frac{t}{\tau_{h2}}}, \tag{3.13}$$

here again the pre and post-step voltage is denote by 1 and 2, respectively. From the *activation protocol*, the variable $m(t)$ can be obtained for each voltage V_2 as:

$$m_2(t) = \left(\frac{I_{Na}}{\bar{g}_{Na} h_2(t)(V_2 - E_{Na})}\right)^{\frac{1}{q}} = m_{\infty 2} + (m_{\infty 1} - m_{\infty 2}) e^{-\frac{t}{\tau_{m2}}} \tag{3.14}$$

The equation (3.14) should saturate at $m_2 = m_\infty(V = V_2)$, leading to the steady-state curves shown in the Figure 3.14 (A1, B1, C1).

Nevertheless, the resulting traces $m_2(t)$ do not display the expected exponential behaviour: they start decaying after some milliseconds as shown in Figure 3.14 (A2, B2, C2), probably because of a slower second inactivation process, related to the resurgent current. Therefore, only the exponential onsets (after the artifact) are the useful sections of the traces (shown in dotted boxes in Figure 3.14 (A2, B2, C2)). Fitting them (A3, B3, C3), the activation time constants τ_m can be found for $q = 3$ and $q = 5$, wheras $q = 1$ does not fit most of the traces. Figure 3.14 (B4, C4) show that τ_m is almost constant in voltage. Table 3.3 summarizes all this information.

	$V_{1/2}$ (mV)	k (mV)	mean τ_m (ms)
Experimental recordings $q = 1$	-26.5	4.5	1.16^4
Experimental recordings $q = 3$	-32.4	5.6	0.16
Experimental recordings $q = 5$	-34.1	5.7	1.16
Wu et al [186]	-43.4	5.0	not reported
Enomoto et al [41]	-32.9	6.1	not reported

Table 3.3: Activation parameters for different exponents q and previous models: half-maximum voltage $V_{1/2}$, slope k and mean activation time τ_m.
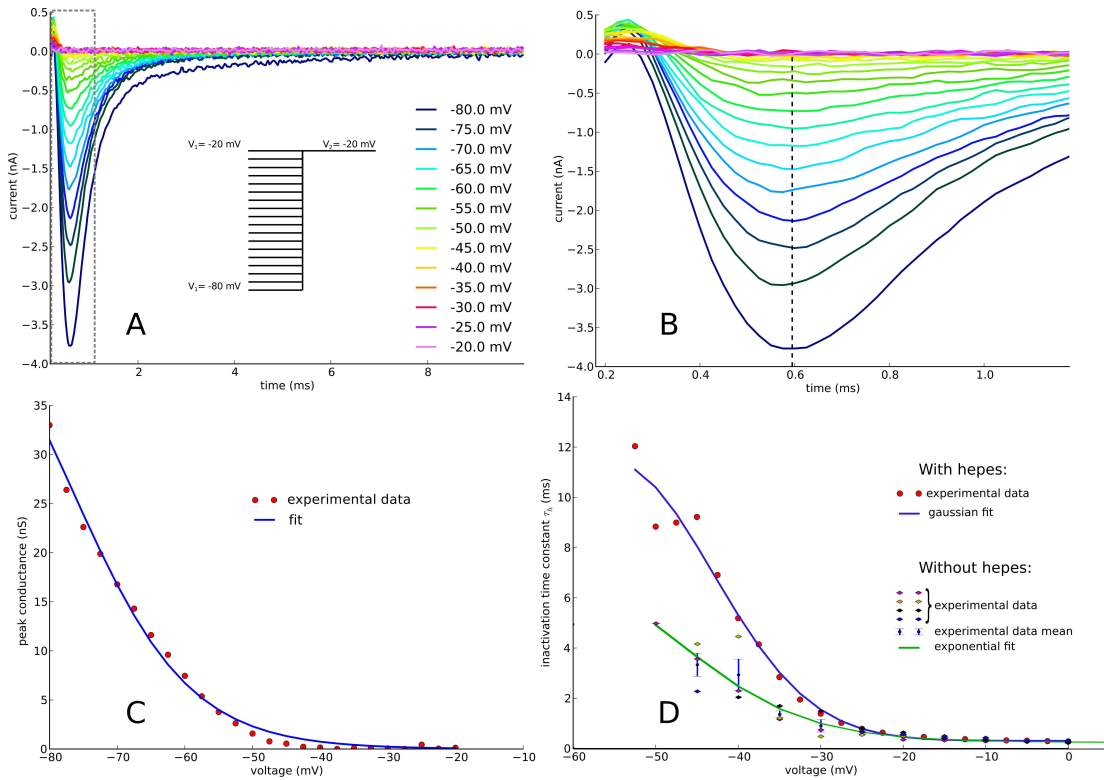

Figure 3.13: Measurement of inactivation according to HH formalism. Figure A shows the current recordings from the voltage clamp protocol displayed as inset: voltage ranging from -80 to -20 mV is stepped to -20 mV. Figure B (zoom of the dotted rectangle in A) shows that the time to peak is almost constant (dotted vertical line), meaning that all the curves reach the same voltage $V_2 = 20$ mV and checking the quality of voltage clamp. The peak currents are a non normalized version steady-state inactivation curve h_∞ (C), fitted with a sigmoid-like function, with a $V_{1/2} = $ -76.6 mV and $k = $ -8.6 mV. Finally, figure D shows the inactivation time constant for the best quality recording (measured in presence of hepes and TTX 10 nM) and for 4 other recordings, along with their corresponding fits.
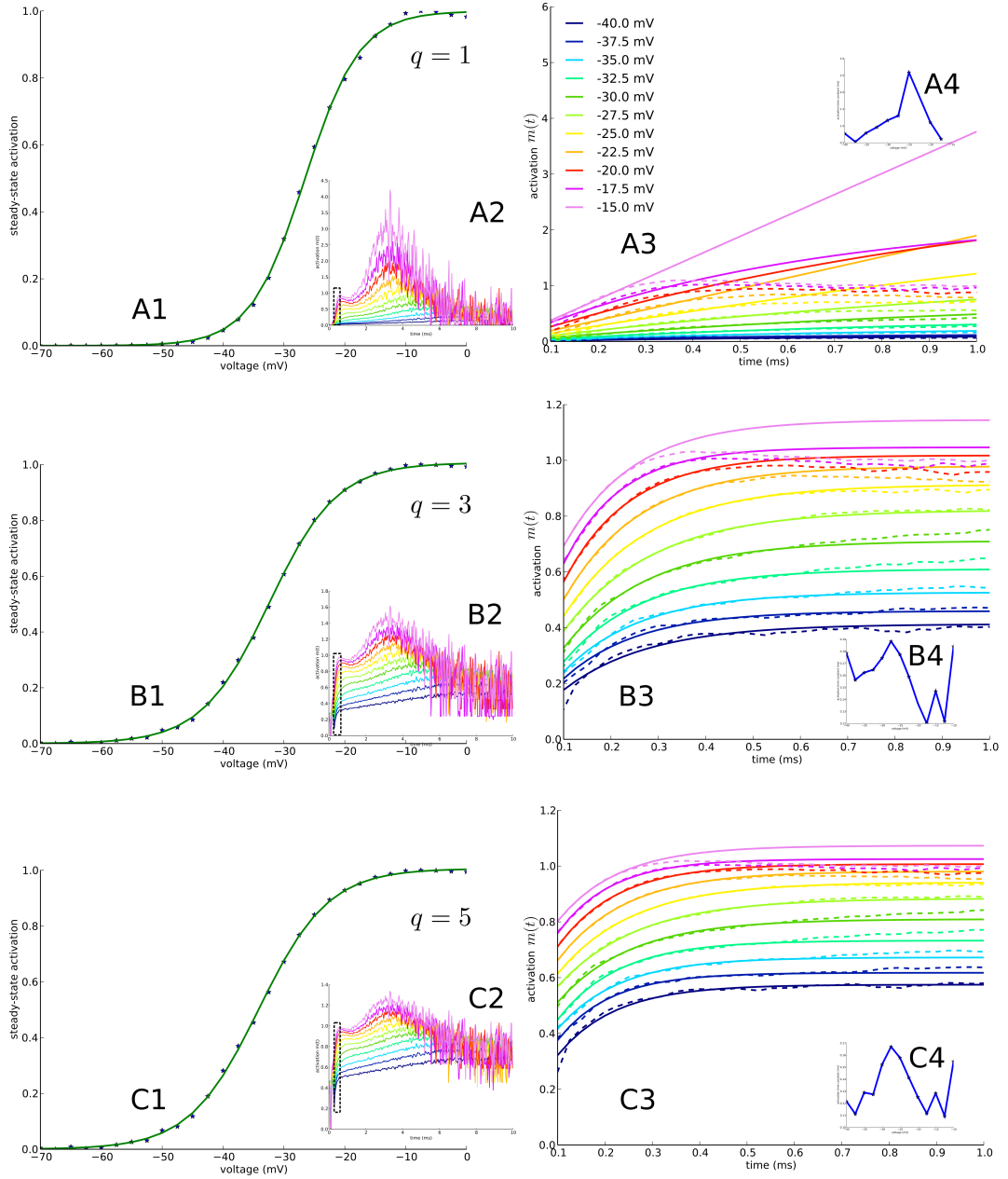
Figure 3.14: Characterization of the activation variable m, for different exponents q=1,3 and 5 arranged horizontally as panels A, B and C, respectively. A1, B1 and C1 show the steady-state activation curves m_∞ and their fittings. A2, B2 and C2 are the activation curves (see equation (3.14), whereas A3, B3 and C3 denote zooms in the dotted regions, with the experimental data and the corresponding exponential fits. Finally, A4, B4 and C4 present the activation time τ_m.

In addition to simulations from the three models with different activation exponents $q = 1, 3, 5$, two more simulations were also made: one using the steady-state inactivation curve from Enomoto et al [41] and the other with the inactivation time constants from the recordings "without hepes" (Figure 3.13). The results are displayed in Figure 3.15. Unless the model with $q = 1$, all the other present a general behaviour similar to the experimental recordings. Coherently, the largest error is found with $q = 1$. Both models with $q = 3$ and $q = 5$ are the best fits within different voltage ranges. Changing the time constant increases the error (C), as expected, because it does not correspond to this recording. However, moving the steady-state inactivation h_∞ does not affect too much the error.
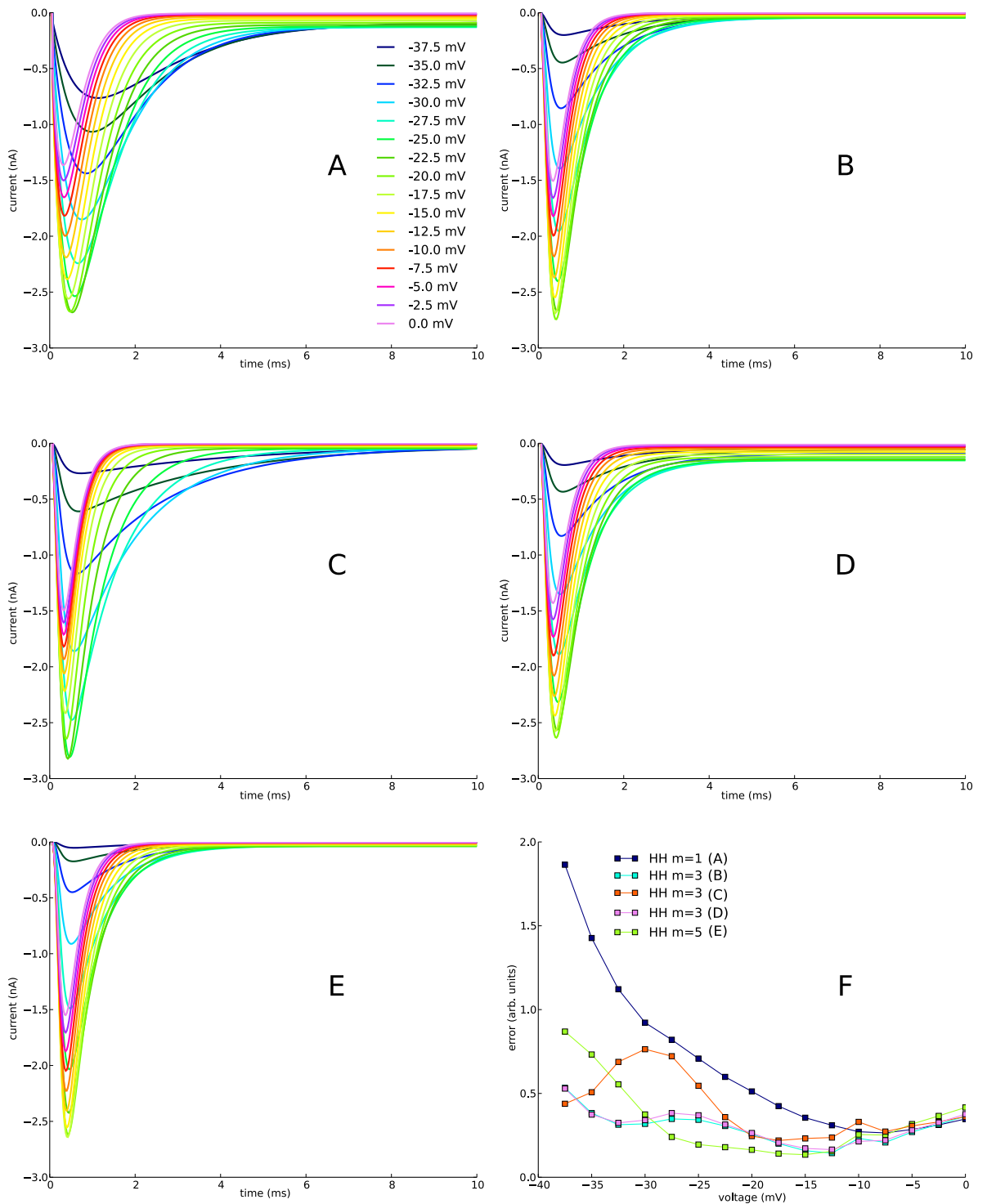
Figure 3.15: Simulated traces for the HH models: A is for $q = 1$; B, C and D for $q = 3$ and E for $q = 5$. While B uses the inactivation steady-state curve $h_\infty(V)$ and time constant $\tau_h(V)$ shown in Figure 3.13, C uses the time constant denoted as "without hepes", D the $h_\infty(V)$ measured by Enomoto et al [41]. F shows the error curves for all the traces.

3.4 Summary

In this chapter, two ionic currents were modelled from experimental data. In the case of the hyperpolarization-activated current I_h, a standard HH model was built, both from control conditions and in presence of cGMP. It was found that cGMP modulates I_h, moving its steady-state activation curve to depolarized values and reducing its time constant, with possible functional implications, that will be explored in the following chapters.

The sodium current was more difficult to study, due to its complexity. Experimental recordings were analyzed carefully, in order to check their quality. After that, only one in seven neurons were useful to develop a model of the sodium current. Markov models were implemented to represent for the first time Mes V resurgent sodium current. Standard HH models were also built. The resulting models fit the data better than a previous one and will be used in the following chapters, although it was not possible to really verify their validity with more data. In addition to that, some points remain open, such as parameter identifiability and their relation with the molecular structure of the sodium channel.

Chapter 4

Mesencephalic trigeminal neuron model

4.1 Introduction

This thesis is centered on the modeling and analysis of rat mesencephalic trigeminal neurons. These are sensory neurons, located in the mesencephalic trigeminal nucleus, responsible for carrying information from masticatory muscle spindles and periodontal ligament receptors [151]. Their morphology is called pseudounipolar [94]: they have an approximately spherical soma without dendrites, connected to an axon that is composed by two branches: one going to the periphery (the origin of the sensory stimuli) and the other to more central regions of the brain [157,158]. Unlike other sensory neurons, the soma of these cells is located in the central neuron system. Their projections reach the thalamus, the trigeminal motor nucleus (closing a reflex arc) and other brainstem nuclei [182]. On the other hand, they receive several synaptic inputs at the soma, allowing them to act as interneurons too [107,178].

The simple morphology of Mes V neurons contrasts with the complexity of the mechanisms that control their behaviour, such as their ionic conductances, the electrical coupling between them [9, 33] and the synaptic inputs mentioned before. The aim of this chapter is to review all these components, in order to build a biologically realistic conductance-based model of the Mes V neurons. While transient sodium I_{NaT} and hyperpolarization-activated I_h currents were characterised in Chapter 3, the other components will be taken from bibliography. Model parameters will be fitted using evolutionary algorithms, using experimental data properties.

4.2 Calcium currents

Del Negro and Chandler [133] recorded plateau-like action potentials in Mes V neurons, sensitive to Cd^{2+}, a calcium channel blocker. These long-lasting depolarizations were unconvered by blocking potassium currents with 20 mM tetraethylammonium (TEA). However, they did not characterise this current, using models

developed for other sensory neurons: low-threshold and high-threshold calcium currents (I_{CaL} and I_{CaT} respectively).

Several years after, Enomoto et al [42] found that calcium currents are minimal during the interspike interval. Then, Yang et al [188] studied the role of calcium currents in Mes V neuron's behaviour, by blocking them with 100-300 μM Cd^{2+}. They did not found any effect of these currents, neither in the spike threshold nor the firing frequency. In conclusion, calcium currents can be neglected in the full Mes V neuron model.

4.3   Potassium currents

Unlike calcium, potassium currents play an important role on Mes V neurons behaviour, modulating their excitability. In particular, the repetitive firing [80,133, 185] and the subthreshold frequency properties [33] of these neurons are directly linked with the strength (maximum conductances) of some potassium currents. Given that modeling of potassium currents from experimental recordings failed, due to voltage-clamp errors (not shown), the following description of potassium currents is based on literature.

4.3.1 Ca^{2+}-activated potassium current

There is a TEA-sensitive calcium-activated potassium current that was measured by Del Negro and Chandler [133], by blocking Ca^{2+} with Cd^{2+} or using low-calcium solutions. However, it can be argued that this current has little functional significance, given that it would produce long-lasting afterhyperpolarizations that are not reported in Mes V neurons [138]. In addition to that, there is almost no information about its dependence on Ca^{2+}, given that Del Negro and Chandler made a model only valid for control conditions. Therefore, this current was not included in the model.

4.3.2   Inward rectifier

The inward rectifier I_{KIR} is a persistent potassium current that get activated by hyperporization. Tanaka et al measured it by applying step voltage commands from -60 to -140 mV, in control condition and in presence of Ba^{2+} (I_{KIR} blocker) [170], finding that it starts to activate at voltages below -100 mV, getting completely activated at -140 mV. In addition to the extremely hyperpolarized activation voltage range, its maximum conductance spans from 0.5 to 2 nS. Thus, this current can be ignored in the model without any important functional consequence.

4.3.3 Delayed rectifier

The delayed rectifier does not correspond to only one type of channel, but to several ones that share the same functional characteristics, being widely present in axons and also in the somatic membrane [71]. In the case of Mes V neurons, there is immunohistochemical[1] evidence of the presence of potassium channels from the subtype Kv2.1 (one of the main responsibles for the delayed rectifier) in both soma and axons [156]. Perhaps because of its ubiquity [126], it was the potassium current described by Hodgkin and Huxley [74] (see the subsection 2.3.1).

It contributes to shorten the action potential duration by producing a "delayed" outward current that "rectifies" (repolarizes) the membrane potential. Using recordings from 4 cells and step depolarizations from a holding potential of -40 mV, Del Negro and Chandler modelled this current using HH formalism [133]:

$$I_{DRK} = \overline{g}_{DRK} n \left(V - E_K \right) \tag{4.1}$$

where the activation variable n satisfies a typical differential equation of a current from a conductance-based model:

$$\frac{dn}{dt} = \frac{n_\infty - n}{\tau_n} \tag{4.2}$$

The activation curve $n_\infty(V)$ is a sigmoid-like function (see equation (2.8)), whose half activation voltage is $V_{1/2}$=-4.2 mV and its slope is k_n=12.9 mV. Given that the activation curve is almost zero at resting potential (-55 mV), the delayed rectifier has little effect on the fine tune of Mes V excitability [188]. Its function is related to the steady-state stabilization of membrane potential, as it is demonstrated by the plateau-like depolarizations elicited by its suppression (see section 4.2).

Nevertheless, the time constant τ_{DRK} reported by them does not fit the time constant shown in their article. For comparisson, Figure 4.1 displays a reconstruction of the data[2] and the model presented in their article, as well as the model by Belluzzi and Sacchi [13] of the delayed rectifier of the rat sympathetic neurons[3]. On the other hand, a later modeling article by Liu et al [113] used a constant τ_{DRK}=10 ms. Fortunately, numerical simulations (not shown) proved that this difference in time constants is not crucial to get Mes V neurons' behaviour. Then, the simplest option will be used: a constant τ_{DRK}.

---

[1]Immunohistochemistry is a technique used to identify specific molecules, through antibodies that bind them selectively and can be seen via a visualization technique.

[2]Graphically reconstructed from the figure 7B in [133].

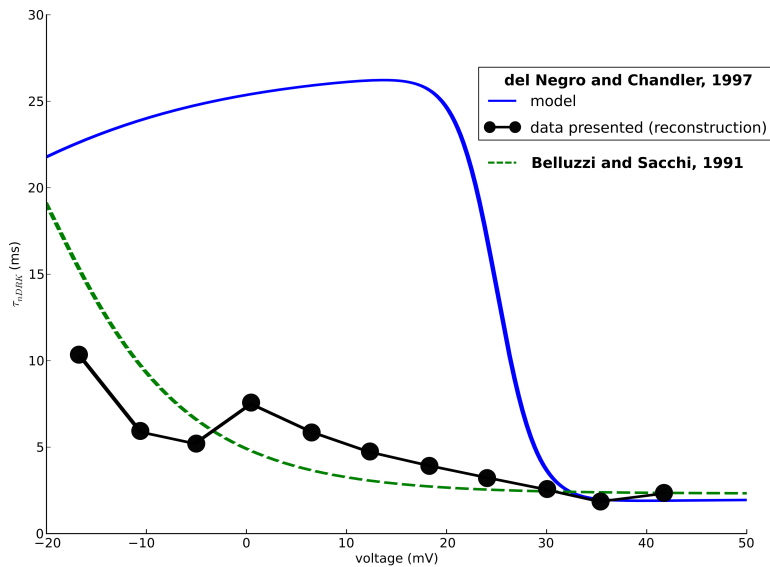[3]The temperature in both articles was the same: 37°C.

Figure 4.1: Comparisson between the reconstructed data from the article by del Negro and Chandler and their model [133]. A previous model by Belluzzi and Sacchi [13] presents a better fit to the data, even though it comes from another neuron type.

4.3.4 Low-threshold currents

The classic example of low-threshold potassium current is the A-type current, that was first described by Connor and Stevens [29, 30], being 4-aminopyridine-sensitive [172] and presenting inactivation. Given its subthreshold activation, it is active in the interspike interval, helping to modulate repetitive firing [29, 71]. Mes V neurons also have low-threshold potassium currents, that have been shown as determinant for their excitability [133] and resonance [185, 186]. For this reason, these currents have been studied in several articles, leading to different results that will be reviewed in this section and summarized in the Figure 4.2.

Del Negro and Chandler made the first complete study on Mes V outward currents [133]. Among them, they found two low-threshold potassium currents: a 4-AP-sensitive sustained current I_{4AP} and a slow transient outward current I_{toc-s} (also 4-AP-sensitive). Along with their different dynamics (I_{toc-s} closes after some time, whereas I_{4AP} not), the half-activation voltage $V_{1/2}$ of I_{4AP} is almost 10 mV below that of I_{toc-s}: -48 mV for the first one and -37 mV for the other.

From the same research group, Hsiao and coworkers [80] made a complete study of the channels that produce low-threshold potassium currents. They used a α-dendrotoxin (α-DTX) to block only channels composed by Kv1.1, 1.2 and 1.6 proteins, finding a current that shows no inactivation during 1-s time periods, with $V_{1/2}$ = -36 mV. According to literature, this current is also sensitive to very low concentrations of 4-AP [187]. Then, it should be the I_{toc-s} reported by Del Negro and Chandler but with different kinetics probably due to different proteins

coupled to the Kv1 units [27]. The time constant of this current does almost not change in the voltage range from -60 to -30 mV: going from 2 to 4 ms. Using inmunohistochemical methods, Hsiao et al confirmed a previous result from Saito et al [156]: these three channels are expressed in Mes V somata, but not in the stem axon.

Finally, Yang et al [188] used the same pharmacological conditions that Del Negro and Chandler utilized for recording the sustained 4-AP-sensitive current, finding the same half-activation values and slightly different slopes. They also studied a population of Mes V neurons with less excitability (also known as class 3, see chapter 6), finding a negative shift of 6 mV in half-maximal activation voltage $V_{1/2}$.

In conclusion, according to the steady-state activation curves (Figure 4.2) there are two different low-threshold potassium currents, both sensitive to 4-AP but only one to α-DTX too. However, only one of them (whose $V_{1/2}$ = -48 mV) is found when 4-AP is applied. Then, it seems that the current sensitive to α-DTX is negligible compared to the other. Therefore, as a first approximation, only I_{4AP} current will be included in the basic Mes V neuron model, whose consequences can be checked with available experimental recordings in control conditions and in presence of 4-AP.
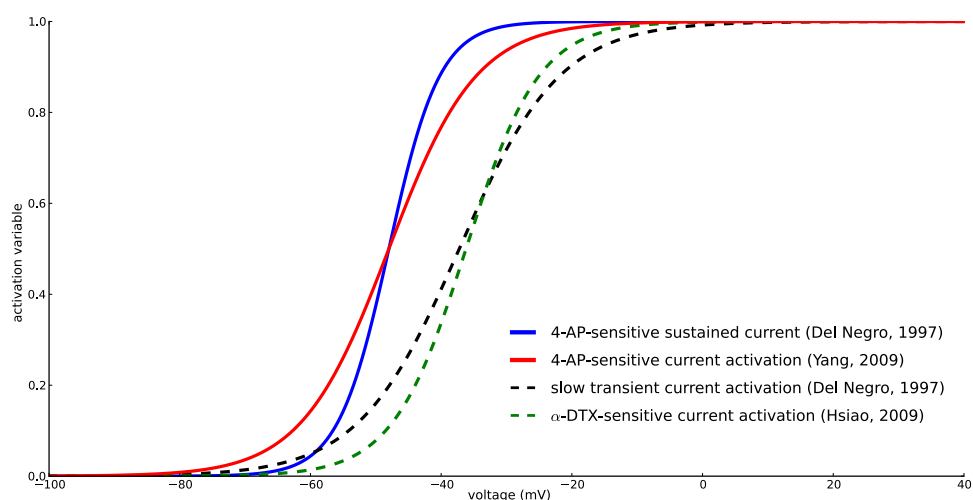

Figure 4.2: Summary of the steady-state activation curves of low-threshold potassium currents. Note that the α-DTX-sensitive current activation curve corresponds approximately to the activation curve of the slow transient current (dashed). The same can also be said for the 4-aminopyridine-sensitive currents (continuous lines).

4.3.5   Fast high-threshold current

Del Negro and Chandler found another potassium current, with relatively fast kinetics, very high threshold ($V_{1/2}$=5 mV) and not sensitive to 4-AP concentrations

that block other potassium currents [133]. This current meets the properties of channels from the Kv3 family [12, 93], that have been already found by immuno-histochemical methods in Mes V neurons [156]. Due to its high-threshold, it will be responsible for membrane potential repolarization after a spike. However, as it will be shown in section 4.4.3, its time constant is too slow to generate Mes V action potentials and should be fitted.

4.3.6 Summary of the ionic currents

In conclusion, six ionic currents will be included in the Mes V neuron model: transient and persistent sodium I_{NaT} and I_{NaP}, hyperpolarization-activated I_h, delayed rectifier I_{DRK}, 4-aminopyridine-sensitive I_{4AP} and high-threshold potassium I_{Kv3}. The next step is to assemble them in a single model, with two compartments (soma and axon), implemented in the NEURON simulator [21].

4.4 Model fitting

After defining the ionic currents to be included in the Mes V neuron model, it is necessary to find how do they get together in a single model that can be validated with experimental data. Although it is possible to look for all of the model parameters at the same time, it could be very computationally expensive. A cheaper computational approach is to follow a sort of *divide et impera* (divide and conquer) strategy [72, 152], dividing the parameter space in regions with lower dimension, simplifying the process to find them. This principle applied to the Mes V neuron model defines roughly three sets of parameters that can be found in cascade:

1. **Passive and geometrical parameters**: Axon length L, membrane and internal specific resistivities (R_m and R_i, respectively).

2. **Subthreshold ionic conductances**: Maximum conductances of persistent sodium $\overline{g}_{NaP}$, hyperpolarization-activated $\overline{g}_h$ and 4-AP-sensitive potassium $\overline{g}_{4AP}$. Leak conductances from soma and axon will be adjusted too, using the R_m value found before.

3. **Suprathreshold ionic conductances**: Maximum conductances of the delayed rectifier $\overline{g}_{DRK}$, transient sodium $\overline{g}_{NaT}$ and high-threshold potassium $\overline{g}_{Kv3}$. The time constant of the Kv3 current τ_{Kv3} need to be fitted too in this step.

Figure 4.3 summarizes the peeling process, indicating which parameters are found in each step. In the next sections, the model parameters will be found according to this scheme.

The passive and geometrical parameters will be estimated by fitting analytical expressions (from a simplified linear model) to experimental recordings. Unfortunately, the analytical approach cannot be taken for the rest of the parameters,
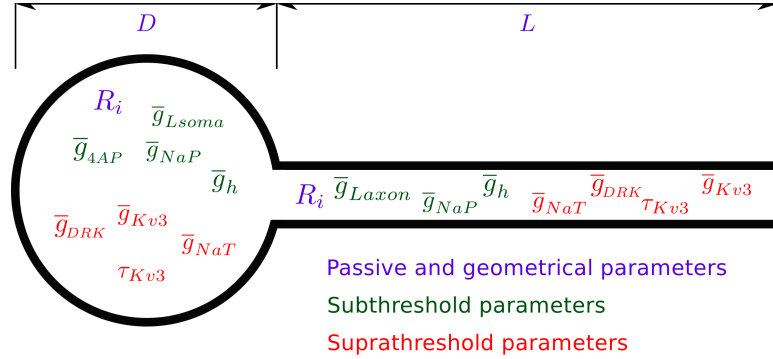
Figure 4.3: Schematic representation of the parameters' cascade. D is the soma diameter, while d and L are the axon diameter and length.

that should be found using numerical algorithms. Tuning parameters by hand is the most widely used procedure [132, 142, 164], but it is a very complex task, due to the nonlinear behaviour of the model. On the other hand, there are several automatic optimization algorithms that have been employed to fit conductance-based neuron models to experimental data (for reviews, see [3, 173]): classical gradient descent [16], parameter space exploration (brute force search) [143, 171], bifurcation analysis to map neuron's dynamics [61], etc. In particular, evolutionary algorithms have been intensively used in the last years [2, 8, 38, 39, 99, 168], given that they can be less prone to fall in local minima than gradient descent, and are not so computationally expensive as brute force search or bifurcation analysis [142].

Hence, most parameters of the Mes V neuron model will be found by evolutionary algorithms [35], utilizing a Python library developed by Bahl et al [8]. Given that this method was not developed in this thesis, it will be fully explained in the appendix B and just briefly presented here. First of all, this procedure uses several optimization objectives, that will be defined later in this section. The method starts by generating a population of random solutions (whose parameters are random variations close to the initial guesses and vary within bounds). Then, they are pairwise compared in fitness and selected to fill a selection pool. Parents are randomly taken from this pool and their parameters are combined (through a crossover operator), in order to generate two children with new parameters. In order to increase the diversity of the solutions population, a mutation operator is applied. Finally, the fitness of each solution is measured for every objective. From the whole population, the procedure only takes those who are nondominating (i.e.: they are at least better than the other in one objective, but not worse in the remaining ones), ranking them and starting again with the selection step. The algorithm ends after N steps (called generations) or a stop-criterion is reached.

Instead of fitting individual experimental recordings, the objective will be to get close to the mean experimental values for 14 features obtained in voltage responses to current steps (the I-V curve), that define Mes V neurons' properties:

1. Resting membrane potential (RMP)

2. Input resistance R_{in}, defined as the slope of the linear fit between hyperpolarizing voltage responses' peaks and the injected currents.

3. Membrane time constant τ_m for an injected current step of -50 pA.

4. Final amplitude of the voltage response to an 200-ms current step of -400 pA and +100 pA.

5. Overshoot of the voltage response to a +100 pA current step.

6. Voltage after-hyperpolarization: minimum voltage after an action potential.

7. Spike amplitude and its duration at -20 mV.

8. Number of spikes at +300, +400 and +600 pA of 200-ms current steps.

9. Mean spike train frequency at +400 and +600 pA.

Actually, fitting individual traces and their derivatives was also tested, but its results were very poor, given that error functions are very sensitive to time shifts between experimental and simulated data. One way to deal with that is using phase plane analysis, that means fitting the traces in the plane $\left(V, \frac{dV}{dt}\right)$ [174]. However, this method is more suited to fit spike trains (and their subthreshold propagations in dendrites), which is not the typical case of Mes V neurons.

4.4.1 Passive and geometrical parameters

Mes V neurons can be simplified geometrically as a sphere (the soma) and a cylinder (the axon[4]), in the so-called ball-and-stick model, shown in Figure 4.4. Assuming that the membrane is only passive and its electrical properties are uniform along the neuron, it is possible to obtain analytical expressions for the voltage response to a current step in the soma. The soma is modelled as an isopotential sphere of diameter D, with lumped parameters: resistance R_s and capacitance C_s. From bibliography and photos, it is possible to estimate the axon diameter $d \sim 3$ μm approximately.

Unlike soma and axon diameters, it is quite difficult to measure axon length, ℓ, from photos, because it can vary a lot, given that Mes V neurons are contained in slices and their axons may be cut depending on their morphology. Then, minimum and maximum values for ℓ will be estimated from individual experimental recordings.

---

[4]Notice that this axon, of diameter d, is representing the two axonal branches of Mes V neurons: peripheral and central. The results from the model presented here can be applied to create two branches if their diameters $d_{peripheral}$ and $d_{central}$ satisfies: $d^{\frac{3}{2}} = d_{peripheral}^{\frac{3}{2}} + d_{central}^{\frac{3}{2}}$ [92]. This result will be used in the chapter 6.
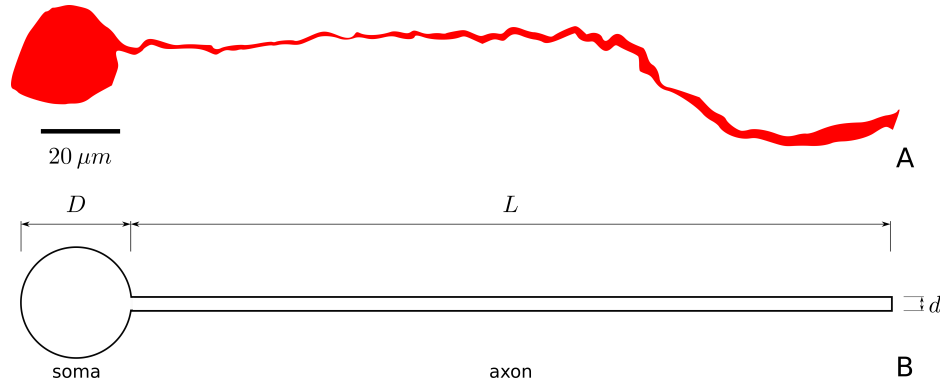
Figure 4.4: Neuron's morphology: experimental picture of a neuron marked with neurobiotin (A, adapted from [33]) and ball-and-stick model (B) with its geometrical parameters: soma diameter D, axon diameter d and length ℓ.

On the other hand, the axon is modelled as a finite cable made of passive components:

- r_i: internal (also called axial or cytoplasmatic) resistance (Ω/cm)

- r_m: membrane resistance ($\Omega.\text{cm}$)

- c_m: membrane capacitance (F/cm)

- r_o: extracellular resistance (Ω/cm), that is usually taken as zero

By using these parameters, the cable equation can be written as [129]:

$$\lambda^2 \frac{\partial^2 V_m}{\partial x^2} = \tau_m \frac{\partial V_m}{\partial t} + V_m \tag{4.3}$$

where $\lambda = \sqrt{\frac{r_m}{r_i}}$ is called the space constant and $\tau_m = r_m c_m$ is the membrane time constant. Space and time variables, x and t, are usually used by normalizing them with these two parameters: $X = x/\lambda$ and $T = t/\tau$.

The parameters r_i, r_m and c_m defined for a cable of radius a can be normalized, defining specific parameters independent of the geometry [92]:

- $R_i = \pi a^2 r_i$: specific intracellular resistivity ($\Omega.\text{cm}$)

- $C_m = \frac{c_m}{2\pi a}$: specific membrane capacitance (F/cm^2). Unlike other parameters, it is quite standard among neuronal types [58], varying from 0.7 [117] to 1.5 μF/cm^2 [74], with a mean value of 0.9 [26,58], that it is rounded up to 1 μF/cm^2 as a standard value in the NEURON simulator [21] and will be used as this in simulations.

- $R_m = 2\pi a r_m$: specific membrane resistivity ($\Omega.\text{cm}^2$). Note that $\tau_m = r_m c_m = R_m C_m$.

51

The input conductance of a finite cable is:

$$G_N = \frac{\pi}{2}\sqrt{\frac{d^3}{R_m R_i}} tanh(L) \tag{4.4}$$

For this model, the voltage response to a current step is:

$$V_m(T,X) = V(\infty, X) - \sum_{n=0}^{\infty} B_n cos\left[\alpha_n\left(L-X\right)\right]e^{-\left(1+\alpha^2\right)T} \tag{4.5}$$

where $B_n cos\left(\alpha_n L\right) = \frac{2B_0\tau_n/\tau_0}{1+(\alpha_n L)^2/(k^2+k)}$ and $\tau_0 = \tau_m$.

Now, let define the **axonic** to somatic conductance ratio $\rho = \frac{G_{Ax}}{G_S}$, that give the proportion of current that flow through the axon relative to the somatic one. The total input conductance G_N can be expressed as: $G_N = G_{Ax} + G_S = (1 + \rho) G_S$.

Equation (4.5) can be expressed as:

$$V_m(T,X) = C_0 e^{-t/\tau_0} + C_1 e^{-t/\tau_1} + \ldots + C_n e^{-t/\tau_n} \tag{4.6}$$

with $C_n = B_n cos\left[\alpha_n\left(L-X\right)\right]$ and $\tau_n/\tau_0 = 1/(1+\alpha_n^2)$.

By definition, $\tau_0 > \tau_1 > \ldots > \tau_n$. Then, the two first time constants can be used as a first approximation $V_m \simeq C_0 e^{-t/\tau_0} + C_1 e^{-t/\tau_1}$. These four parameters can be found by fitting the somatic membrane potential, as Figure 4.5 displays.

The normalized axon length L can be obtained from the following equation [92]:

$$\left|\frac{C_1}{(2C_0\tau_1/\tau_0) - C_1}\right| = cot(\alpha_1 L)\left[cot(\alpha_1 L) - 1/(\alpha_1 L)\right] \tag{4.7}$$

and then

$$\rho = -\frac{\alpha_1 cot(\alpha_1 L)}{coth(L)} \tag{4.8}$$

After deriving all the equations, it is time to find the parameters. The procedure starts by fitting the subthreshold voltage response to Equation (4.6), in order to find C_0, C_1, τ_0 and τ_1. The specific membrane resistance R_m is directly found using τ_0 and C_m (remember that is fixed at 1 μF/cm^2). On the other hand, the normalized axon length L is computed from equation (4.7) and then ρ from (4.8). The specific intracellular resistance R_i, space constant λ and axon length ℓ and soma diameter d are obtained from L, ρ, the input conductance G_{in} (computed as the quotient between the input current and the voltage response) and Equation (4.4).

4.4.2 Subthreshold ionic conductances

According to the half-activation values of the steady-state curves, the main ionic currents at subthreshold level are the persistent sodium I_{NaP}, 4-AP-sensitive
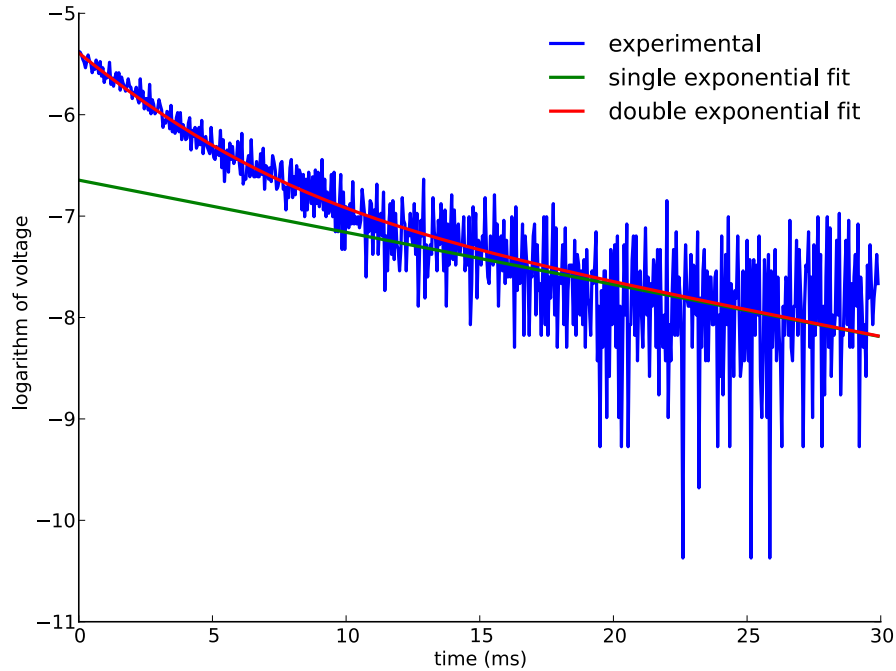
Figure 4.5: Geometrical parameters can be obtained from experimental recordings. The two slowest time constants τ_0 and τ_1 can be found by fitting of the logarithm of the voltage.

potassium I_{4AP} and hyperpolarization-activated I_h, as well as the leak current I_L. These currents and the previously estimated passive and geometrical parameters define a reduced Mes V neuron model. Unlike the passive ball-and-stick model, this new model is not completely homogeneous, due to the lack of I_{4AP} at the axon (see section 4.3.4). In order to compensate this assymmetry, leak conductances from axon and soma will be considered as independent parameters.

In this step, the maximum conductances of the ionic currents and axon length will be fitted using the first 6 features from the list presented at section 4.4, related to the response of the neuron to current steps from -400 pA to +100 pA. Although all the ionic currents have influence on all the features, some of them are decisive to generate specific properties. For example, a model without I_{4AP} cannot generate a depolarizing overshoot. Figure 4.6) displays a simulation of the model with a set of parameters obtained from the evolutionary algorithm routine.

The optimization technique was applied to the subthreshold Mes V neuron model 20 times, obtaining parameters' ranges that will be used as bounds for the next step.

4.4.3 Suprathreshold behaviour

In order to get the suprathreshold behaviour, the model incorporates the remaining ionics currents: delayed rectifier I_{DRK}, transient sodium current I_{NaT} and
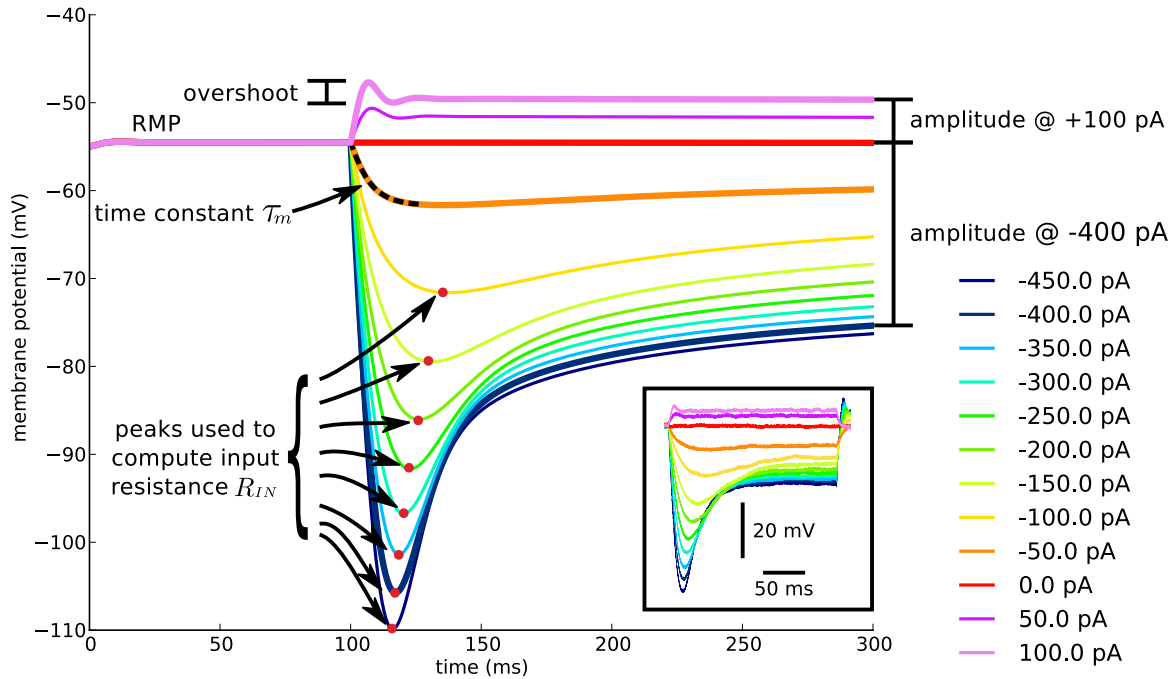
Figure 4.6: Simulation of subthreshold response of a reduced Mes V neuron model, with the qualitative features that are optimized. An experimental recording is shown in inset, for comparisson.

high-threshold fast potassium current I_{Kv3}. These last two currents are responsible for the action potential depolarization (I_{NaT}) and repolarization (I_{Kv3}). The transient sodium current I_{NaT} has been studied in detail in section 3.3: the best HH model (exponent $q = 3$) will be used.

Unlike I_{NaT}, Kv3 current is not so well described. In fact, the model reported by del Negro and Chandler [133] (section 4.3.5) presents two severe drawbacks. The first is that afterhyperpolarizations get smaller during repetitive firing, due to I_{Kv3} slow inactivation. Then, I_{Kv3} inactivation variable has to be taken out, resulting in the following expression for this current:

$$I_{Kv3} = \overline{g}_{Kv3} m^3 \left(V - E_K \right) \tag{4.9}$$

where m is the activation variable that evolves according the typical HH formalism (Equation (2.6)).

The second problem is that I_{Kv3} generates action potentials three times broader than the experimental ones. Several options were explored unsuccessfully to overcome this: changing the activation exponent blocks spike generation, shifting downwards the half-amplitude voltage $V_{1/2m}$ of the steady-state activation curve $m_\infty(V)$ produces action potentials with smaller amplitudes, whereas increasing its slope k_m generates weird spikes or even plateaux. The remaining alternative is to

deal with its time constant τ_{Kv3}, that was expressed originally as:

$$\tau_{Kv3}(V) = \tau_{Kv3\min} + \tau_{Kv3\exp}.e^{-\frac{\left(V-V_{\tau_{Kv3}}\right)}{k_{Kv3}}} \tag{4.10}$$

where $\tau_{Kv3\min}$ =1.5 ms, $\tau_{Kv3\exp}$ =15.2 ms, $V_{\tau_{Kv3}}$=-57 mV and k_{Kv3}=31 mV. From these parameters, $\tau_{Kv3\min}$ and $\tau_{Kv3\exp}$ were included in the optimization procedure, leading to better results. Figure 4.7 shows how spike shape improves in the new I_{Kv3} model, compared to the original [133] and to two models taken from other neuron types (auditory [184] and Purkinje [5]).
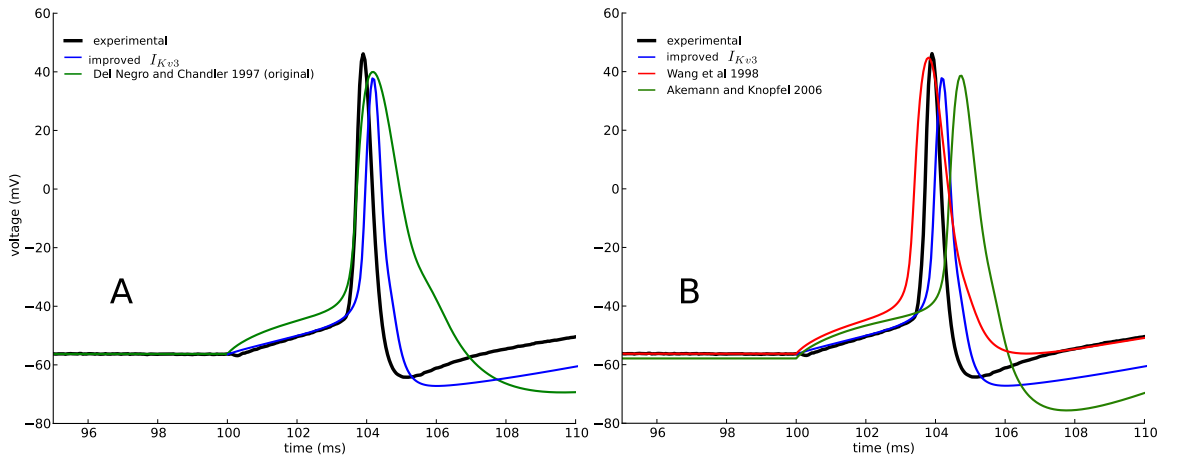

Figure 4.7: Experimental and simulated spikes generated in response to a current step of 350 pA. Given that the original Del Negro and Chandler model [133] (A) generates a very wide action potential, that is improved after adjusting the time constants $\tau_{Kv3\min}$ and $\tau_{Kv3\exp}$. Alternative Kv3 current models [5, 184] (right) do not work better (B).

Notice the time difference between the experimental spike and the simulated one using the improved I_{Kv3} model. Indeed, this slight time shift (due to minor differences in spike threshold and depolarizing slope) may give a very large root mean square error, in spite of the similarity between the traces. This fact supports the idea of fitting using quantitative features and not individual experimental traces.

Table 4.1 compares the final results from the whole Mes V model to those from experimental data. There is a good agreement between experiments and simulations in almost all the features: only the number of spikes seems to be different. That is caused by the slightly increased excitability of the model, that generate repetitive spiking when Mes V neurons just spike 2 or 3 action potentials, probably due to a decreased outward current. Increasing I_{4AP} may improve this situation (and also generate more overshoot), but with unwanted side effects: increase of the time constant τ_m, reduction of the input resistance R_{IN} and resting membrane potential. Then, it is better to use the trade-off solution presented in Table 4.1. The final set of parameters is presented in appendix **??**.

Parameter	Experimental	Model
Resting membrane potential (mV)	-54.7 ± 0.5	-55.2 ± 0.2
Input resistance R_{IN} (MΩ)	118.3 ± 8.1	114.9 ± 1.1
Time constant τ_m (ms)	7.4 ± 0.8	6.5 ± 0.2
Final voltage response @ I_{inj}=-400 pA (mV)	-17.4 ± 1.1	-19.2 ± 0.2
Final voltage response @ I_{inj}=+100 pA (mV)	4.3 ± 0.3	4.1 ± 0.2
Overshoot @ I_{inj}=+100 pA (mV)	2.5 ± 0.3	2.3 ± 0.3
Voltage after-hyperpolarization value (mV)	-7.4 ± 0.7	-8.7 ± 1.1
Spike amplitude (mV)	93.3 ± 1.9	97.9 ± 1.8
Spike duration @ -20 mV (ms)	0.67 ± 0.06	0.66 ± 0.03
# spikes @ I_{inj}=+300 pA	7.1 ± 2.3	17.8 ± 0.6
# spikes @ I_{inj}=+400 pA	8.9 ± 2.8	22.5 ± 0.6
# spikes @ I_{inj}=+600 pA	11.6 ± 3.4	31.0 ± 1.0
Spike train frequency @ I_{inj}=+400 pA (Hz)	119.0 ± 7.9	111.4 ± 3.2
Spike train frequency @ I_{inj}=+600 pA (Hz)	139.0 ± 9.2	152.4 ± 5.4

Table 4.1: Mes V neuron quantitative features: experimental (n=15) and simulations from the whole model (n=35).

4.5 Comparisson with previous models

There are three previous complete models of Mes V neurons published. The first one was a single-compartment model, with 9 ionic currents and 17 differential equations, developed by del Negro and Chandler in 1997 [133]. It did not present neither I_{NaP} nor I_{4AP}, but two calcium currents and one calcium-dependent potassium current. In addition to that, they also modelled calcium dynamics with four additional nonlinear differential equations. Although several ionic currents are studied in detail from experimental recordings (sections 4.2 and 4.3), their transient sodium model proved to be quite inaccurate in section 3.3. In addition to that, their capacitance value (C=21 pF) is approximately a half of the reported value for rats at the same age range: 36 pF (2 days old rats) to 46 pF (7 days), making their model more excitable and with faster action potentials.

Chandler and his team continued working on Mes V neurons, generating the next mathematical model in 2005, in collaboration with the legendary Izhikevich [186] (who used the experimental data later as examples in his book [88]). The new model was very simple, accounting only for the main currents: leak, I_{NaP}, I_{4AP} and I_{NaT}. Years later, another team picked up this model, adding two "supporting actors": I_h and I_{DRK} [113]. In this case, the capacitance value was within experimental range.

The model developed in this thesis adds one more compartment (axon), instead of only the soma. The question now is whether the multi-compartment model developed in this thesis is worth this increased complexity or not. Does this model

contribute to the state-of-the-art on neuron modelling or not? The answer is summarized in Figure 4.8, where previous Mes V neuron models are compared to experimental data and the new model. There was a minor adjustment of the maximum hyperpolarization-activated conductance $\overline{g}_h$ in the new model, in order to achieve a better fit to the recordings from one individual neuron.
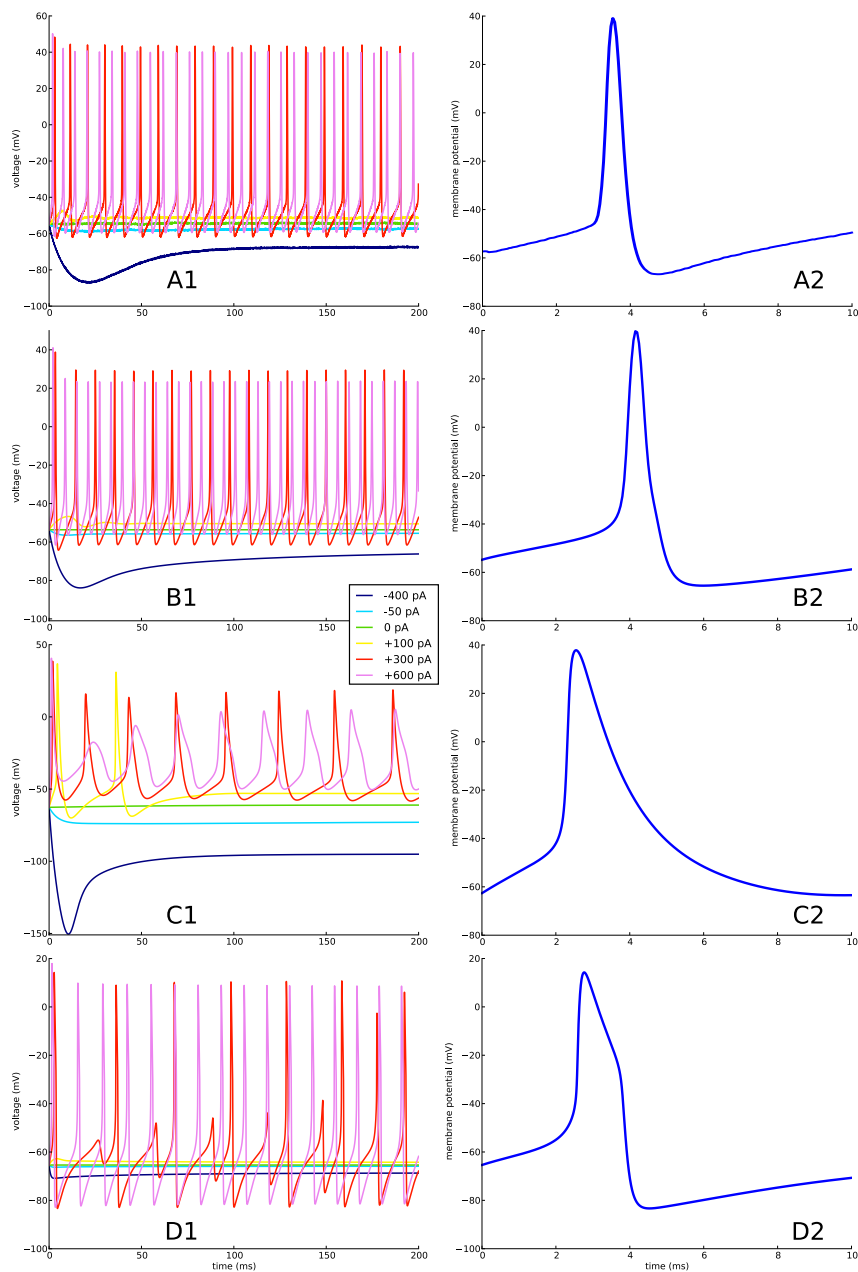
Figure 4.8: Comparisson between experimental data and simulations, for several Mes V neuron models. The left column displays the Mes V neuron response under a current clamp protocol (color reference is the same for all): experimental (A1), model developed in this thesis (B1), del Negro and Chandler [133] (C1) and Liu et al [113] (D1). The right column shows the spikes corresponding to each row.

4.6 Synaptic inputs

Mes V neurons collect sensory information from masticatory muscle spindles and periodontal ligament receptors that are innervated by their peripheral axons [151]. They also receive chemical synaptic inputs at the soma, from several regions of the central nervous system, such as amygdala [159], raphe nuclei [112], hypothalamus [108], substantia nigra [130] and other trigeminal neurons [178]. Although some of the neurotransmitters used have been characterised (nitric oxide [140], histamine [108], serotonin [112] and GABA [189]), Mes V neurons seem to be quite chemically heterogeneous [107]. Then, the role of these synaptic inputs is not clear: they may make Mes V neurons act as interneurons, but when and why?[5] Therefore, somatic inputs will not be studied in this thesis, but only some effects of I_h modulation by cyclic GMP (that may be a product of nitric oxide or histamine presence [160]). The focus will be to understand how Mes V neuron process peripheral inputs, which will be modelled as axonal excitatory synapses (equation (2.18)).

On the other hand, Mes V neurons can be connected between themselves through electrical synapses [9]. These electrical synapses are membrane pores, composed by a protein called connexin36 (Cx36), that allow bidirectional ion flow between coupled neurons. Neurons are usually connected in pairs, though some cases of triplets and quadruplets were also found [33]. On the other hand, the only presence of Cx36 does not always imply the coupling between two neurons, given that the pores may be closed (Figure 4.9).

Electrical coupling generates some astounding behaviours that have been experimentally tested by recording pairs of connected Mes V neurons simultaneously. For example, subthreshold signals with specific frequency content are less attenuated than DC when they pass from one neuron to another. Furthermore, Mes V neuron are more efficient recruiting electrically coupled neurons than other neuron types. However, these properties are not only caused by the coupling: the electrical properties of the membrane are also involved [33]. In the next two chapters, this interaction between electrical coupling and membrane properties will be studied, in order to explain these behaviours.

---

[5]There is recent evidence that Mes V neurons decrease the synaptic strength of GABA inputs during repetitive firing [190]. Therefore, at least in this case, the neuron favours its sensory input and does not "listen" central nervous system orders.
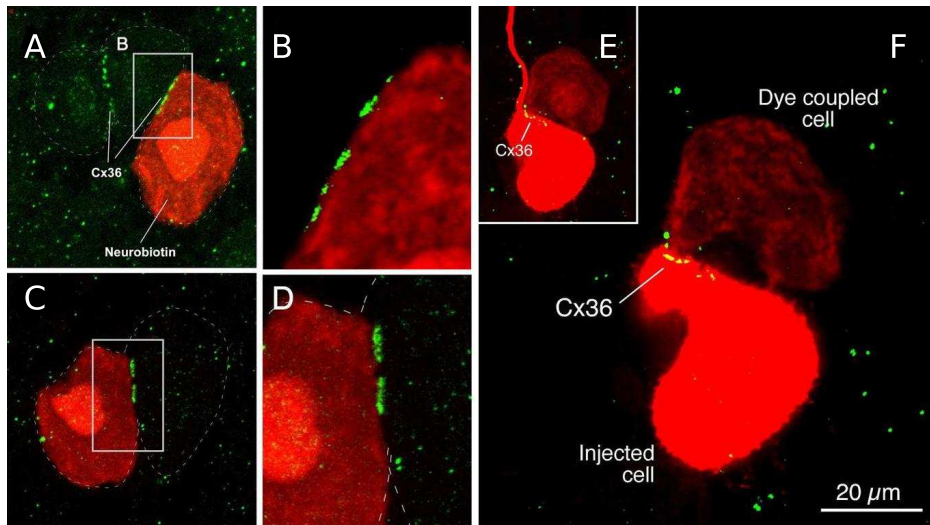
Figure 4.9: Mes V neurons are coupled by gap junctions, made by connexin36 (Cx36). However, Cx36 presence (green) does not guarantee electrical coupling as it is shown by neurobiotin (an intracellular label) injection in (A,B,C,D). In the case of (E,F), connexins are open, allowing neurobiotin to spread between them. Image adapted from [33].

4.7 Summary

A complete Mes V neuron model has been defined in this chapter. This model takes into account the sodium and hyperpolarization-activated currents characterised in chapter 3, as well as other ionic currents from bibliography, reviewed in the first part of this chapter. Its geometrical and passive parameters were estimated using cable theory, while evolutionary algorithms were employed to get the others: maximum ionic conductances and Kv3 current's time constant. This model reproduces most of the features generated by experimental neurons and presents far better current clamp responses than previously reported.

The synaptic inputs of Mes V neurons have been briefly reviewed. The aim of the next two chapters will be to study how the electrical coupling between pairs of Mes V neurons interact with their membrane properties and peripheral inputs.

Chapter 5

The cellular membrane as a filter

5.1   Introduction

Experimental models have shown that individual Mes V neurons present high-frequency (from 49 to 90 Hz [185]) voltage oscillations at the subthreshold level [138, 186]. These small-amplitude oscillations are not due to oscillatory input, but the consequence of the Mes V neuron selective response to inputs within a frequency range.

Assuming linear behaviour near resting membrane potential, the *impedance* of these neurons have been measured by injecting signals with rich frequency content and computing the Fourier transform of the response. This impedance is similar to a band-pass filter, whose properties depend on ionic currents and membrane potential. In this chapter, an analytical expression of this impedance function will be derived from a reduced version of the Mes V neuron model.

On the other hand, there is recent evidence that there could be frequency preference in the subthreshold communication between neurons coupled by electrical synapses [33], instead of mere low-pass filter properties (some recent articles: [14, 31, 59, 106, 175, 179]. This property can be characterised using a *transfer function*, whose frequency preference will be studied from the mathematical point of view, following the same procedure used to compute the impedance function.

5.2   Small-signal model of Mes V neuron

In order to study analytically Mes V neuron's behaviour at subthreshold level and understand the role of each voltage-gated current, it is necessary to simplify the whole model of Mes V neuron. Experimental recordings have shown that subthreshold properties of Mes V neurons are shaped by the persistent sodium current I_{NaP} [41, 185, 186] and 4-AP-sensitive potassium I_{4AP} [80, 185]. Therefore, these two currents have to be included in the reduced model.

On the other hand, the model has not to take into account currents whose steady activation curves are roughly zero at resting potential. Hence, transient sodium I_{NaT}, high-threshold potassium current I_{Kv3}, potassium delayed rectifier I_{DRK} and hyperpolarization-activated current I_h are not taken under consideration. The resulting reduced model of an individual Mes V neuron can be expressed as:

$$\begin{cases} C\dfrac{dV}{dt} = & I_{inj} - I_L - I_{NaP} - I_{4AP} = a\left(V, n_{4AP}, I_{inj}\right) \\[2mm] \dfrac{dn_{4AP}}{dt} = & \dfrac{n_{4AP\infty}(V) - n_{4AP}}{\tau_{4AP}} = b\left(V, n_{4AP}\right) \end{cases} \tag{5.1}$$

where V stands for the membrane potential, C the neuron's capacitance (remember that this is a single-compartment model), I_{inj} the injected current and I_L the leak current.

The objective is to analyze how is the neuron's response to pulse current stimuli that do not elicit action potentials, but just small-amplitude voltage oscillations. In order to do that, the equations (5.1) will be linearized around the equilibrium.

Let V_0 and n_{4AP0} be the stationary values of the state variables: $a\left(V_0, n_{4AP0}, I_0\right) = b\left(V_0, n_{4AP0}, I_0\right) = 0$, and define small-signal variables:

$$\begin{cases} i_{inj} &= I_{inj} - I_{inj0} \\ v &= V - V_0 \\ \eta_{4AP} &= n_{4AP} - n_{4AP0} \end{cases}$$

Assuming small-amplitude voltage fluctuations and that the resting potential is a stable equilibrium point of the system, the differential equations (5.1) can be linearized, taking the partial derivatives of functions a and b:

$$\begin{cases} C\dfrac{dv}{dt} = & -\left[g_L + \overline{g}_{4AP}n_{4AP\infty} + \overline{g}_{NaP}n_{NaP\infty} + \overline{g}_{NaP}\dfrac{dn_{NaP\infty}}{dV}\left(V - E_{Na}\right)\right]v - \\ & -\overline{g}_{4AP}\left(V - E_K\right)\eta_{4AP} + i_{inj} \\[3mm] \dfrac{d\eta_{4AP}}{dt} = & \dfrac{1}{\tau_{4AP}}\dfrac{dn_{4AP\infty}}{dV}v - \dfrac{1}{\tau_{4AP}}\eta_{4AP} \end{cases}$$

$$\tag{5.2}$$

Now, it is possible to study how the neuron responds to sinusoidal stimuli, by applying the Fourier transform to the linearized system (5.2). This response is characterised by the neuron impedance $Z(j\omega)$, defined as the ratio between the Fourier transforms of voltage v and the injected current i_{inj}, for each angular frequency ω. After some calculations, the Mes V neuron impedance is expressed as:

$$Z(j\omega) = \left[j\omega C + g_L + \overline{g}_{4AP} n_{4AP\infty} + \overline{g}_{NaP} n_{NaP\infty} + \overline{g}_{NaP} (V_0 - E_{Na}) \frac{dn_{NaP\infty}}{dV} + \right.$$
$$\left. + \overline{g}_{4AP} \frac{(V_0 - E_K)}{1 + j\omega\tau_{4AP}} \frac{dn_{4AP\infty}}{dV} \right]^{-1}$$
$$(5.3)$$

Although the expression 5.3 is quite complicated, it is possible to see that it has one zero and two poles. The zero only depends on the I_{4AP} time constant, while the poles are dependent on all the properties, including the characteristics of the sigmoid-like steady-state activation curves $n_{NaP\infty}$, $n_{4AP\infty}$ and its derivatives. Some of this features will be shared by the next challenge: the transfer function between Mes V neurons.

5.3 Transfer function between coupled neurons

In the case of two coupled neurons, it is interesting in how information pass between them at subthreshold level. To model that, one neuron (neuron 1) will be stimulated by an external current signal I_{inj}, that corresponds to a step in the case of the experimental recordings, but can be any other signal. The postsynaptic neuron will be neuron 2. Using the reduced model presented in the section 5.2 and adding the electrical coupling between the neurons (see Figure 5.1), the differential equations describing the system can be expressed as:

$$\begin{cases} \dfrac{dV_1}{dt} &= \dfrac{1}{C_1} [I_{inj} - g_{L1}(V_1 - E_L) - g_{NaP1}.n_{NaP1\infty}(V_1 - E_{Na}) - \\ & \quad g_{4AP1}.n_{4AP1}(V_1 - E_K) - g_j(V_1 - V_2)] \\[2ex] \dfrac{dn_{4AP1}}{dt} &= \dfrac{1}{\tau_{4AP}} [n_{4AP1\infty} - n_{4AP1}] \\ \dfrac{dV_2}{dt} &= \dfrac{1}{C_2} [-g_{L2}(V_2 - E_L) - g_{NaP2}.n_{NaP2\infty}(V_2 - E_{Na}) - \\ & \quad g_{4AP2}.n_{4AP}(V_2 - E_K) - g_j(V_2 - V_1)] \\[2ex] \dfrac{dn_{4AP2}}{dt} &= \dfrac{1}{\tau_{4AP}} [n_{4AP2\infty} - n_{4AP2}] \end{cases} \quad (5.4)$$

Now, the transfer function $H(j\omega) = \frac{V_2(j\omega)}{V_1(j\omega)}$ can be obtained by applying the same procedure used before to calculate the impedance of a neuron, $Z(j\omega)$. After linearizing and applying the Fourier transform to the four differential equations in (5.4), the resulting system has four equations and five variables: $V_1(j\omega)$, $V_2(j\omega)$, $\eta_{4AP1}(j\omega)$, $\eta_{4AP2}(j\omega)$ and $i_{inj}(j\omega)$. However, only the last two equations are needed to compute the transfer function:

$$H(j\omega) = \frac{g_j (1 + j\omega\tau_{4AP})}{(j\omega)^2 \tau_{4-AP} C_2 + (C_2 + \Gamma_\infty \tau_{4AP}) j\omega + \Gamma_0} \quad (5.5)$$
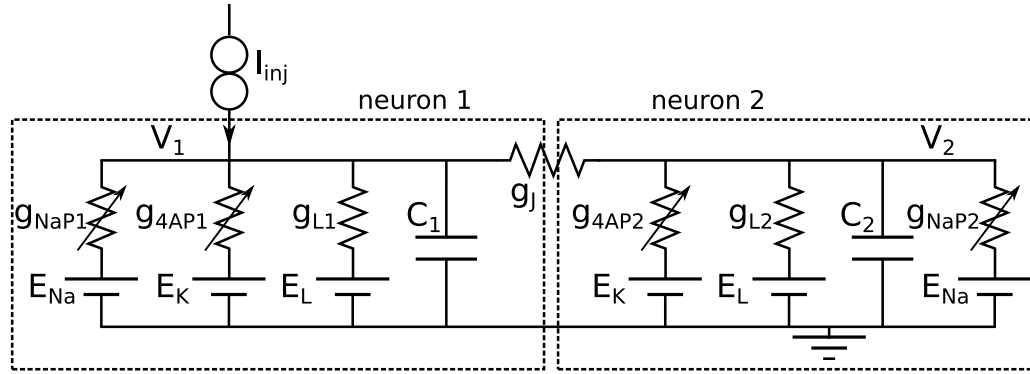
Figure 5.1: Reduced model of two coupled neurons, according to equations 5.4.

where:

$$\Gamma_0 = g_{L2} + g_j + \overline{g}_{4AP2}\left[n_{4AP2\infty} + \frac{dn_{4AP2\infty}}{dV_2}(V_2 - E_K)\right] + \overline{g}_{NaP2}\left[n_{NaP2\infty} + \frac{dn_{NaP2\infty}}{dV_2}(V_2 - E_{Na})\right]$$
(5.6)

and

$$\Gamma_\infty = g_{L2} + g_j + \overline{g}_{4AP2}n_{4AP2\infty} + \overline{g}_{NaP2}\left[\frac{dn_{NaP2\infty}}{dV_2}(V_2 - E_{Na}) + n_{NaP2\infty}\right]$$ (5.7)

Again, the expression (5.5) is pretty complicated to fully understand it at a glance. However, there are a couple of key features to highlight. First, the transfer function $H(j\omega)$ depends only on the properties of the postsynaptic neuron and the coupling strength. Not a single parameter from the presynaptic neuron appears on its analytical expression. The second feature is related with the first one: Equation (5.5) is almost the same as the expression for the neuron impedance $Z(j\omega)$ (5.3). Actually, the two differential equations (5.1) are almost the same as the last two from (5.4), with $i_{inj} = g_j(V_1 - E_L)$ and $g_{L2} = g_L + g_j$. Then, the transfer function between two neurons can be interpreted as the impedance function of a neuron, with an injected current proportional to the presynaptic membrane potential and a leak conductance composed by its own leak and the gap junction conductance.

Apart from these two important results, it is difficult to get more insight from (5.5). In the next section, the transfer function will be studied by low and high frequency approximations, that are more intuitive to understand.

5.4 Frequency preference of coupled neurons

The impedance $Z(j\omega)$ of a neuron accounts for its behaviour when the injected current produce subthreshold voltage changes. It can be interpreted as a function that determines the excitability of neurons depending on the frequency content of the stimulus. If the neuron impedance has a peak in a given frequency, the cell is more suitable to reach its threshold and fire. A similar thing can be said of

the transfer function between two neurons $H(j\omega)$, that also are shown to present resonance [33]. $H(j\omega)$ measures how the postsynaptic neuron responds to voltage changes in the presynaptic one. If the presynaptic is oscillating at some frequency $\omega = \omega_0$, the postsynaptic will be oscillating at the same frequency too, but with a relative amplitude and phase given by the value of $H(j\omega_0)$.

Instead of working with the full expression (5.5), it is possible to dissect it analyzing its asymptotic behaviours: for low and high frequencies. The transfer function resonance will be explained as the result of the overlaping between a low-pass filter (cutoff frequency f_{LP}) and a high-pass filter (cutoff frequency f_{HP}), when $f_{HP} < f_{LP}$ [84].

Let's come back to the last two equations of the Mes V coupled neurons reduced model (5.4). For the sake of simplicity, the subscripts 1 and 2 will still be utilized only for distinguishing between pre and postsynaptic voltages, given that all the parameters and the state variable n_{4AP} corresponds to the postsynaptic neuron 2:

$$\begin{cases} \dfrac{dV_2}{dt} & = & -\dfrac{1}{C}\left[g_L(V_2 - E_L) + \overline{g}_{NaP}.n_{NaP\infty}(V_2 - E_{Na}) \right. \\ & & \left. + \overline{g}_{4AP}.n_{4AP}(V_2 - E_K) - g_j(V_2 - V_1)\right] \\ \\ \dfrac{dn_{4AP}}{dt} & = & \dfrac{1}{\tau_{4AP}}\left(n_{4AP\infty} - n_{4AP}\right) \end{cases} \tag{5.8}$$

Now, note that the differential equations (5.8) have two different time scales: τ_m for the voltage variable V_2 and τ_{4AP} for n_{4AP}. Actually, $\tau_m < \tau_{4AP}$ as sub-threshold depolarizing current steps show: after a $+50$ pA current step there is always an overshoot due to the slower n_{4AP} kinetics (see section 4.4.2). This time constant mismatch will be utilized in the next sections to study asymptotic behaviours.

5.4.1 Low-pass behaviour

For fast frequency stimuli, n_{4AP} cannot "see" voltage changes. Therefore, for all purposes, it could be considered in steady state: $n_{4AP} = n_{4AP\infty}(V_{2initial})$ and $\frac{dn_{4AP}}{dt} = 0$. Applying that on the differential equations 5.8, linearizing and making Fourier analysis as in the previous section, the transfer function for high frequencies $H_{\mathrm{LP}}(j\omega)$ is:

$$H_{\mathrm{LP}}(j\omega) = \frac{V_2(j\omega)}{V_1(j\omega)} = \frac{g_j}{\Gamma_0}\frac{1}{1 + \dfrac{j\omega}{\omega_m}} \tag{5.9}$$

The transfer function $H_{\mathrm{LP}}(j\omega)$ is a low pass filter, whose bandwidth $\omega_m = \frac{\Gamma_0}{C}$ is directly proportional to Γ_0, that was defined in equation (5.6).

Notice that the bandwidth of the transfer function is not only determined by the passive properties (such as its capacitance, leak and gap conductance): its ionic currents contribute to it too.

5.4.2   High-pass behaviour

On the other hand, for low-frequency signals, below low-pass cutoff frequency, the capacitor has enough time to become fully charged and $i_C = C\frac{dV_2}{dt} = 0$. The low-pass filter is not filtering too much in this frequency range. However, n_{4AP} can follow low frequency signals ($\frac{dn_{4AP}}{dt} \neq 0$) and filter them. According to that, the transfer function for low frequencies $H_{\mathrm{HP}}(j\omega)$ can be approximated as:

$$H_{\mathrm{HP}}(j\omega) = \frac{V_2(j\omega)}{V_1(j\omega)} = \frac{g_j\left(1 + j\omega\tau_{4AP}\right)}{\Gamma_0 + j\omega\tau_{4AP}\Gamma_\infty} = \frac{g_j}{\Gamma_\infty} \frac{j\omega + \dfrac{1}{\tau_{4AP}}}{j\omega + \dfrac{1}{\tau_{4AP}}\dfrac{\Gamma_0}{\Gamma_\infty}} \tag{5.10}$$

where Γ_∞ was defined in Equation (5.7).

5.4.3   Conditions to get resonance

In conclusion, the transfer function $H(j\omega)$ can be approximated for a low-pass filter for high frequencies and a sort of high-pass filter for low frequencies. The Figure 5.2 displays the absolute value of the magnitude of both filters and the resulting transfer function. Basically, there is resonance in the region where the low-pass and the high-pass filters overlap. Hence, a necessary condition to get a resonance peak is $\omega_m = \frac{\Gamma_0}{C} > \omega_1 = \frac{1}{\tau_{4AP}}$.
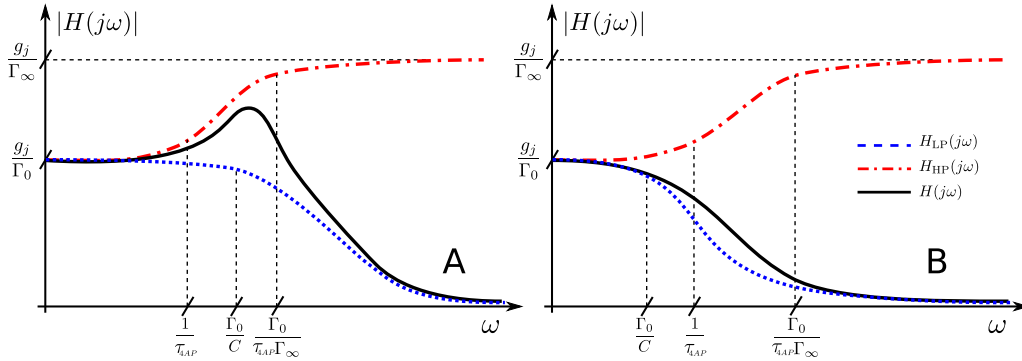

Figure 5.2: Schematic representation of how transfer function's resonance arises from the match between a low-pass (green dots) and a high-pass filter (dash and dots in red). A) The cutoff frequency of the low-pass filter is above the zero of the high-pass filter, producing a hump. B) No resonance can be seen when the low-pass filter begins to filter before the zero of the high-pass filter.

Given that ω_1 is fixed (depends on the intrisic characteristics of the 4-AP-sensitive current), the resonance can be set by increasing ω_m, by enlarging Γ_0, decreasing C or both at the same time. However, increasing Γ_0 may augment Γ_∞ too, because both share several parameters, leading to a net drop of the relative

distance between both parameters and reducing the range of $H_{HP}(j\omega)$. Actually, the high-pass filter only exists when there is a difference between there is the zero and the pole of the high-pass filter. Therefore, resonance will be abolished if $\Gamma_0 - \Gamma_\infty = \overline{g}_{4AP} \frac{dn_{4AP\infty}}{dV_2} (V_2 - E_K) = 0$. That may happen in two cases:

1. $\overline{g}_{4AP} = 0$: there is no 4-AP-sensitive potassium on the postsynaptic cell. One way to check this experimentally may be by blocking 4-AP-sensitive current with 4-AP or producing knockout rats not expressing 4-AP-sensitive current channels.

2. $\frac{dn_{4AP\infty}}{dV_2} = 0$: resting potential is not in the linear region of the 4AP-sensitive current activation variable. This is extremely interesting, because it means that the resonance only operates in a voltage-range around the half activation voltage of 4-AP-sensitive current $V_{4AP1/2}$. Roughly, the resting potential $V_2 \in \left[V_{4AP1/2} - k_{4AP}, V_{4AP1/2} + k_{4AP}\right]$. That is consistent with the following two observations:

    - Below $V_{2min} = V_{4AP1/2} - k_{4AP}$ The 4-AP-sensitive current does not operate, as in the first case

    - Above $V_{2max} = V_{4AP1/2} + k_{4AP}$ The 4-AP-sensitive current is saturated (all the channels are open), acting as a leak.

Figure 5.3 summarizes all the conditions to get a resonant peak. Notice that the resonant behaviour only operates above the resting potential ($V_2 \simeq$-56 mV), for depolarizing presynaptic inputs. On the other hand, it decreases quickly above the firing threshold ($V_2 \simeq$-45 mV), when the linear model and its transfer function are no longer valid. In the next section, this model for the transfer function will be checked against experimental data.
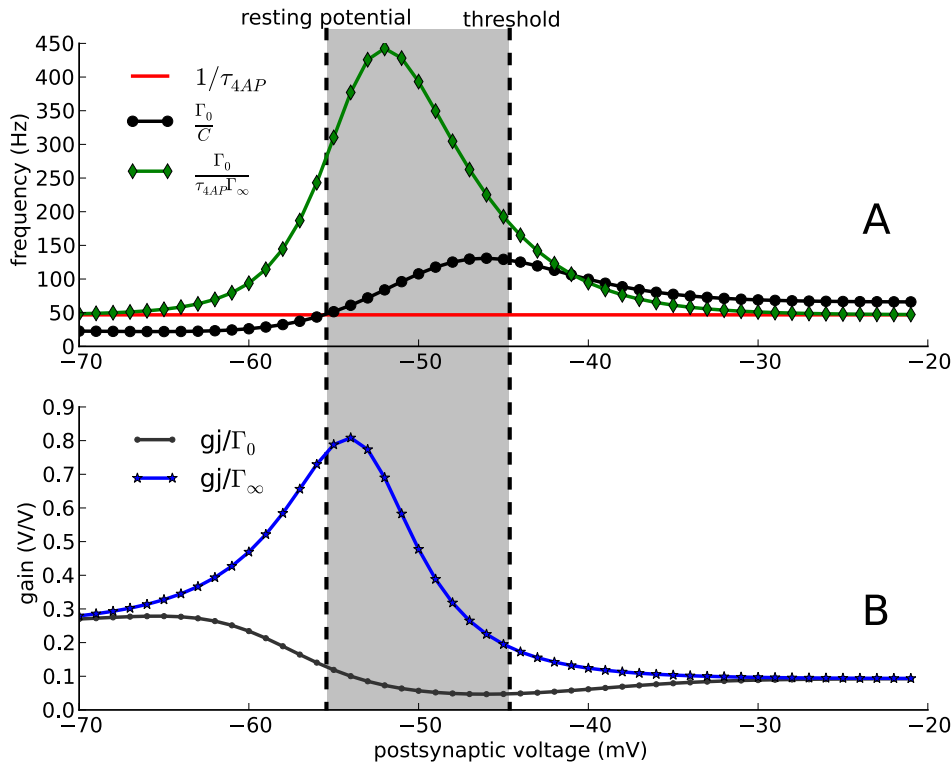
Figure 5.3: The shaded region indicates the voltage region where there is a resonant peak: the cutoff frequency of the low-pass filter, Γ_0/C may be larger than the lower frequency of the high-pass, $1/\tau_{4AP}$ (A); the high-pass filter gain may be larger at high frequencies (B); the linear model has to be valid (below threshold, dashed vertical line)

5.5   Tuning the resonance

Experimental recordings were performed at the School of Medicine, by applying current stimuli to the presynaptic neuron and recording the voltage of both pre and postsynaptic neurons, according to procedures described elsewhere [33]. There were two types of current stimuli:

1. Sinusoids of a given frequency: from 1 to 600 Hz

2. Impedance profile amplitude (ZAP) stimuli [144]: $I(t) = A.sin(at^3)$, where $a = 8\times10^{-7}\ s^{-3}$ and A is the amplitude, adjusted for each neuron for getting small-amplitude voltage deflections. The parameter a was chosen in order to have a frequency content between 1 to 600 Hz.

In fact, ZAP currents are the most widely signal used to measure frequency reponse in neurons [19, 62, 64, 82–84], given that resonance can be detected online by the researcher eye, just looking at the voltage response envelope. Each couple of traces also allows to obtain the complete transfer function estimate, as the ratio between the fast Fourier transform (FFT) of post and presynaptic voltage traces. Sinusoids may be simpler to analyze, but require a large amount of frequencies

(and time) to get a good transfer function.

Linearization only works well when the fluctuations of the system around the equilibrium are very small. However, electrophysiological noise defines a minimum postsynaptic voltage excursion of around 5 mV, given that below that signal-to-noise ratio worsens. Due to transfer function attenuation, the presynaptic excursion may be 5 times larger than the presynaptic one. Then, the presynaptic neuron is always out of the linear range and it is not possible to get its impedance, for example. Finally, the researcher is not directly controlling pre or postsynaptic membrane potentials, but the injected current. For this reason, the "ideal" of 5 mV at the postsynaptic neuron is very difficult to get in the lab, with the consequent increased mismatch between linear and experimental models. Given that constant amplitude sinusoidal and ZAP currents were injected, their responses are very poor at frequencies above 100 Hz, also due to frequency-dependent attenuation.

To unmask the impact of ionic currents in the transfer function, they were selectively blocked by drugs. First, coupled neurons' response was recorded in control conditions, without any drug. Then, I_{NaP} was blocked by TTX and the frequency response was measured again. Finally, I_{4AP} was blocked by 4-AP, in order to record the transfer function without these two currents.

An inverted version of the recording procedure simplifies transfer function modelling, according to the expression (5.5). Indeed, the experimental response in presence of both 4-AP and TTX means $\overline{g}_{4AP} = \overline{g}_{NaP} = 0$, that means a transfer function $H_{\text{TTX + 4AP}}(j\omega)$:

$$H_{\text{TTX + 4AP}}(j\omega) = \frac{g_j}{g_j + g_L + j\omega C} \tag{5.11}$$

Equation (5.11) is a low-pass filter, with only three parameters to estimate: capacitance C, leak and gap conductances g_L and g_j, whose values are also calculated by the recording software[1]. An example of the response of pre and postsynaptic neurons during a ZAP protocol is shown in Figure 5.4, in presence of 4-AP and TTX. According to the linearized model, each neuron has to show a low-pass response. However, the high amplitude of the presynaptic response (more than 50 mV peak to peak) activates other ionic currents both TTX and 4-AP-resistant. The resulting voltage waveform is asymmetric, probably due to the activation of the delayed potassium rectifier I_{DRK} at depolarized levels. Postsynaptic neuron has a high amplitude too and its waveform is pretty similar to the presynaptic one.

After finding C, g_L and g_j, the same fitting procedure is used to get $\overline{g}_{4AP}$ from recordings in presence of TTX (without I_{NaP}). Finally, $\overline{g}_{NaP}$ is obtained

---

[1]In fact, recording software makes online estimates of several parameters while recording. However, this values are not always accurate, given that they correspond to simplified models, and usually fluctuate in time, because of changes in the experimental conditions.
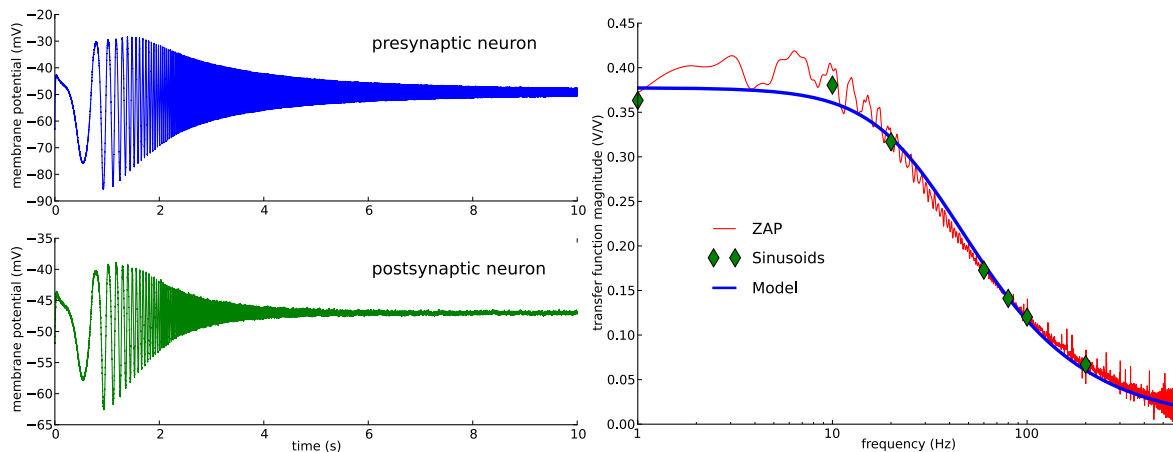
Figure 5.4: Left: pre and postsynaptic voltage traces during a ZAP protocol, in presence of TTX and 4-AP. Right: transfer function estimate obtained as the ratio between the FFT of the post and presynaptic traces, as well as the response to sinusoidal inputs in diamonds and the linearized model fit.

from the control recordings. Figure 5.5 presents the results from the same cell pair shown in 5.4. The presynaptic response is smaller than in the previous case, but is still asymmetrical, due to the larger resonance for voltages above -56 mV, approximately. The amplitude of the postsynaptic response at the resonance peak is within the ideal range, but it decreases rapidly at higher frequencies and almost merges with noise. Nevertheless, the transfer function can be fitted using the linearized model. The resonance peak at 42 Hz can be characterised by the Q-value, defined as the ratio between its magnitude and the DC gain [82]; in this case: Q=1.32. The width at half amplitude of the hump is around 38 Hz, which means a relatively wide frequency preference, while the cutoff frequency is 95 Hz.
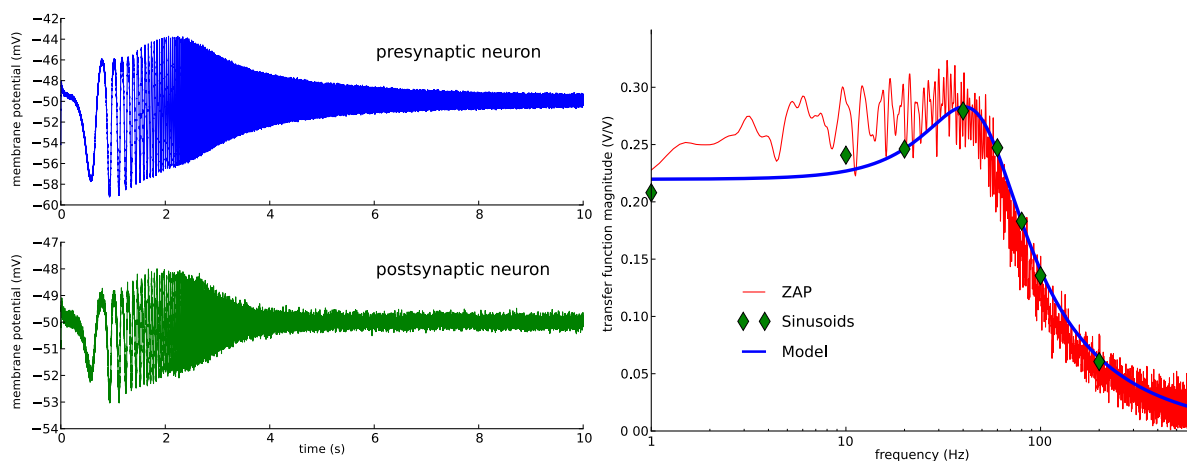

Figure 5.5: Response for a ZAP in control conditions. Pre and postsynaptic voltage traces (A and B). Right: transfer function (C).
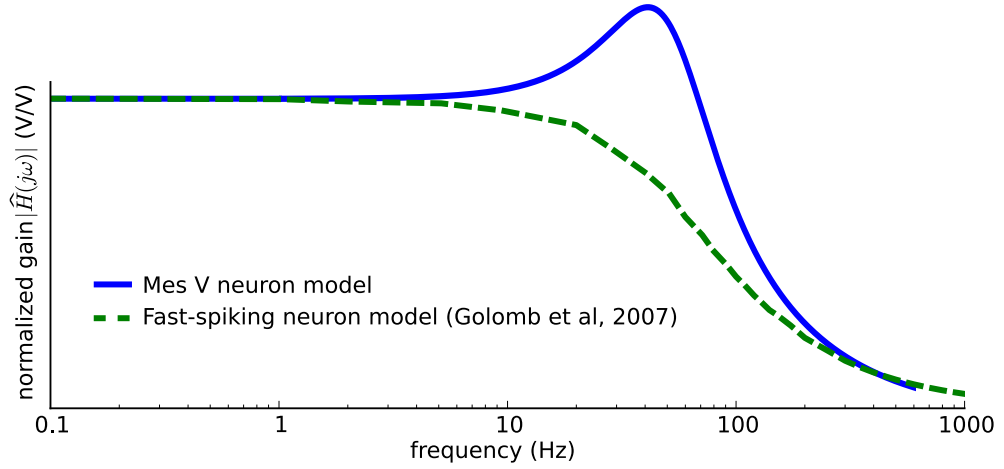
Figure 5.6: Transfer function comparisson between Mes V and fast-spiking neuron models [60]. Fast-spiking transfer function does not only have a smaller cutoff frequency (around 50 Hz), but it is a classic low-pass filter, as it was reported experimentally too [59].

Actually, the transfer function between Mes V neurons is unique among those reported previously in bibliography. Figure 5.6 compares it with the transfer function between fast-spiking (FS) neurons (which are also connected by gap junctions [59]), simulated from a model developed by Golomb et al [60]. Indeed, coupled FS neurons act as low-pass filters, like Mes V neurons without I_{NaP} and I_{4AP} (Equation 5.11). In addition to that, the FS cutoff frequency is almost the half of the Mes V one, meaning that they are not well suited to pass fast signals. This is coherent with the fact that FS are less efficient to transfer spikes than Mes V neurons [33], as it will be studied in the next chapter.

Even though it is not possible to vary smoothly the amount of I_{NaP} and I_{4AP} in the experimental model, the mathematical model can be simulated for different values of $\overline{g}_{NaP}$ and $\overline{g}_{4AP}$. Figure 5.7A shows that persistent sodium is not essential for resonance, but amplifies it, as well as the overall gain. Coming back to the full expression of the transfer function (5.5), it can be seen that I_{NaP}-related terms appear only in the denominator, multiplying the following term:

$$N(V) = n_{NaP2\infty} + \frac{dn_{NaP2\infty}}{dV_2}(V_2 - E_{Na}) \tag{5.12}$$

The product between the steady-state derivative $\frac{dn_{NaP2\infty}}{dV_2} > 0$ and the driving force $(V_2 - E_{Na}) < 0$ makes $N(V) < 0$ for $V_2 < -34$ mV. Therefore, larger persistent sodium conductances $\overline{g}_{NaP}$ lead to smaller Γ_∞ and Γ_0 that decrease the denominator, producing a net increase in the transfer function magnitude. The Q-value grows for the same reason, basically because of a net decrease on the damping term in the denominator: $(C_2 + \Gamma_\infty \tau_{4AP})$. Larger non realistic $\overline{g}_{NaP}$ values make the neuron unstable, given that the real part of the poles becomes positive.

On the other hand, the transfer function between neurons goes from a low-pass filter to a band-pass filter as $\overline{g}_{4AP}$ increases, as Figure 5.7B proves. The resonance peak is very sensitive to $\overline{g}_{4AP}$ as well as the Q-value and the hump's width. Unlike persistent sodium, 4-AP-sensitive current reduces the DC value too, given that its increase leads to a net decrease in the transfer function denominator, given that $(V_2 - E_K)$ and $\frac{dn_{4AP2\infty}}{dV_2}$ are always positive. For this reason, I_{4AP} is both necessary and sufficient to produce a transfer function with one zero and two poles, such as (5.5).
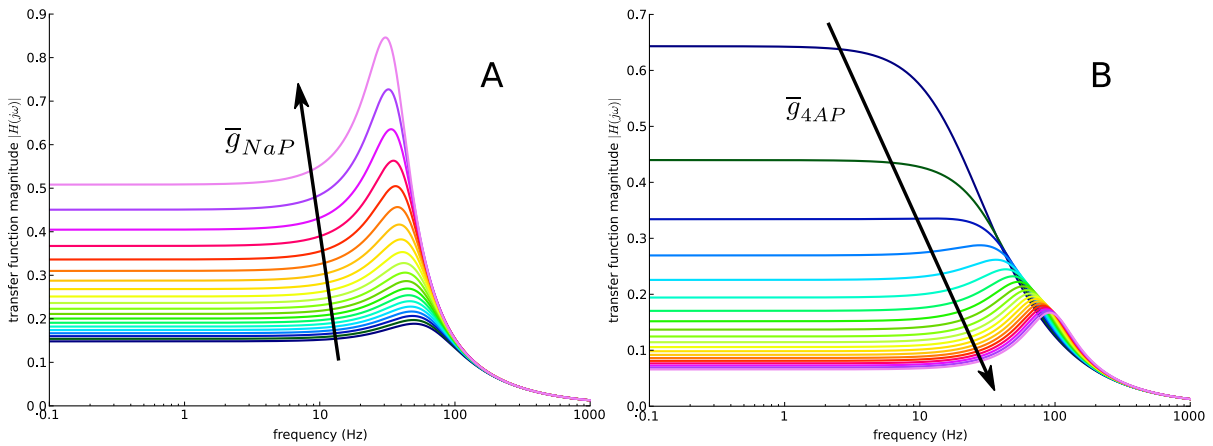
Figure 5.7: Transfer function dependence on $\overline{g}_{NaP}$ (A) and $\overline{g}_{4AP}$ (B). Arrows indicate increasing conductance values, from zero to a biologically pausible value. Persistent sodium conductance $\overline{g}_{NaP}$ increases the excitability of the postsynaptic cell, due to the larger value of the overall transfer function. It also amplifies resonant hump, with minor changes on the peak frequency. However, persistent sodium is not essential to get resonance, given that all the traces present a resonant peak. On the other hand, 4-AP sensitive conductance is key to generate band-pass behaviour, though with a reduced DC value, due to the smaller input resistance R_{IN}.

5.6   Modulation of the transfer function by cGMP

The conclusion from the previous section is that I_{4AP} produces resonance whereas I_{NaP} amplifies it. The next question is what happens if another current is added to the model? Well, in fact, it may produce resonance or amplify it, depending on the same thing: the sign of the product between their corresponding driving forces and the steady-state curve derivatives. Izhikevich used this sign to classify ionic current variables in two categories: *resonating* and *integrating* [88], which are the basis of class 2 and class 1 excitabilities, respectively.

Thus, the hyperpolarization-activated current I_h may produce resonance too, given that it satisfies the sign condition, as Figure 5.8. Indeed, it can induce a resonance in the neuron impedance [170], but only when the resting membrane

potential is at very hyperpolarized values, because of the steady-state activation curve s_∞ of I_h. However, in section 3.2 it was shown that cyclic GMP (cGMP) modulates it, moving its half-value $V_{1/2}$ to more depolarized values and increasing its slope k. The overall effect of cGMP is that I_h becomes involved in the neuron dynamics around resting potential, with a consequent effect on the transfer function.
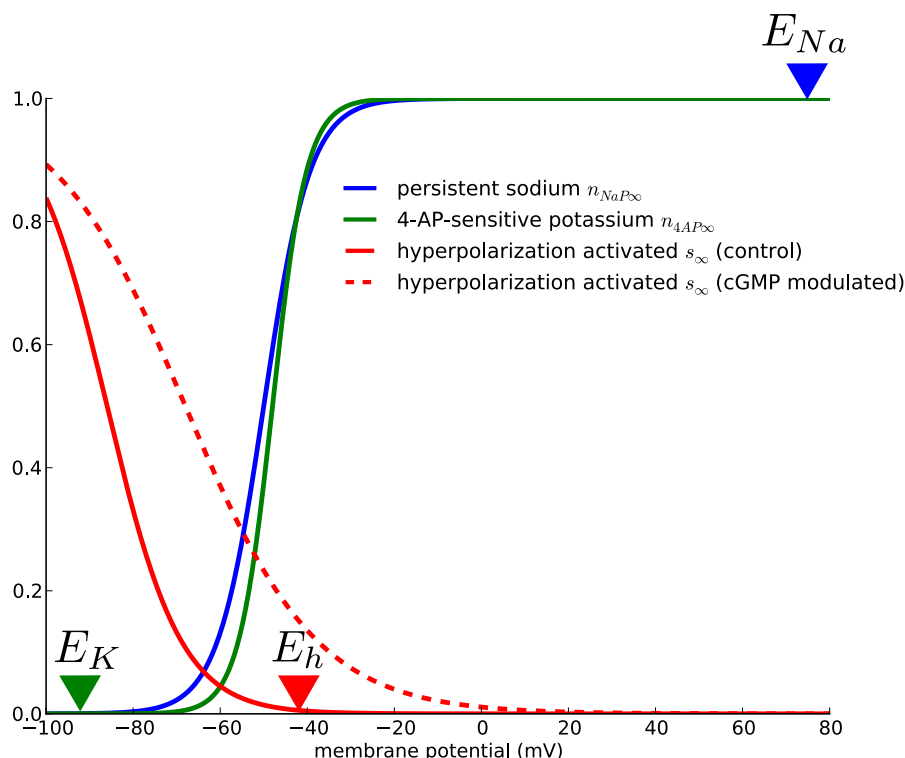

Figure 5.8: Integrating versus resonating currents, according to their steady-state activation curves and their equilibrium potentials. For resonating currents, such as I_{4AP} and I_h, the equilibrium potential lies at the base of the sigmoid. The opposite is valid for I_{NaP}. The intuitive interpretation is that resonance is produced when the growth of the activation variable increases the driving force, that acts as a negative feedback.

Although there are no experimental recordings of this phenomenon yet, numerical simulations (Figure 5.9) confirm the effect of cGMP in the transfer function. First of all, the DC value decreases a lot, again due to the change on the input resistance R_{IN} (not shown). There is an important change on the curve's shape: the band-pass region becomes wider, reducing the specificity of the frequency preference of the coupled neurons, and the bandwith increases too. Then, it is expected that this neurons are more able to transmit information in a larger frequency range in presence of cGMP.
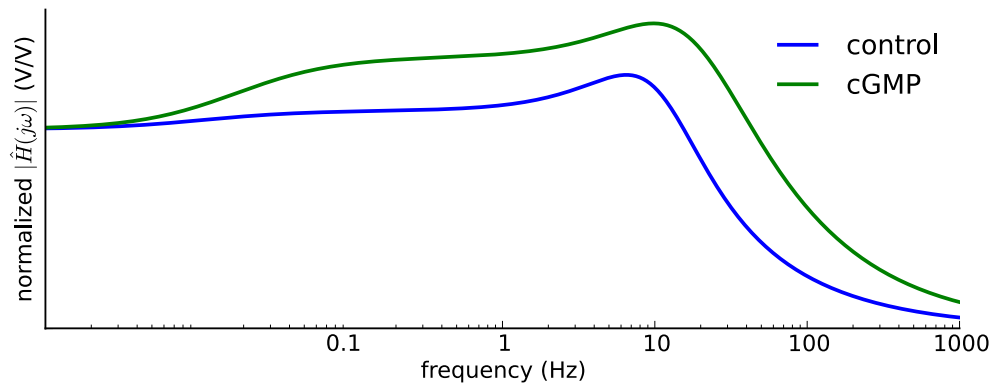
Figure 5.9: Theoretical normalized transfer function modulation including I_h, in control conditions and in presence of cGMP.

5.7   Summary

Along this chapter, the subthreshold transfer function between two neurons was studied using analytical and numerical tools. The results were successfully compared with experimental data. Two major results were demonstrated, challenging previous conceptions [59, 84]:

- Electrically coupled neurons may not act as low-pass filters, but display frequency preference.

- Transfer function properties depend on the coupling strength and also on the *postsynaptic ionic currents*.

Chapter 6

Synchronization of two coupled neurons

6.1 Introduction

This chapter deals with the synchronization of pairs of coupled Mes V neurons, using the multicompartment neuron model presented in chapter 4. The influence of I_{NaP}, I_{4AP} and I_h on synchronization will be studied. The main aim is to demonstrate that synchronization properties are not only dependent on the coupling strength, but also on the intrinsic properties of neurons: its ionic conductances. First, identical neurons will be considered, using phase models to study their phase responses and phase locking. Then, numerical simulations of the model will be used to analyze synchronization lag and recruiting probability. The chapter ends with a more "functional" experiment, to understand how electrical coupling influences sensorial information processing.

6.2 Phase response curve

The phase response curve is a tool that characterizes the behaviour of a periodically spiking neuron under brief perturbations [63]. If the oscillation period of the "standalone" (isolated, unperturbed) neuron is T, the phase variable ϕ can be defined as $\phi = 2\pi t/T$ for each cycle, where $t = 0$ is usually taken at the peak of the action potential.

Now, suppose that the oscillator is stimulated by a sudden pulse at $t = t_s$, as Figure 6.1 shows. The phase of the system may be altered, changing the timing of the next peak. The phase response curve (PRC) $Z(\phi)$ is defined from the new period of the perturbed system T_{new} [18]:

$$Z(\phi) = \Delta\phi = 2\pi\frac{T - T_{new}}{T} \tag{6.1}$$

A negative (positive) $Z(\phi)$ means a phase delay (advance), given that the perturbed system period is larger (shorter) than the original one. Analytical expressions of $Z(\phi)$ can only be obtained for simplified models, such as leaky and

quadratic integrate-and-fire neurons [139]. However, even numerically obtained PRC are very useful to understand neuron's behaviour. In fact, phase shifts of class 1 neurons are always positive, given that they integrate the input, advancing the next spike. On the other hand, class 2 neurons present biphasic PRC: the next spike can be either delayed or advanced depending on the phase of the incoming stimulus [88, 163].
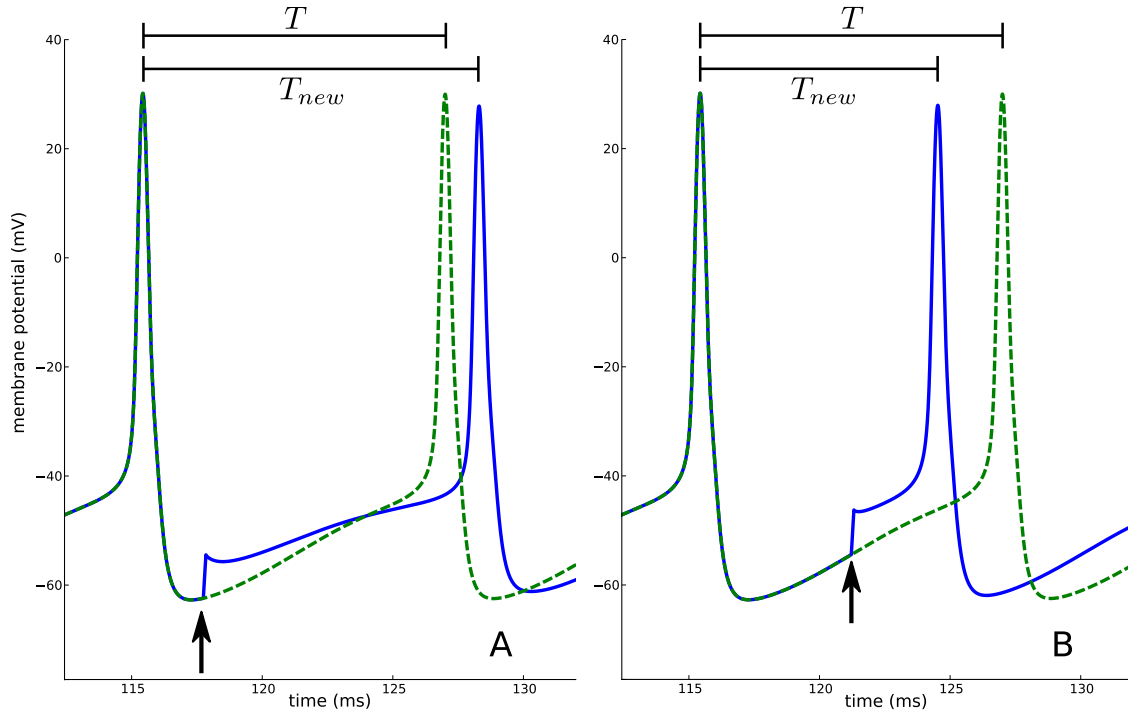

Figure 6.1: Perturbation of an oscillating Mes V neuron model. After an action potential peak, an external pulse is delivered to the neuron (vertical arrow), changing its trajectory from the unperturbed dashed line to the continuous one. Depending on the time (phase) of the stimulus, the next spike can be delayed (A) or advanced (B). In the first case, the PRC is negative, whereas in the other is positive.

Figure 6.2 shows the PRC for Mes V neuron model, varying the maximum conductances of I_{NaP}, I_{4AP} and I_h or modulating I_h by cGMP. Increasing $\overline{g}_{NaP}$ makes dissapear the negative region of the PRC, whereas the contrary happens when $\overline{g}_{4AP}$. This is coherent with the subthreshold properties studied in the chapter 5: I_{NaP} is an integrating current that generates class 1 PRC, whereas I_{4AP} is resonant and produces class 2 behaviour. On the other hand, both parameters have almost no effect after three quarters of the period.

I_h does not change the overall PRC shape, only increasing a bit its phase shift at the middle of the period. Its modulation by cGMP increases slightly the class 2 behaviour, by expanding the negative phase shift region. Again, this is connected with the cGMP-induced resonance, briefly presented at the end of the previous
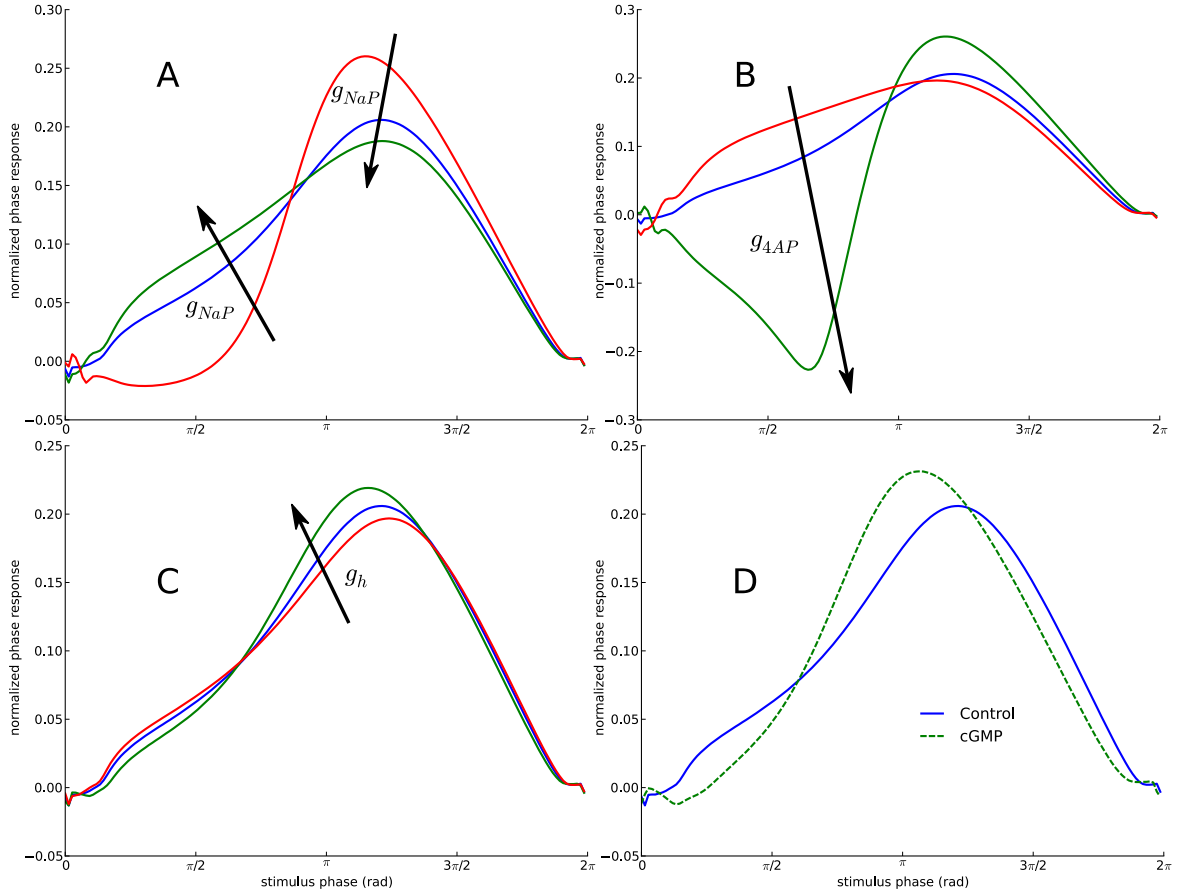
chapter.

Figure 6.2: PRC for Mes V neuron model. The standard model is always shown in blue, whereas red (green) lines denote a decrease (increase) of $\overline{g}_{NaP}$ (A), $\overline{g}_{4AP}$ (B) and $\overline{g}_h$ (C). Figure D shows the effect of cGMP modulation, without changing maximum conductances.

6.3 From PRC to phase locking

In the previous section, it was stated that phase response curves represent neuron's behaviour. According to weakly coupled oscillators theory, the PRC can be used to describe a forced periodic oscillator like:

$$\frac{dX}{dt} = f(X) + \epsilon p(t) \tag{6.2}$$

where X is the state vector (composed by voltages, activation and inactivation variables, etc), f a nonlinear function of the state and $\epsilon p(t)$ an external input that stimulates the system (for example, a synaptic input). The parameter ϵ represents

the stimulus strength and it is assumed to be small. Then, Equation (6.2) can be transformed into a phase model [88]:

$$\frac{d\phi}{dt} = \omega + \epsilon Z(\phi)p(t) \tag{6.3}$$

where $\omega = 2\pi/T$ and T the period of the free-running oscillator (6.2) ($\epsilon = 0$).

Now, suppose that there are two identical coupled oscillators, whose phase models are [52]:

$$\begin{cases} \dfrac{d\phi_1}{dt} = \omega_1 + \Gamma_{12}(\phi_1 - \phi_2) \\ \dfrac{d\phi_2}{dt} = \omega_2 + \Gamma_{21}(\phi_2 - \phi_1) \end{cases} \tag{6.4}$$

where $\omega_1 = \omega_2 = \omega$ and $\Gamma_{12} = \Gamma_{21} = \Gamma$ is the phase coupling function. Assuming that $p(t) = I_{syn}(\phi_1, \phi_2) = -g\left(V(\phi_1) - V(\phi_2)\right)$, Γ can be obtained as [139]:

$$\Gamma(\phi_1 - \phi_2) = \frac{1}{T} \int_0^T Z(u + \phi_1) I_{syn}(u + \phi_1, u + \phi_2) du \tag{6.5}$$

Phase locking can be found by substracting the equations (6.4) and defining $\Delta\phi = \phi_1 - \phi_2$:

$$\frac{d\Delta\phi}{dt} = \Gamma(\Delta\phi) - \Gamma(-\Delta\phi) = \Gamma_{odd}(\Delta\phi) \tag{6.6}$$

Phase locking means constant $\Delta\phi$ and can be found as the zeros of $\Gamma_{odd}(\Delta\phi)$. The fixed points of (6.6) have to satisfy $\dfrac{d\Gamma_{odd}}{d\phi} < 0$. Note that $\Delta\phi = 0$ is a trivial solution, given that $\Gamma(0) = 0$. In fact, it is also stable for these neurons[1].

According to Figure 6.3, the antiphase locking $\Delta\phi = \pi$ is an unstable solution, due to $\dfrac{d\Gamma_{odd}}{d\phi}(\Delta\phi = \pi) > 0$. This derivative decreases with $\overline{g}_{NaP}$, making it less unstable (the contrary happens with $\overline{g}_{4AP}$). That means that, for larger persistent sodium values, the antiphase locking could be a stable solution, as Pfeuty et al have shown for quadratic integrate-and-fire neurons [139].

Finally, now suppose that the coupled neurons are slightly different, due to their maximum conductances, input resistance, time constant or a combination of all. In that case, their free-running frequencies become different too $\omega_1 \neq \omega_2$, provoking a frequency mismatch $\Delta\omega = \omega_1 - \omega_2$. Nevertheless, phase locking is still possible at the zeros of $\hat{\Gamma}_{odd}(\Delta\phi) = \Gamma_{21}(-\Delta\phi) - \Gamma_{12}(\Delta\phi) = -\Delta\omega$ [89]. Then, the mininum and maximum values of $\hat{\Gamma}_{odd}$ determine the maximum and mininum frequency mismatch tolerance for the coupled system.

Hence, $\overline{g}_{4AP}$ and $\overline{g}_{NaP}$ have opposite effects on frequency mismatch tolerance, that is increased by the first current and diminishes with the second (Figure 6.3).

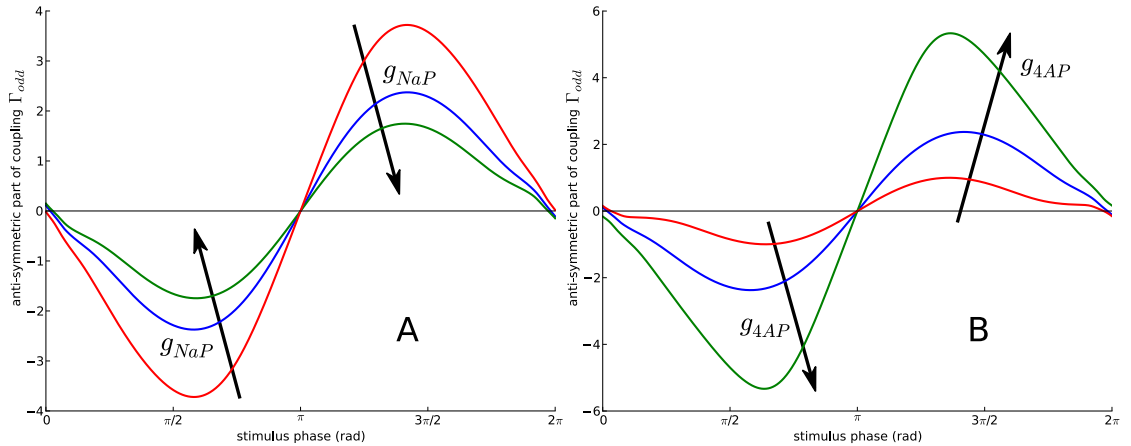[1]Note that there is a small phase shift artifact in the figures, at $\phi = 0$ and 2π.

Figure 6.3: Phase locking for coupled Mes V neurons. Antiphase $\Delta\phi = \pi$ is a unstable solution in both cases, though $\overline{g}_{NaP}$ and $\overline{g}_{4AP}$ have opposite effects on it.

6.4 Non identical neurons

Mes V neurons are quite diverse, due to their different size (i.e.: capacitance), input resistance, ionic current densities, etc. However, they all receive sensorial information coming from masticatory muscle spindles and periodontal ligament receptors, process it in and send the output to motorneurons and other cells. Then, electrical coupling may be a tool to help them to generate coordinated outputs, even if coupled neurons are different. How tolerant is synchronization to differences in the coupled cells?

The base experiment in this chapter consists in two coupled Mes V neuron models, that receive a current step at their somata, whose amplitude allows each neuron to fire only one spike. Both neurons will be identical but in only one parameter: $\overline{g}_{4AP}$ or $\overline{g}_{NaP}$. This parameter will be fixed in one of the neurons (neuron 1) and varied in the other (neuron 2). Two main important synchronization features will be studied: the time lag between synchronized neurons and the probability that one neuron may recruit its coupled partner.

Figures 6.4A-B show how different coupled neurons can get 1:1 synchronization, in a parameter space region that recalls Arnold's tongues [119][2]. In fact, the vertical axis is the coupling strength, g_j, whereas the horizontal one represents the frequency mismatch between neuron 1 and 2, due to their different $\overline{g}_{4AP}$ or $\overline{g}_{NaP}$. As a result, synchronization tolerance to conductances mismatch improves

---

[2]Arnold's tongues are stereotyped parameter space (coupling strength and frequency mismatch) regions where there is 1:1 synchronization. The Mes V neuron model shows standard Arnold's tongues when both neurons present repetitive firing without any coupling. Although this is interesting from the computational point of view, this has no sense in the biological area, given that it is unrealistic to have two uncoupled neurons in "1:1 synchronized state".

with the gap junction conductance. Colorbars indicate the time lag between 1:1 synchronized spike trains in milliseconds. The blue area only indicates not 1:1 synchronization, though it could be other synchronization modes (1:2, 1:3, 2:7, etc).

A zoom of Figures 6.4A and B, at $g_j = 3$ nS (approximately the mean experimental value [33]), is shown in Figures 6.4C and D, respectively. Again, both ionic currents have opposite effects: increasing of $\overline{g}_{NaP}$ ($\overline{g}_{4AP}$) in the neuron 2 leads to a larger (smaller) time delay.
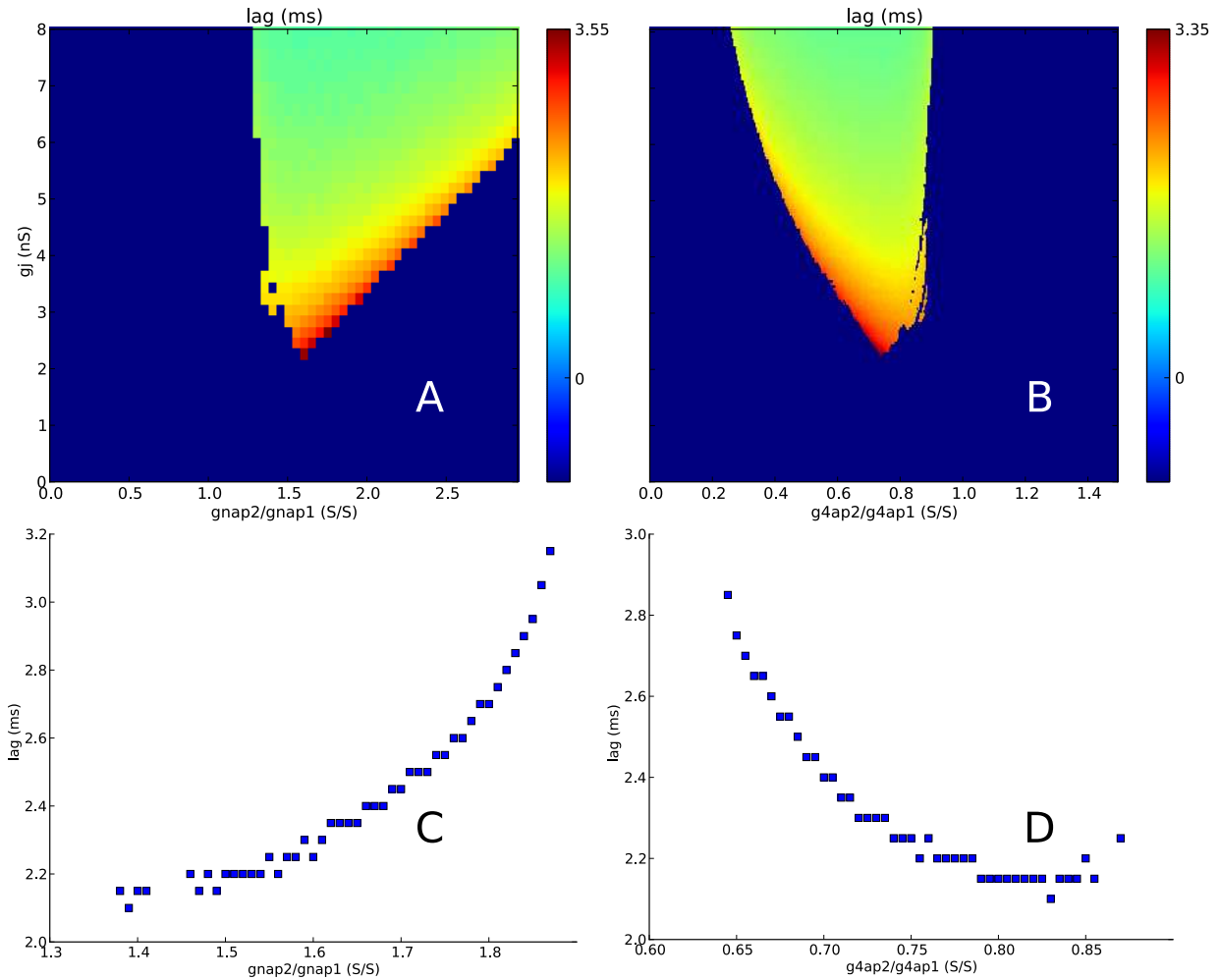
Figure 6.4: Time lag between synchronized spike trains. Increase of postsynaptic $\overline{g}_{NaP}$ produces larger time lags (A), whereas the opposite is valid for $\overline{g}_{4AP}$ (B). A detailed zoom of both figures, at $g_j = 3$ nS, is shown in (C) and (D).

The next objective is to study which conditions improve recruitment of a coupled cell by another repetitively spiking. A small amount of gaussian noise was added to the current steps injected in both neurons, in order to generate some randomness in their behaviours. Recruitment is measured as the ratio between

the post and presynaptic spikes: 100 % means that no presynaptic spike is lost to the post.

Both simulated curves 6.5A1-B1 present the same trend: increasing conductance improves recruitment. Whereas the curve for $\overline{g}_{NaP}$ is sigmoid-like, the corresponding to $\overline{g}_{4AP}$ is almost a step. Two insets in (A1) display a portion of the voltage traces (total simulated time was 10 s) at both extremes of the curve (marked by red points). The remaining two figures present the spikes per second average for each simulation. Notice that neurons get synchronized when their mean frequencies reach the voltage range below 80 Hz, within the subthreshold bandpass frequency band, in agreement with the results presented in section **??**.
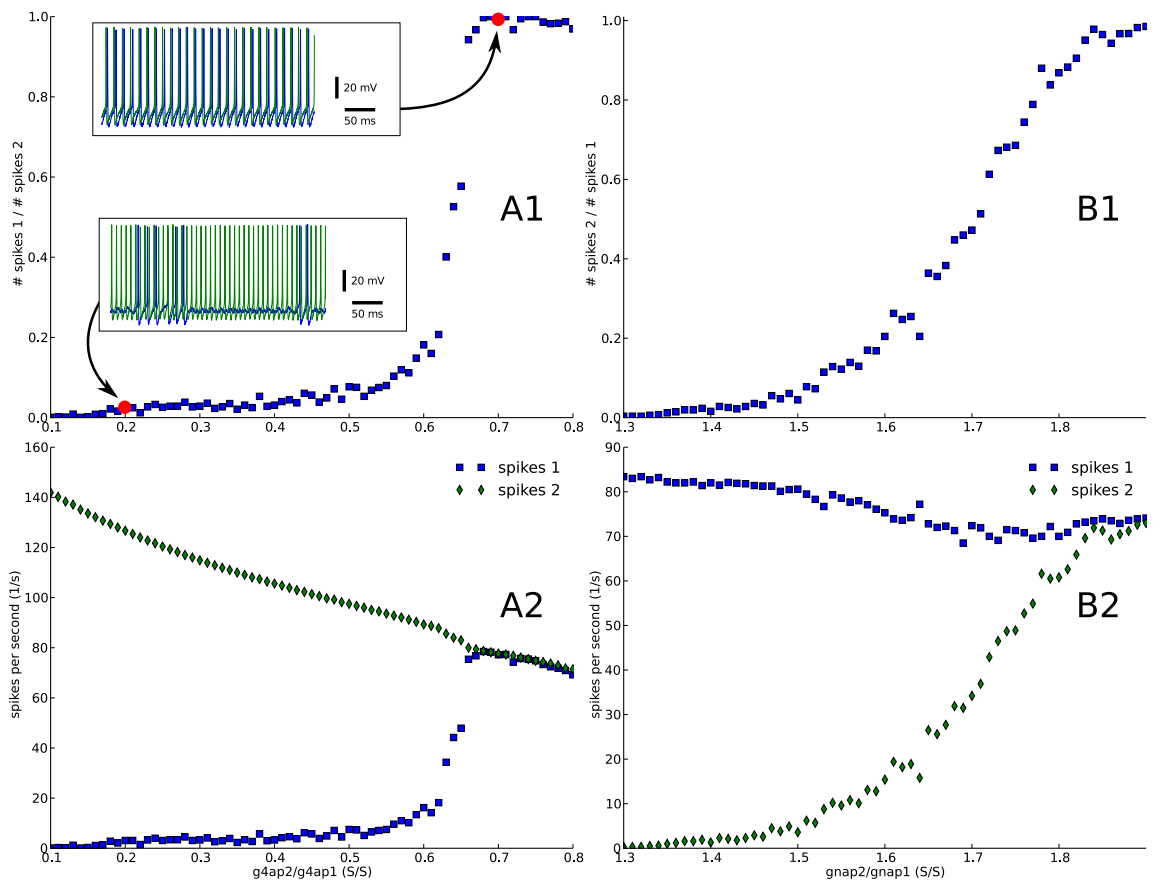

Figure 6.5: Recruitment and frequency content. More I_{4AP} and I_{NaP} promotes recruitment of a neuron by a periodically spiking coupled one (A1,B1). Insets in (A1) display voltage traces at the base and top of the recruitment curves. Actually, recruitment is related with a match between firing frequency and subthreshold properties (A2,B2).

Finally, Mes V neurons are said to be very efficient to transmit action potentials [33], according to coupling measurements. DC coupling is defined as the ratio between post and presynaptic voltage amplitude responses to an hyperpolarizing current step. On the other hand, action potential (AP) coupling is measured as the

quotient between spikelet and spike amplitudes. Figure 6.6 shows how increased postsynaptic I_{4AP} (A) and I_h (C) improves AP coupling efficiency, whereas I_{NaP} (B) has almost no effects on it. The results from the Mes V neuron model in control conditions are compared in (D) with the experimental results (shaded region, adapted from [33]), as well as the fast spiking neuron model [60] used in chapter 5 and experimental results from this neuron. There is a quite good agreement between model and experiments.
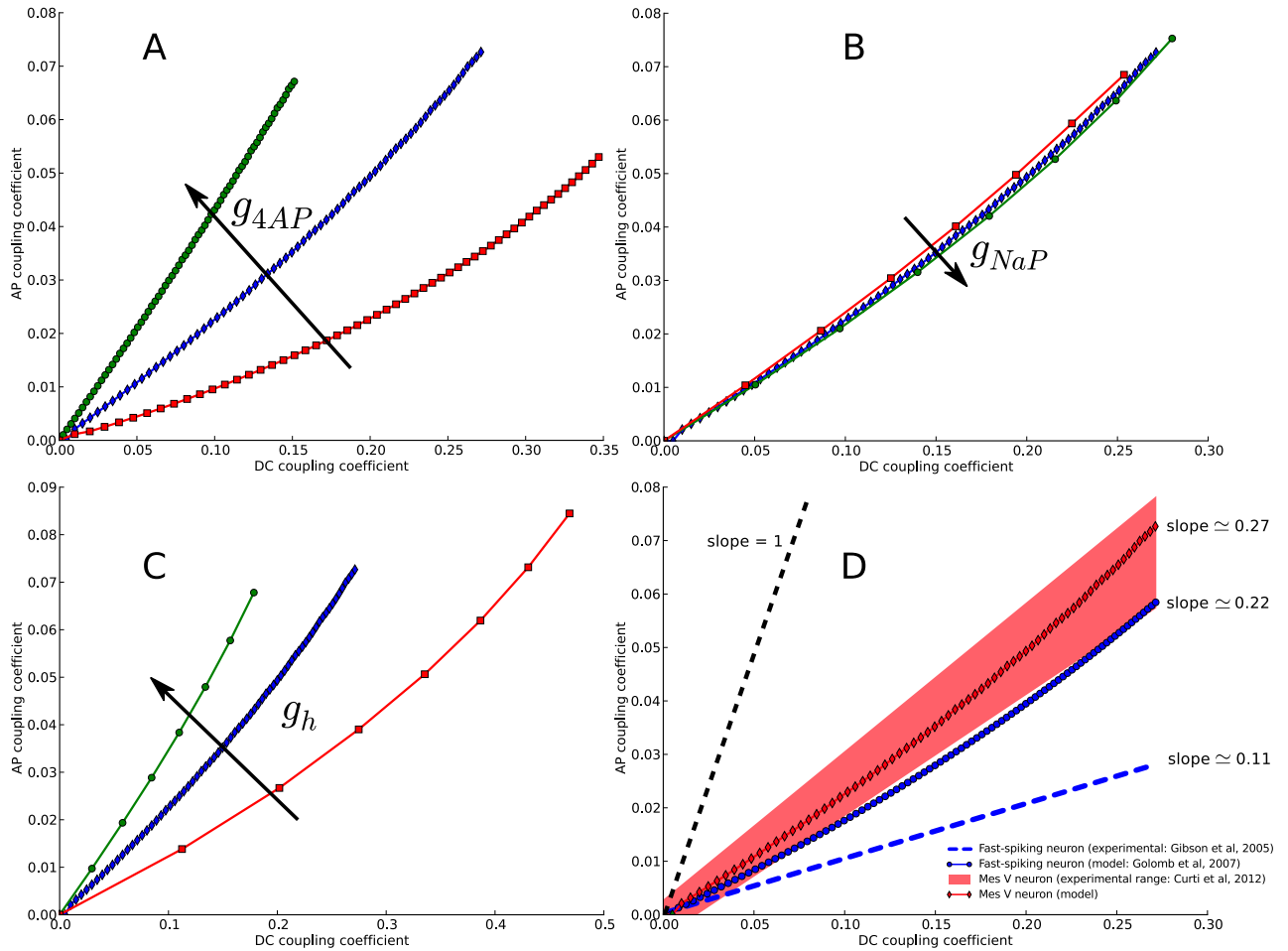

Figure 6.6: Action potential coupling against DC's, for different values of $\overline{g}_{4AP}$ (A), $\overline{g}_h$ (B) and $\overline{g}_{NaP}$ (C) Figure (D) compares Mes V model results to experimental ones (shaded area) and from fast spiking neurons [60].

6.5 Sensorial information processing

When the presynaptic neuron fires, the postsynaptic can be recruited or not, as it was shown in the previous section. In some cases, the postsynaptic response is a spikelet: a subthreshold response at the soma that may not propagate, because it lacks the regenerative behaviour of the sodium-mediated action potentials. On the other hand, the system can be wired in a way that both neurons receive a stimulus at the same time. Figure 6.7 shows that neurons may present repetitive firing when they receive simultaneous current injection at the soma, marking a more "important" message to motorneurons and/or central regions of the brain. Therefore, when there is a coincidence on the stimuli, neurons display a behaviour that they do not show when only one is stimulated.
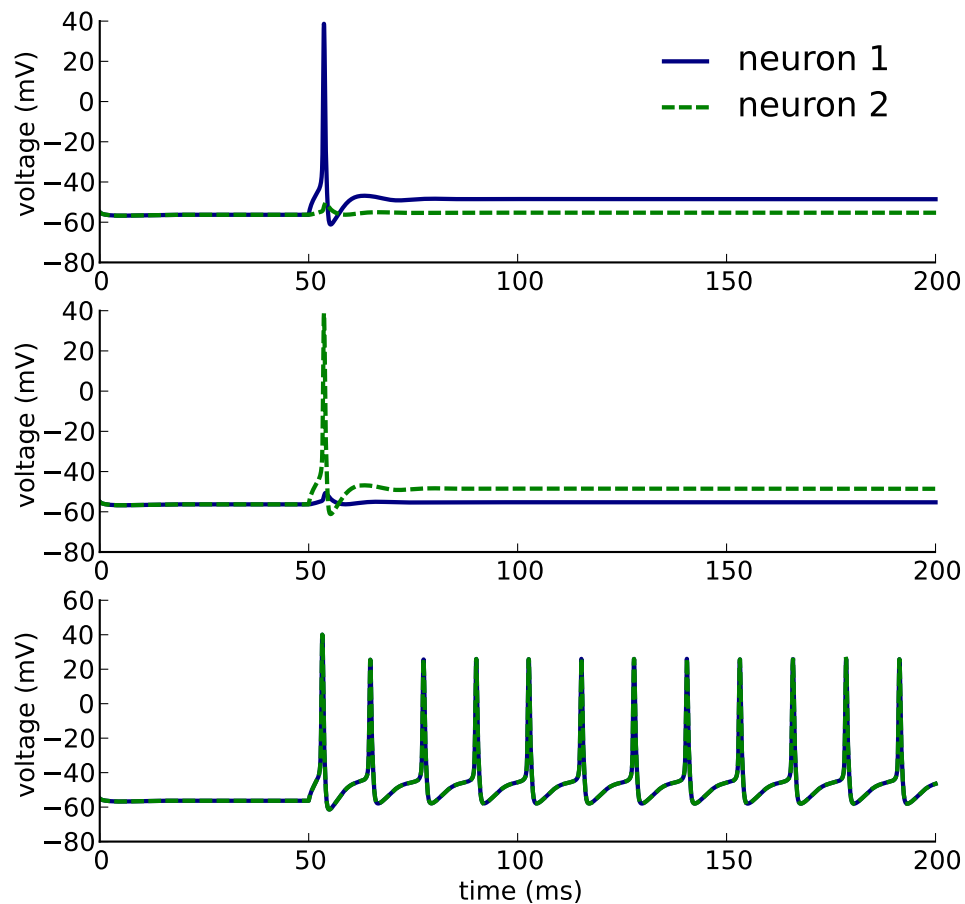

Figure 6.7: Coincidence detection in Mes V neurons. Only one neuron is stimulated in the first two horizontal figures, generating only one spike in the injected neuron and a spikelet in the other. However, if the stimulus is injected in both neurons, they present repetitive firing. The overall result is a larger response in the case of coincident stimuli.

While the protocol used in Figure 6.7 can be make at the lab, it is more difficult to implement a more functional test: to stimulate the peripheral axons, to see how

neurons cope with practical issues, such as time delays between sensorial inputs. In fact, it at least two complex several experimental issues. First, peripheral axon branches, from coupled neurons, have to be located at the tissue slice. Then, each one has to be stimulated independently, an almost impossible feat, given that it is very difficult to patch so tiny membrane portions.

On the other hand, it is quite easy to implement the experiment using simulations. The setup is shown in Figure 6.8A. Two identical coupled Mes V neurons are stimulated at their peripheries by synaptic inputs, with the same shape but different time delays. These inputs generate action potentials that travel through the cell, reaching the central axon, that operates as output port. If coupled neurons are coincidence detectors, they should reduce the delay at the output.

Simulations for different values of coupling strength g_j are presented in Figure 6.8 for control conditions (B) and increased $\overline{g}_{4AP}$ (C) or $\overline{g}_{NaP}$. The straight line corresponds to the case of no coupling ($g_j = 0$), where input and output delays are the same. Increased coupling means smaller output time delay for small input delays. However, after a time delay of $\simeq 7$ ms, the oppposite happens: output delay gets larger than the input. There is even a region without spikes, in control and increased $\overline{g}_{4AP}$.
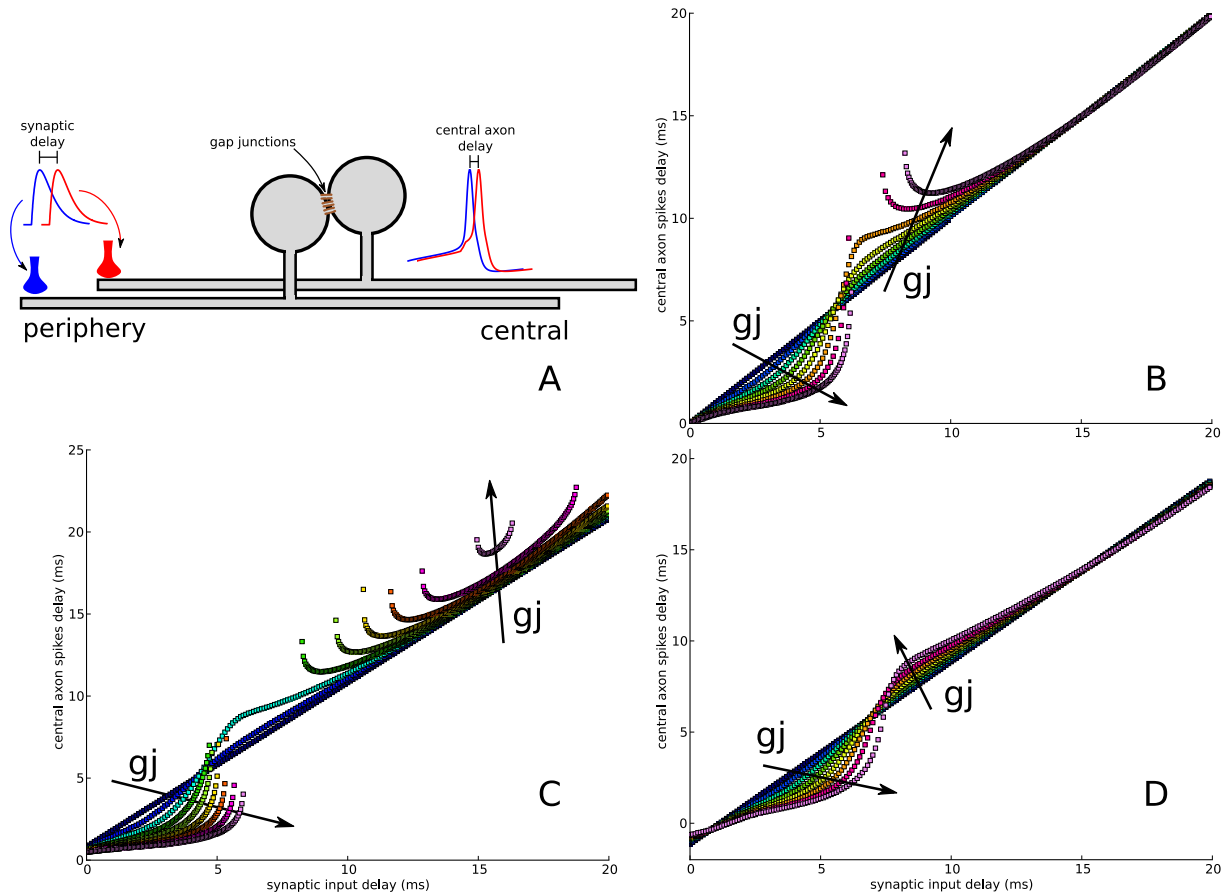
Figure 6.8: Coupling may generate coincidence detection or increased contrast in sensorial information. Two identical coupled neurons were stimulated by excitatory synaptic inputs at their peripheral axons (A). Each axon receives the same synaptic input, according to the synaptic conductances waveforms shown at the left, but with a variable temporal delay. These synaptic inputs generate action potentials that travel until the central axon, where their delay is measured again. Central axon delay is plotted against synaptic input delay in control conditions (B), increased $\overline{g}_{4AP}$ (C) and increased $\overline{g}_{NaP}$. Gap junction conductance g_j is varied from 0 to 7-8 nS, as indicated by black arrows.

Figure 6.9 shows what happens when $g_j = 3$ nS and $\overline{g}_{4AP}$ is increased. The left figure show the output delay - input delay curve in this case, marking some key points: small delay (a), large delay but with action potentials in both neurons (b), no action potential in the delayed cell (c) and (d), still larger delay (e) and (f). Voltage traces of all the cases are displayed at right. With a small delay(a), the two neurons cooperate, generating action potentials whose output delay is smaller. However, the neuron receiving the delayed input fails to fire in (c), due to an inhibition produced by the afterhyperpolarization potential (AHP) of its coupled cell. This phenomenon diminishes at (e) (both neurons fire again), but the onset of the second spike is still delayed by the AHP. Then, the system generates a larger output delay, separating both sensory signals in the temporal domain. Finally, a still larger input delay means that the two neurons fire almost independently.
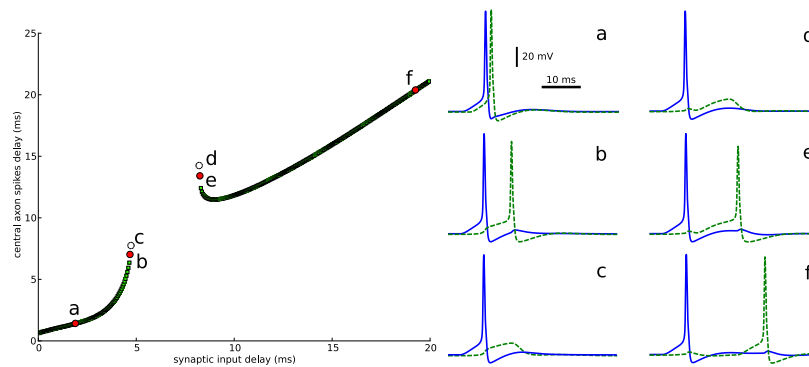
Figure 6.9: Coupled Mes V neurons may reduce or enlargen sensorial input delays with constant coupling strength. Red points in the left figure mark specific situations, whose voltage traces are shown at the right panel.

6.6 Summary

Synchronization of pairs of Mes V coupled neurons was studied in this chapter. Identical model cells were analyzed by phase reduction. Their phase response curves allowed to calculate phase locking of them, showing that in-phase synchronization is always stable, whereas antiphase $\Delta\phi = \pi$ not. Persistent sodium and 4-AP-sensitive current presented opposite results in most situations: excitability clases, frequency mismatch tolerance, stability trend of the antiphase solution, spike train delay AP efficiency, etc. Then, Mes V behaviour is shaped by a precise counterbalancing between these two currents.

Chapter 7

Conclusions and future work

Along this thesis, a biological system was studied using tools from engineering. Two ionic currents were modelled after experimental data, using nonlinear differential equations and Markov chains. For the first time, the Mes V sodium current is modelled taking into account the resurgent component (see appendix C). On the other hand, hyperpolarization-activated current modulation by cGMP is studied for the first time too.

A whole cell model of the Mes V neuron is obtained by using the cable theory and evolutionary algorithms. A reduced version of the model is used to study analytically and numerically the subthreshold transfer function resonance, challenging the general conception that electrical coupled neurons act as low-pass filters. It was also shown that modulated I_h may have an impact on the transfer function, though it will be necessary to check in the experimental model.

The synchronization between coupled neurons was also studied, using phase response curves and simulations. It was found that synchronization does not only depend on coupling strength, but also on the membrane properties. The efficiency of action potential coupling was also analyzed, as well as sensorial information processing.

The numerical simulations taken out during this thesis have generated answers to experimental questions, but they have also created new questions. One of them is sodium current time constants, that were successfully measured and then modelled, though more experimental recordings are needed to fully validate the model.

Another question is about the dynamics of high-threshold fast potassium current, that were adjusted by the optimization algorithm. Unfortunately, only one experiment was made using 4-aminopyridine, without any positive result. After reading some biophysical bibliography, we propose to measure the current using 1 mM TEA and TTX. On the other hand, given that any of the models completely fulfill the expected subthreshold behaviour, a more detailed inmunohistochemical characterization of ionic channels is needed, in order to check if there are Kv3 and

4-AP-sensitive channels in the axon (or at least in the initial segment).

Finally, more ambitious experiments will be needed to run an hybrid model, mixing real neurons and differential equations. Such experiments will allow to check the validity of the models and to explore the whole range of parameters in living neurons. A recording technique called *dynamic clamp* was studied to make that, but no proper equipment was available during this thesis. Opportunely, in December 2013 this equipment was purchased at the School of Medicine, making hybrid models possible.

Appendix A

Model parameters' values

The parameters used by the multicompartmental Mes V neuron model are:

Parameter	Value
Potassium reverse potential E_K (mV)	-93
Sodium reverse potential E_{Na} (mV)	78
I_h reverse potential E_h (mV)	-40.2
Specific intracellular resistance R_i (Ω.cm)	152.9 ± 30.8
Soma diameter D (μm)	43.7 ± 3.7
Axon length L (μm)	198.6 ± 7.2
Axon diameter d (μm)	3
Leak reverse potential E_L (mV)	-55.5 ± 0.4
Soma's leak conductance ($\mu\Omega/\text{cm}^2$)	40.2 ± 0.6
Axon's leak conductance ($\mu\Omega/\text{cm}^2$)	54.8 ± 0.6
Persistent sodium conductance $\overline{g}_{NaP}$ ($\mu\Omega/\text{cm}^2$)	20.9 ± 1.2
4-AP-sensitive potassium conductance $\overline{g}_{4AP}$ ($\mu\Omega/\text{cm}^2$)	229.2 ± 5.0
Hyperpolarization-activated conductance $\overline{g}_h$ ($\mu\Omega/\text{cm}^2$)	953.0 ± 30.5
Delayed rectifier conductance $\overline{g}_{DRK}$ ($\mu\Omega/\text{cm}^2$)	381.0 ± 82.3
Transient sodium conductance $\overline{g}_{NaT}$ ($m\Omega/\text{cm}^2$)	83.4 ± 6.1
Potassium Kv3 conductance $\overline{g}_{Kv3}$ ($m\Omega/\text{cm}^2$)	150.9 ± 6.7
$\tau_{Kv3\text{min}}$ (ms)	0.44 ± 0.03
$\tau_{Kv3\text{exp}}$ (ms)	0.63 ± 0.07

This page has been intentionally left blank

Appendix B

Evolutionary algorithms

Evolutionary algorithms are iterative optimization algorithms inspired in biological evolution [38]. The basic idea is to start with a "population" of subjects (for example, parameters' sets) whose fitness to a target function is measured. Only the best ones pass to the next generation, were they suffer mutation and combination, creating a new population. The process is repeated until the optimization goal is achieved.

In this thesis, the Evolutionary Multi-Objective Optimization (EMOO) tool[1] was employed to find model parameters. It was developed by Armin Bahl at the Max Planck Institute of Neurobiology (Germany) to fit a multicompartment model of pyramidal neurons [8], and it is possible to use it as a Python library. Then, it can interact with the Mes V neuron model, implemented using NEURON in Python.

The basic steps of this algorithm are [44]:

1. **Creation of individuals:** A population of N random solutions (whose parameters are random variations close to the initial guesses and vary within bounds) is generated intially.

2. **Selection:** Individuals from the population are pairwise compared in fitness and selected to fill a selection pool, that will have N individuals again. Then, the selection step has to be done twice.

3. **Crossover:** Parents are randomly taken from the selection pool and their parameters are combined, in order to generate two children with new parameters. The operator used by this tool is the simulated binary crossover [35], which starts by taking a random number $u_i \in [0, 1]$ from a uniform distri-

---

[1]Freely available at `http://projects.g-node.org/emoo`.

bution, that is used to obtain a new value β_{qi}:

$$
\beta_{qi} = \begin{cases} (2u_i)^{\frac{1}{\eta_c+1}} & \text{if } u_i \leq 0.5 \\ \dfrac{1}{2(1-u_i)}^{\frac{1}{\eta_c+1}} & \text{otherwise} \end{cases} \tag{B.1}
$$

Where η_c is a positive number chosen by the researcher (η_c=20 or 40 in this thesis). If x_i^1 and x_i^2 are the chosen parents, their offspring parameters y_i^1 and y_i^2 can be computed using β_{qi}:

$$
\begin{aligned}
y_i^1 &= 0.5 \left[(1+\beta_{qi})\, x_i^1 + (1-\beta_{qi})\, x_i^2 \right] \\
y_i^2 &= 0.5 \left[(1-\beta_{qi})\, x_i^1 + (1+\beta_{qi})\, x_i^2 \right]
\end{aligned} \tag{B.2}
$$

Parameters outside the predefined range are moved to the closest bound. Crossover continues until there are $C > N$ individuals in the whole population.

4. **Mutation:** Parameters diversity is increased by applying a polynomial mutation to each parameter from each individual. Again, a random number r_i is obtained from a uniform distribution, being used to compute δ_i:

$$
\delta_i = \begin{cases} (2r_i)^{\frac{1}{\eta_m+1}} - 1 & \text{if } r_i \leq 0.5 \\ 1 - [2(1-u_i)]^{\frac{1}{\eta_m+1}} & \text{otherwise} \end{cases} \tag{B.3}
$$

Again, η_m is a number tunned by the researcher ($\eta_m = \eta_c$ here). δ_i is added to the parameter, in order to generate a new one: $x_i \rightarrow x_i + \delta_i$.

5. **Evaluation:** Each individual is evaluated using error functions. In the multiobjective case, each individual will get M error values.

6. **Set fitness:** Each individual receives a fitness value, in order to establish a population ranking. Given that there could be M independent objectives, individuals are classified according to their nondomination rank. A solution is said to dominates the others if it is better in at least one objective, but not worse in the others. After finding the first set of nondominating solutions (called Pareto front), the rest of the population is evaluated again to get a second nondominating set. The individuals within each Pareto front are ranked using a "crowding distance" measure, that promotes the most isolated solutions in the parameter space.

7. **New generation**: N individuals are chosen to get a new population and start with the process again.

Appendix C

State-space sodium current model

The basic template for the Markov model of the sodium channel was presented in chapter 3 and it is presented in Figure C.1 again.
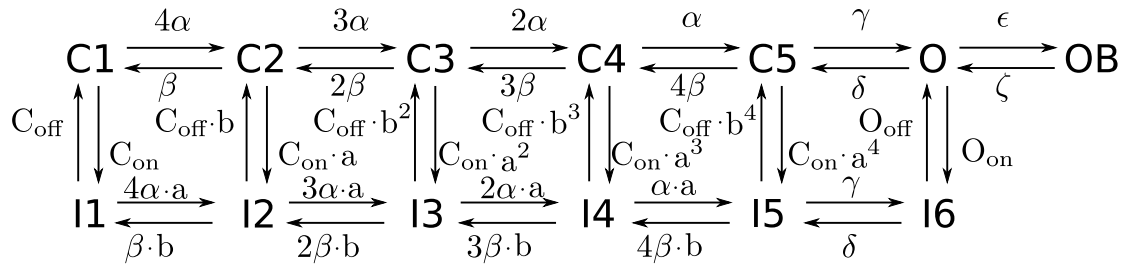

Figure C.1: Markov model of the sodium current [102]

Two different approaches were used to obtain the models' parameters from macroscopic current recordings:

- **Deterministic approach**: The Markov model is considered as a deterministic state-space model, described by a system of coupled differential equations. The optimization procedure can be divided in the following steps:

  1. The Prediction Error Method was used to find the parameters evaluated at each voltage, when the differential equations system is linear. This method -implemented as a part of the System Identification toolbox of Matlab [121]- finds the parameters of a linear model by minimizing the error between the data and the output of a linear filter that acts as a predictor [114, 169]. Parameters that do not vary too much in voltage will be taken as constant, whereas the other will be modelled as exponential rates $K_j = k_j e^{q_j V}$.

  2. The parameters of the Markov model in the whole voltage range are found using by multiobjective optimization using evolutionary algorithms [35], using a Python library developed by Bahl [8] and described in the appendix B.

3. Finally, these complex models could need some little hand tuning [45, 176], using the parameters that determine the features of the open state waveforms, according to its sensitivity $S(t) = \frac{\partial O}{\partial p}$. For example, the transition rate from inactivation to the open state, O_{on} is relevant to set the steady state of the O state, i.e. the persistent sodium current.

- **Stochastic approach**: In this case, parameters are found using the maximum likelihood estimation algorithm from QUB software [124]. Briefly, the master equation is solved to find the states occupancy for a given set of parameters θ. Then, the program computes the conditional probability of the macroscopic recorded current I given the parameters: $L = p(I|\theta)$, where L is called the likelihood function. The parameter space is explored by simplex and quasi-Newton methods [134], in order to maximize the likelihood function. Given that the master equation gives the state occupancy of a single channel, QUB also estimates the total number of channels.

The basic model is shown in Figure C.1, with the rates presented there, and will be called "Khaliq fit", given that it is basically the model reported by him and his coworkers [102], but with different parameters. A less strict version of it, called "standard mode" has the same structure, but its kinetic rates are independent between them, being only contraint by microscopic reversibility. Two reduced variations of the standard model were also simulated. The first one has no OB state: it will be called standard model without resurgent current. The other variation is the standard without two states (C_1 and I_1), i.e. without a "gate" in HH terms.

Figure C.2 presents the simulations' result (parameter values can be found in appendix A). Without any fitting, the Khaliq model (A) resembles more the data than the model by del Negro and Chandler [133] (see Figure 3.10). Fitting the parameters, the model increases the difference between peak currents (B). These differences improve also in the standard model, when all the parameters are set free and only contraint by biophysical conditions (C). In addition to that, its times to peak increase too, being more similar to the experimental ones. The standard model without 2 states (D) displays a similar behaviour, with a longer inactivation. Finally, the standard model without resurgent current displays slower activation and inactivation times, simultaneously. The error e_k between simulations $s_k(t)$ and recordings $d_k(t)$ for each voltage was computed as:

$$e_k = \frac{\|d_k(t) - s_k(t)\|_2}{\|d_k(t)\|_2}, \qquad k = 1, \dots, 16 \qquad (C.1)$$

The errors plotted in (F) prove what it was explained above. The best fit in the whole range is achieved by the standard model, followed closely by its variations. The resurgent component appears to be important in the lowest 5-mV range, coherent with the range where it is maximum [41, 146]. The overall picture shows that, in general, the biggest errors are in the lowest range, where baseline offsets may be relevant.
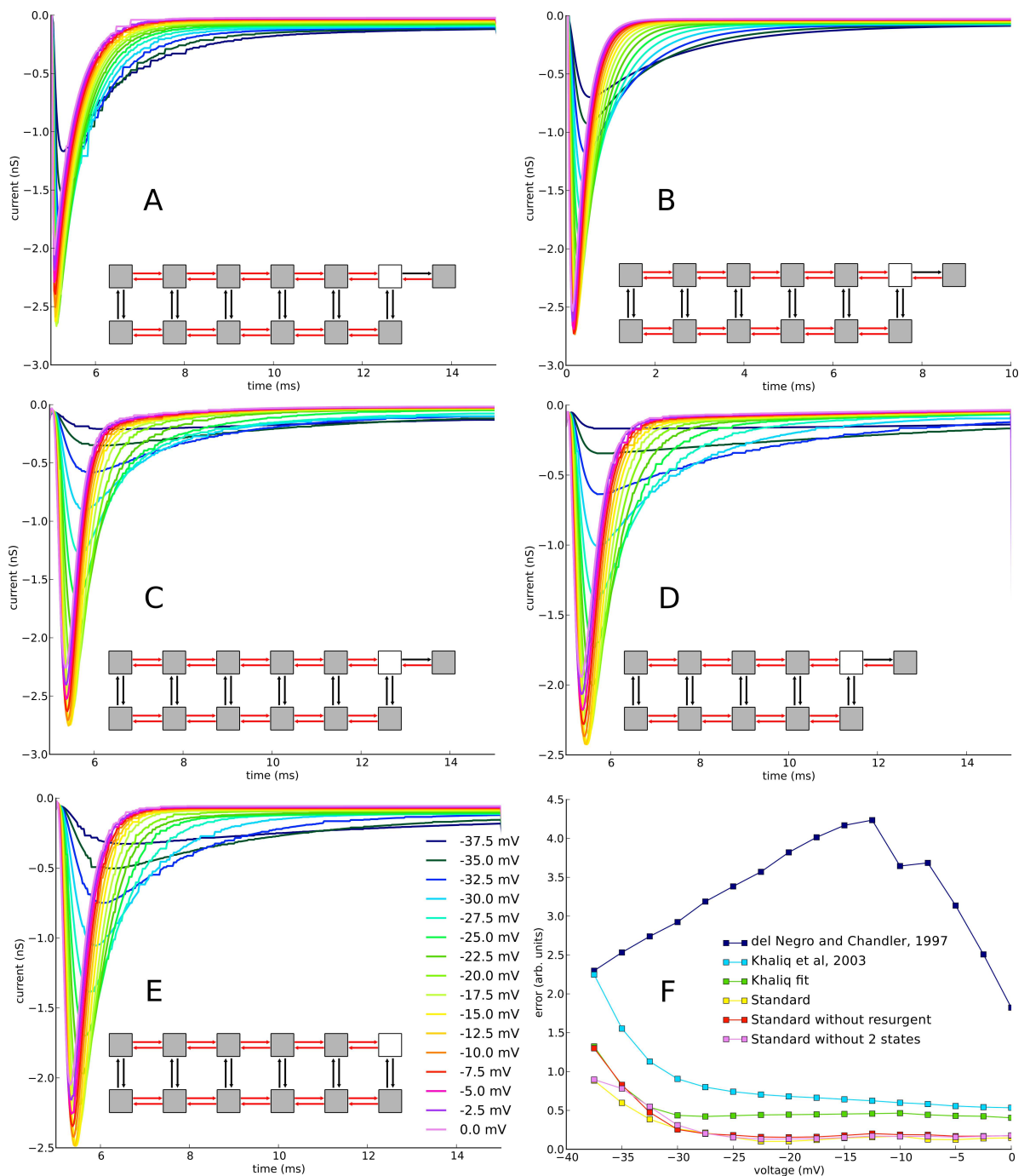
Figure C.2: Simulations of Markov models. From left to right and from top to bottom, simulations from: original model from Khaliq et al [102] (A), the same structure but with fitted values (B), the standard model (C), and it without two states (D) or without the OB state (E). Below each group of traces, there is a little scheme of the Markov model used. The white box denotes the open state O, whereas the grey ones are nonconductive states: inactived (bottom of the chain), closed (top, at the left of O) and blocked state (at the right of O). Red arrows are voltage dependent (in an exponential manner) and black ones are constant. The error curves between simulations and experimental traces (F) show that the best model is the standard.

This page has been intentionally left blank

Bibliography

[1] Laurence F. Abbott. Lapicque's introduction of the integrate-and-fire model neuron (1907). *Brain Research Bulletin*, 50:303–304, 1999.

[2] Pablo Achard and Erik De Schutter. Complex parameter landscape for a complex neuron model. *PLoS Comput Biol*, 2(7):e94, 07 2006.

[3] Pablo Achard, Werner Van Geit, and Gwendal LeMasson. Parameter searching. In Erik de Schutter, editor, *Computational Modeling Methods for Neuroscientists*, Results and Problems in Cell Differentiation, pages 31–60. The MIT Press, 2010.

[4] Fatemeh S Afshari, Krzysztof Ptak, Zayd M Khaliq, Tina M Grieco, N Traverse Slater, Donald R McCrimmon, and Indira M Raman. Resurgent Na currents in four classes of neurons of the cerebellum. *Journal of Neurophysiology*, 92(5):2831–43, November 2004.

[5] Walther Akemann and Thomas Knöpfel. Interaction of kv3 potassium channels and resurgent sodium current influences the rate of spontaneous firing of purkinje neurons. *The Journal of Neuroscience*, 26(17):4602–4612, 2006.

[6] Veronica a Alvarez, Carson C Chow, Elisabeth J Van Bockstaele, and John T Williams. Frequency-dependent synchrony in locus ceruleus: role of electrotonic coupling. *Proceedings of the National Academy of Sciences of the United States of America*, 99(6):4032–6, March 2002.

[7] Joseph M. Amatrudo, Christina M. Weaver, Johanna L. Crimins, Patrick R. Hof, Douglas L. Rosene, and Jennifer I. Luebke. Influence of highly distinctive structural properties on the excitability of pyramidal neurons in monkey visual and prefrontal cortices. *The Journal of Neuroscience*, 32(40):13644–13660, 2012.

[8] Armin Bahl, Martin B. Stemmler, Andreas V.M. Herz, and Arnd Roth. Automated optimization of a reduced layer 5 pyramidal cell model based on experimental data. *Journal of Neuroscience Methods*, 210(1):22 – 34, 2012. Special Issue on Computational Neuroscience.

[9] R. Baker and R. Llinás. Electrotonic coupling between neurones in the rat mesencephalic nucleus. *The Journal of Physiology*, 212(1):45–63, 1971.

Bibliography

[10] Gytis Baranauskas and Marco Martina. Sodium currents activate without a Hodgkin-and-Huxley-type delay in central mammalian neurons. *The Journal of Neuroscience*, 26(2):671–84, January 2006.

[11] Douglas A. Baxter, Carmen C. Canavier, John W. Clark, and John H. Byrne. Computational model of the serotonergic modulation of sensory neurons in aplysia. *Journal of Neurophysiology*, 82(6):2914–2935, 1999.

[12] Bruce P Bean. The action potential in mammalian central neurons. *Nature Reviews Neuroscience*, 8:451–465, 2007.

[13] O Belluzzi and O Sacchi. A five-conductance model of the action potential in the rat sympathetic neurone. *Progress in biophysics and molecular biology*, 55(1):1–30, January 1991.

[14] Michael VL Bennett and R Suzanne Zukin. Electrical coupling and neuronal synchronization in the mammalian brain. *Neuron*, 41 (4):495–511, 2004.

[15] Michele Bezzi, Thierry Nieusb, Olivier J.-M. Coenena, and Egidio D'Angelob. An integrate-and-fire model of a cerebellar granule cell. *Neurocomputing*, 58–60:593–595, 2004.

[16] U. S. Bhalla and J. M. Bower. Exploring parameter space in detailed single neuron models: simulations of the mitral and granule cells of the olfactory bulb. *Journal of Neurophysiology*, 69(6):1948–1965, 1993.

[17] Nicolas Brunel and Peter Latham. Firing rate of the noisy quadratic integrate-and-fire neuron. *Neural Computation*, 15(10):2281–2306, 2003.

[18] Carmen C. Canavier and Srisairam Achuthan. Pulse coupled oscillators and the phase resetting curve. *Mathematical Biosciences*, 226(2):77–96, 2010.

[19] Lorenzo Cangiano, Claudia Gargini, Luca Della Santina, Gian Carlo Demontis, and Luigi Cervetto. High-pass filtering of input signals by the Ih current in a non-spiking neuron, the retinal rod bipolar cell. *PloS one*, 2(12):e1327, January 2007.

[20] Robert C Cannon and Giampaolo D'Alessandro. The ion channel inverse problem: Neuroinformatics meets biophysics. *PLoS Comput Biol*, 2(8):e91, 08 2006.

[21] Nicholas T. Carnevale and Michael L. Hines. *The NEURON Book*. Cambridge University Press, 2004.

[22] Enrico Cataldo, Marcello Brunelli, John H. Byrne, Evyatar Av-Ron, Yidao Cai, and Douglas A. Baxter. Computational model of touch sensory cells (t cells) of the leech: Role of the afterhyperpolarization (ahp) in activity-dependent conduction failure. *Journal of Computational Neuroscience*, 18(1):5–24, 2005.

[23] William A Catterall. From ionic currents to molecular mechanisms: The structure and function of voltage-gated sodium channels. *Neuron*, 26(1):13 – 25, 2000.

[24] William A. Catterall, Indira M. Raman, Hugh P. C. Robinson, Terrence J. Sejnowski, and Ole Paulsen. The hodgkin-huxley heritage: From channels to circuits. *The Journal of Neuroscience*, 32(41):14064–14073, 2012.

[25] Fei Chen and Yuan-Ting Zhang. An integrate-and-fire-based auditory nerve model and its response to high-rate pulse train. *Neurocomputing*, 70:1051–1055, 2007.

[26] Raymond A. Chitwood, Aida Hubbard, and David B. Jaffe. Passive electrotonic properties of rat hippocampal ca3 interneurones. *Journal of Physiology*, 515.3:743–756, 1999.

[27] William A Coetzee, Yimy Amarillo, Joanna Chiu, Alan Chow, David Lau, Herman Moreno, Marcela S Nadal, Ander Ozaita, David Pountney, Michael Saganich, Eleazar Vega-saenz D E Miera, and Bernardo Rudy. Molecular diversity of k+ channels. *Annals of the New York Academy of Sciences*, 868:212–263, 1999.

[28] David Colquhoun and AlanG. Hawkes. A q-matrix cookbook. In Bert Sakmann and Erwin Neher, editors, *Single-Channel Recording*, pages 589–633. Springer US, 1995.

[29] J.A. Connor and C.F. Stevens. Prediction of repetitive firing behaviour from voltage clamp data on an isolated neurone soma. *The Journal of Physiology*, 213(1):31–53, 1971.

[30] J.A. Connor and C.F. Stevens. Voltage clamp studies of a transient outward membrane current in gastropod neural somata. *Journal of Physiology*, 213:21–30, 1971.

[31] Barry W. Connors, Timothy A Zolnik, and Seung-Chan Lee. Enhanced functions of electrical junctions. *Neuron*, 67 (3):354–357, 2010.

[32] Geoffrey M. Cooper. *The Cell: A Molecular Approach*. Sunderland, 2nd edition, 2000.

[33] Sebastian Curti, Gregory Hoge, James I. Nagy, and Alberto Pereda. Synergy between electrical coupling and membrane promotes strong synchronization of neurons of the mesencephalic trigeminal nucleus. *Journal of Neuroscience*, 32(13):4341–4359, 2012.

[34] Peter Dayan and Laurence F. Abbott. *Theoretical Neuroscience*. MIT Press, Cambridge, 2001.

[35] Kalyanmoy Deb and Deb Kalyanmoy. *Multi-Objective Optimization Using Evolutionary Algorithms*. Wiley, 1 edition, June 2001.

Bibliography

[36] Alain Destexhe. Kinetic models of membrane excitability and synaptic interactions. In J Bower and H Bolouri, editors, *Computational Models of Molecular and Cellular Interactions*. 1998.

[37] Alain Destexhe and John R. Huguenard. Nonlinear thermodynamic models of voltage-dependent currents. *Journal of Computational Neuroscience*, 9(3):259–270, 2000.

[38] Shaul Druckmann, Yoav Banitt, Albert A Gidon, Felix Schürmann, Henry Markram, and Idan Segev. A novel multiple objective optimization framework for constraining conductance-based neuron models by experimental data. *Frontiers in Neuroscience*, 1(1), 2007.

[39] Shaul Druckmann, Thomas K Berger, Felix Schürmann, Sean Hill, Henry Markram, and Idan Segev. Effective stimuli for constructing reliable neuron models. *PLoS computational biology*, 7(8):e1002133, August 2011.

[40] Guillaume P Dugué, Nicolas Brunel, Vincent Hakim, Eric Schwartz, Mireille Chat, Maxime Lévesque, Richard Courtemanche, Clément Léna, and Stéphane Dieudonné. Electrical coupling mediates tunable low-frequency oscillations and resonance in the cerebellar Golgi cell network. *Neuron*, 61(1):126–39, January 2009.

[41] Akifumi Enomoto, Juliette M Han, Chie-Fang Hsiao, and Scott H Chandler. Sodium currents in mesencephalic trigeminal neurons from nav1.6 null mice. *Journal of Neurophysiology*, 98(2):710–719, 2007.

[42] Akifumi Enomoto, Juliette M Han, Chie-Fang Hsiao, Nanping Wu, and Scott H Chandler. Participation of sodium currents in burst generation and control of membrane excitability in mesencephalic trigeminal neurons. *The Journal of neuroscience : the official journal of the Society for Neuroscience*, 26(13):3412–22, March 2006.

[43] Bard Ermentrout and N. Kopell. Parabolic bursting in an excitable system coupled with a slow oscillation. *SIAM Journal on Applied Mathematics*, 46:233–253, 1986.

[44] Hilda Faraji. *Automated Optimization of a Reduced Layer 5 Pyramidal Cell Model Based on Experimental Data*. PhD thesis, Humboldt-Universitat zu Berlin, 2009.

[45] Martin Fink and Denis Noble. Markov models for ion channels: versatility versus identifiability and speed. *Philosophical Transactions of the Royal Society A: Mathematical, Physical and Engineering Sciences*, 367(1896):2161–2179, 2009.

[46] Richard FitzHugh. Impulses and physiological states in theoretical models of nerve membrane. *Biophysical Journal*, 1:445–466, 1961.

[47] Michael D. Forrest. Mathematical model of bursting in dissociated purkinje neurons. *PLoS ONE*, 8(8):e68765, 08 2013.

[48] Michael D. Forrest, Mark J. Wall, Daniel A. Press, and Jianfeng Feng. The sodium-potassium pump controls the intrinsic firing of the cerebellar purkinje neuron. *PLoS ONE*, 7(12):e51169, 12 2012.

[49] Pierre A. Fortier. Detecting and estimating rectification of gap junction conductance based on simulations of dual-cell recordings from a pair and a network of coupled cells. *Journal of Theoretical Biology*, 265(2):104 – 114, 2010.

[50] Nicolas Fourcaud-Trocmé, David Hansel, Carl van Vreeswijk, and Nicolas Brunel. How spike generation mechanisms determine the neuronal response to fluctuating inputs. *The Journal of Neuroscience : the official journal of the Society for Neuroscience*, 23:11628–11640, 2003.

[51] Pedro Freire Costa. The kinetic parameters of sodium currents in maturing acutely isolated rat hippocampal CA1 neurones. *Developmental Brain Research*, 91:29–40, 1996.

[52] Tomohiro Fujita, Tomoki Fukai, and Katsunori Kitano. Influences of membrane properties on phase response curve and synchronization stability in a model globus pallidus neuron. *Journal of computational neuroscience*, 32(3):539–53, June 2012.

[53] E. J. Furshpan and D. D. Potter. Transmission at the giant motor synapses of the crayfish. *The Journal of Physiology*, 145(2):289–325, 1959.

[54] Juan Gao and Philip Holmes. On the dynamics of electrically-coupled neurons with inhibitory synapses. *Journal of computational neuroscience*, 22(1):39–61, February 2007.

[55] L. L. Gao, S. McMullan, L. Djouhri, C. Acosta, A. A. Harper, and S. N. Lawson. Expression and properties of hyperpolarization-activated current in rat dorsal root ganglion neurons with known sensory function. *The Journal of Physiology*, 590(19):4691–4705, 2012.

[56] Angelo Di Garbo. The electrical coupling confers to a network of interneurons the ability of transmitting excitatory inputs with high temporal precision. *Brain Research*, 1225(0):47 – 56, 2008. Brain and Vision.

[57] Juan Mauricio Garré and Michael V.L. Bennett. Gap junctions as electrical synapses. In Hisashi Umemori and Michael Hortsch, editors, *The Sticky Synapse*, pages 423–439. Springer New York, 2009.

[58] Luc J. Gentet, Greg J. Stuart, and John D. Clements. Direct measurement of specific membrane capacitance in neurons. *Biophysical Journal*, 79(1):314–320, 2000.

Bibliography

[59] Jay R Gibson, Michael Beierlein, and Barry W Connors. Functional properties of electrical synapses between inhibitory interneurons of neocortical layer 4. *Journal of Neurophysiology*, 93(1):467–80, January 2005.

[60] David Golomb, Cuiyong Yue, and Yoel Yaari. Contribution of persistent na+ current and m-type k+ current to somatic bursting in ca1 pyramidal cells: Combined experimental and modeling study. *Journal of Neurophysiology*, 96(4):1912–1926, 2006.

[61] John Guckenheimer, Shay Gueron, and Ronald M. Harris-Warrick. Mapping the dynamics of a bursting neuron. *Philosophical Transactions of the Royal Society of London. Series B: Biological Sciences*, 341(1298):345–359, 1993.

[62] Yoram Gutfreund, Yosef Yarom, and Idan Segev. Subthreshold oscillations and resonant frequency in guinea-pig cortical neurons: physiology and modelling. *Journal of Physiology*, 483:621–640, 1995.

[63] Boris S Gutkin, G Bard Ermentrout, and Alex D Reyes. Phase-response curves give the responses of neurons to transient inputs. *Journal of Neurophysiology*, 94(2):1623–35, August 2005.

[64] Julie S. Haas and John A. White. Frequency selectivity of layer II stellate cells in the medial entorhinal cortex. *Journal of Neurophysiology*, 88(5):2422–9, November 2002.

[65] Hermann Haken. *Synergetics: An Introduction*. Springer-Verlag, 1977.

[66] Verena Hammelmann, Xiangang Zong, Franz Hofmann, Stylianos Michalakis, and Martin Biel. The cgmp-dependent protein kinase ii is an inhibitory modulator of the hyperpolarization-activated hcn2 channel. *PLoS ONE*, 6(2):e17078, 02 2011.

[67] David Hansel and Germán Mato. Asynchronous states and the emergence of synchrony in large networks of interacting excitatory and inhibitory neurons. *Neural Computation*, 15:1–56, 2003.

[68] Neil Hardingham, James Dachtler, and Kevin Fox. The role of nitric oxide in pre-synaptic plasticity and homeostasis. *Frontiers in Cellular Neuroscience*, 7(190), 2013.

[69] Neil Herring, Lauren Rigg, Derek A Terrar, and David J Paterson. No-cgmp pathway increases the hyperpolarisation-activated current, if, and heart rate during adrenergic stimulation. *Cardiovascular Research*, 52(3):446–453, 2001.

[70] Andreas V. M. Herz, Tim Gollisch, Christian K. Machens, and Dieter Jaeger. Modeling single-neuron dynamics and computations: A balance of detail and abstraction. *Science*, 314(5796):80–85, 2006.

[71] Bertil Hille. *Ion Channels of Excitable Membranes*. Sinauer Associates, 3rd edition edition, 2001.

[72] Shinn-Ying Ho, Li-Sun Shu, and Jian-Hung Chen. Intelligent evolutionary algorithms for large parameter optimization problems. *Evolutionary Computation, IEEE Transactions on*, 8(6):522–541, 2004.

[73] AL Hodgkin. The Ionic Basis of Nervous Conduction. *Science*, 145:1148–1154, 1964.

[74] AL Hodgkin and AF Huxley. A quantitative description of membrane current and its application to conduction and excitation in nerve. *The Journal of Physiology*, 117(4):500–544, 1952.

[75] AL Hodgkin and AF Huxley. Currents carried by sodium and potassium ions through the membrane of the giant axon of Loligo. *The Journal of Physiology*, 116:449–472, 1952.

[76] AL Hodgkin and AF Huxley. The dual effect of membrane potential on sodium conductance in the giant axon of loligo. *The Journal of Physiology*, 116:497–506, 1952.

[77] AL Hodgkin and AF Huxley. Measurement of current-voltage relations in the membrane of the giant axon of Loligo. *The Journal of physiology*, pages 424–448, 1952.

[78] AL Hodgkin and AF Huxley. The components of membrane conductance in the giant axon of Loligo. *The Journal of physiology*, 116:473–496, 1952.

[79] Sheriar G. Hormuzdi, Mikhail A. Filippov, Georgia Mitropoulou, Hannah Monyer, and Roberto Bruzzone. Electrical synapses: a dynamic signaling system that shapes the activity of neuronal networks. *Biochimica et Biophysica Acta (BBA) - Biomembranes*, 1662(1–2):113 – 137, 2004. The Connexins.

[80] Chie-Fang Hsiao, Gurvinder Kaur, Angela Vong, Harpreet Bawa, and Scott H Chandler. Participation of Kv1 channels in control of membrane excitability and burst generation in mesencephalic V neurons. *Journal of Neurophysiology*, 101(3):1407–18, March 2009.

[81] JR Huguenard and D.A. McCormick. Simulation of the currents involved in rhythmic oscillations in thalamic relay neurons. *Journal of Neurophysiology*, 68(4):1373–1383, 1992.

[82] B Hutcheon, R M Miura, and E Puil. Models of subthreshold membrane resonance in neocortical neurons. *Journal of Neurophysiology*, 76(2):698–714, August 1996.

[83] B Hutcheon, R M Miura, Y Yarom, and E Puil. Low-threshold calcium current and resonance in thalamic neurons: a model of frequency preference. *Journal of Neurophysiology*, 71(2):583–94, February 1994.

Bibliography

[84] Bruce Hutcheon and Yosef Yarom. Resonance, oscillation and the intrinsic frequency preferences of neurons. *Trends in neurosciences*, 23(5):216–22, May 2000.

[85] E. M. Izhikevich and R. FitzHugh. Fitzhugh-nagumo model. 1(9):1349, 2006.

[86] Eugene Izhikevich. Simple model of spiking neurons. *Neural Networks, IEEE Transactions on*, 14(6):1569–1572, 2003.

[87] Eugene Izhikevich. Which model to use for cortical spiking neurons? *IEEE Transactions on Neural Networks*, 15:1063–1070, 2004.

[88] Eugene Izhikevich. *Dynamical Systems in Neuroscience: The Geometry of Excitability and Bursting*, volume 38. The MIT Press, 2007.

[89] Eugene Izhikevich and Bard Ermentrout. Phase model. *Scholarpedia*, 3(10):1487, 2008.

[90] Eugene M Izhikevich. Resonate-and-fire neurons. *Neural Networks*, 14:883–894, 2001.

[91] Dieter Jaeger, Erik De Schutter, and James M. Bower. The role of synaptic and voltage-gated currents in the control of purkinje cell spiking: A modeling study. *The Journal of Neuroscience*, 17(1):91–106, 1997.

[92] Daniel Johnston and Samuel Miao-Sin Wu. *Foundations of Cellular Neurophysiology*. MIT Press, 1997.

[93] Jamie Johnston, Ian D Forsythe, and Conny Kopp-Scheinpflug. Going native: voltage-gated potassium channels controlling neuronal excitability. *The Journal of physiology*, 588(Pt 17):3187–200, September 2010.

[94] Eric R. Kandel, J. H. Schwartz, and Thomas M. Jessell. *Principles of Neural Science*. McGraw-Hill Medical, July 2000.

[95] Youngnam Kang, Mitsuru Saito, Hajime Sato, Hiroki Toyoda, Yoshinobu Maeda, Toshihiro Hirai, and Yong-Chul Bae. Involvement of persistent Na+ current in spike initiation in primary sensory neurons of the rat mesencephalic trigeminal nucleus. *Journal of Neurophysiology*, 97(3):2385–93, March 2007.

[96] Alan R. Kay, Mutsuyuki Sugimori, and Rodolfo Llinás. Kinetic and stochastic properties of a persistent sodium current in mature guinea pig cerebellar purkinje cells. *Journal of Neurophysiology*, 80(3):1167–1179, 1998.

[97] Temel Kayikcioglu and Vedat Ozkaner. A new description for sodium channel gating model based on macroscopic ionic currents in dissociated cerebellar purkinje neurons. *Physica A*, 343:487–498, 2004.

[98] Justin Keat, Pamela Reinagel, R. Clay Reid, and Markus Meister. Predicting every spike: A model for the responses of visual neurons. *Neuron*, 30:803–17, 2001.

[99] Naomi Keren, Dan Bar-Yehuda, and Alon Korngreen. Experimentally guided modelling of dendritic excitability in rat neocortical pyramidal neurones. *The Journal of Physiology*, 587(7):1413–1437, 2009.

[100] S O M Ketelaars, J A Gorter, E A Van Vliet, and W J Wadman. Sodium currents in isolated rat ca1 pyramidal and dentate granule neurones in the post-status epilepticus model of epilepsy. *Neuroscience*, 105(1):109–120, 2001.

[101] Baljit S. Khakh and Graeme Henderson. Hyperpolarization-activated cationic currents (ih) in neurones of the trigeminal mesencephalic nucleus of the rat. *Journal of Physiology*, 510.3:695–704, 1998.

[102] Zayd M Khaliq, Nathan W Gouwens, and Indira M Raman. The contribution of resurgent sodium current to high-frequency firing in Purkinje neurons: an experimental and modeling study. *The Journal of neuroscience : the official journal of the Society for Neuroscience*, 23(12):4899–912, June 2003.

[103] O. Kiehn and R. M. Harris-Warrick. 5-ht modulation of hyperpolarization-activated inward current and calcium-dependent outward current in a crustacean motor neuron. *Journal of Neurophysiology*, 68(2):496–508, 1992.

[104] Bruce W. Knight. Dynamics of encoding in a population of neurons. *The Journal of General Physiology*, 59:734–766, 1972.

[105] Chung-Chin Kuo and Bruce P Bean. Na+ Channels Must Deactivate to Recover from Inactivation. *Neuron*, 12:819–829, 1994.

[106] Carole E. Landisman, Michael A. Long, Michael Beierlein, Michael R. Deans, David L. Paul, and Barry W. Connors. Electrical synapses in the thalamic reticular nucleus. *The Journal of Neuroscience*, 22(3):1002–1009, 2002.

[107] Nikolai E Lazarov. The Neurochemical Anatomy of Trigeminal Primary Afferent Neurons. 2009.

[108] Nikolai E. Lazarov and Manfred Gratzl. Selective expression of histamine receptors in rat mesencephalic trigeminal neurons. *Neuroscience Letters*, 404(1–2):67 – 71, 2006.

[109] Harold Lecar. Morris-lecar model. *Scholarpedia*, 2(10):1333, 2007.

[110] Sabina Leonelli. What is in a model? using theoretical and material models to develop intelligible theories. In Manfred Dietrich Laubichler and Gerd B. Müller, editors, *Modeling Biology: Structures, Behavior, Evolution*. MIT Press, 2006.

Bibliography

[111] Alan S. Lewis and Dane M. Chetkovich. {HCN} channels in behavior and neurological disease: Too hyper or not active enough? *Molecular and Cellular Neuroscience*, 46(2):357 – 367, 2011.

[112] Jin-Lian Li, Kang-Hui Xiong, Yun-Qing Li, Takeshi Kaneko, and Noboru Mizuno. Serotonergic innervation of mesencephalic trigeminal nucleus neurons: a light and electron microscopic study in the rat. *Neuroscience Research*, 37(2):127 – 140, 2000.

[113] Yihui Liu, Jing Yang, and Sanjue Hu. Transition between two excitabilities in mesencephalic V neurons. *Journal of computational neuroscience*, 24(1):95–104, February 2008.

[114] Lennart Ljung. *System identification: Theory for the User.* 1987.

[115] G Maccaferri and C J McBain. The hyperpolarization-activated current (ih) and its contribution to pacemaker activity in rat ca1 hippocampal stratum oriens-alveus interneurones. *The Journal of Physiology*, 497(Pt 1):119–130, 1996.

[116] Jacopo Magistretti, Loretta Castelli, Lia Forti, and Egidio D'Angelo. Kinetic and functional analysis of transient, persistent and resurgent sodium currents in rat cerebellar granule cells in situ: an electrophysiological and modelling study. *The Journal of physiology*, 573(Pt 1):83–106, May 2006.

[117] G Major, AU Larkman, P Jonas, B Sakmann, and JJ Jack. Detailed passive cable models of whole-cell recorded ca3 pyramidal neurons in rat hippocampal slices. *The Journal of Neuroscience*, 14(8):4613–4638, 1994.

[118] Jaime G. Mancilla, Timothy J. Lewis, David J. Pinto, John Rinzel, and Barry W. Connors. Synchronization of electrically coupled pairs of inhibitory interneurons in neocortex. *The Journal of Neuroscience*, 27(8):2058–2073, 2007.

[119] Susanna Manrubia, Alexander Mikailov, and Damian Zanette. *Emergence of Dynamical Order: Synchronization Phenomena in Complex Systems.* World Scientific, 2004.

[120] Eduardo Marban, Toshio Yamagishi, and Gordon F. Tomaselli. Structure and function of voltage-gated sodium channels. *Journal of Physiology*, 508(3):647–657, 1998.

[121] MATLAB. *version 7.12.0 (R2011a).* The MathWorks Inc., Natick, Massachusetts, 2011.

[122] D A McCormick and H C Pape. Properties of a hyperpolarization-activated cation current and its role in rhythmic oscillation in thalamic relay neurones. *The Journal of Physiology*, 431(1):291–318, 1990.

[123] Carola Meier and Rolf Dermietzel. Electrical synapses – gap junctions in the brain. In EckartD. Gundelfinger, ConstanzeI. Seidenbecher, and Burkhart Schraven, editors, *Cell Communication in Nervous and Immune System*, volume 43 of *Results and Problems in Cell Differentiation*, pages 99–128. Springer Berlin Heidelberg, 2006.

[124] Lorin S. Milescu, Gustav Akk, and Sachs Frederick. Maximum likelihood estimation of ion channel kinetics from macroscopic currents. *Biophysical Journal*, 88:2494–2515, 2005.

[125] Lorin S. Milescu, Tadashi Yamanishi, Krzysztof Ptak, and Jeffrey C. Smith. Kinetic properties and functional dynamics of sodium channels during repetitive spiking in a slow pacemaker neuron. *Journal of Neuroscience*, 30(36):12113–12127, 2010.

[126] Hiroaki Misonou, Durga P Mohapatra, and James S Trimmer. Kv2.1: a voltage-gated k+ channel critical to dynamic control of neuronal excitability. *Neurotoxicology*, 26(5):743–52, October 2005.

[127] Tsugumichi Miyasho, Hiroshi Takagi, Hideo Suzuki, Shigeo Watanabe, Masashi Inoue, Yoshihisa Kudo, and Hiroyoshi Miyakawa. Low-threshold potassium channels and a low-threshold calcium channel regulate ca2+ spike firing in the dendrites of cerebellar purkinje neurons: a modeling study. *Brain Research*, 891(1–2):106 – 115, 2001.

[128] Aliakmal Momin, Hervé Cadiou, Adrian Mason, and Peter A. McNaughton. Role of the hyperpolarization-activated current ih in somatosensory neurons. *The Journal of Physiology*, 586(24):5911–5929, 2008.

[129] Pablo Monzón and Juan Piquinela. *Sistemas lineales en régimen permanente.* 2012.

[130] Philippe Morquette, Raphaël Lavoie, Mitch-David Fhima, Xavier Lamoureux, Dorly Verdier, and Arlette Kolta. Generation of the masticatory central pattern and its modulation by sensory feedback. *Progress in neurobiology*, 96(3):340–55, March 2012.

[131] Catherine Morris and Harold Lecar. Voltage oscillations in the barnacle giant muscle fiber. *Biophysical Journal*, 35:193–213, 1981.

[132] Farzan Nadim, ØysteinH. Olsen, Erik Schutter, and RonaldL. Calabrese. Modeling the leech heartbeat elemental oscillator i. interactions of intrinsic and synaptic currents. *Journal of Computational Neuroscience*, 2(3):215–235, 1995.

[133] C.A.D. Negro and S.H. Chandler. Physiological and theoretical analysis of K+ currents controlling discharge in neonatal rat mesencephalic trigeminal neurons. *Journal of Neurophysiology*, 77(2):537–553, 1997.

Bibliography

[134] Jorge Nocedal and Stephen J. Wright. *Numerical Optimization.* Springer Series in Operations Research and Financial Engineering. Springer New York, 2006.

[135] Patricio Orio and Daniel Soudry. Simple, fast and accurate implementation of the diffusion approximation algorithm for stochastic ion channels with multiple states. *PLoS ONE*, 7(5):e36670, 05 2012.

[136] Srdjan Ostojic, Nicolas Brunel, and Vincent Hakim. Synchronization properties of networks of electrically coupled neurons in the presence of noise and heterogeneities. *Journal of computational neuroscience*, 26(3):369–92, June 2009.

[137] Philip Parker, Scott Cruikshank, and Barry W. Connors. Stability of electrical coupling despite massive developmental changes of intrinsic neuronal physiology. *The Journal of Neuroscience*, 29(31):9761–9770, 2009.

[138] Cristina M. Pedroarena, Inés E. Pose, Jack Yamuy, Michael H. Chase, and Francisco R. Morales. Oscillatory membrane potential activity in the soma of a primary afferent neuron. *Journal of Neurophysiology*, 82(3):1465–1476, 1999.

[139] Benjamin Pfeuty, Germán Mato, David Golomb, and David Hansel. Electrical synapses and synchrony: the role of intrinsic currents. *The Journal of Neuroscience*, 23(15):6280–94, July 2003.

[140] Inés Pose, Sharon Sampogna, Michael H. Chase, and Francisco R. Morales. Mesencephalic trigeminal neurons are innervated by nitric oxide synthase-containing fibers and respond to nitric oxide. *Brain Research*, 960(1–2):81 – 89, 2003.

[141] Steven A. Prescott, Stéphanie Ratté, Yves De Koninck, and Terrence J. Sejnowski. Pyramidal neurons switch from integrators in vitro to resonators under in vivo-like conditions. *Journal of Neurophysiology*, 100(6):3030–3042, 2008.

[142] Astrid A. Prinz. Neuronal parameter optimization. *Scholarpedia*, 2(1):1903, 2007.

[143] Astrid A. Prinz, Cyrus P. Billimoria, and Eve Marder. Alternative to hand-tuning conductance-based models: Construction and analysis of databases of model neurons. *Journal of Neurophysiology*, 90(6):3998–4015, 2003.

[144] E. Puil, B. Gimbarzevsky, and R. M. Miura. Quantification of membrane properties of trigeminal root ganglion neurons in guinea pigs. *Journal of Neurophysiology*, 55(5):995–1016, 1986.

[145] Purves et al, editor. *Neuroscience.* Sinauer Associates, 3 edition, 2004.

[146] Indira M Raman and Bruce P Bean. Resurgent sodium current and action potential formation in dissociated cerebellar Purkinje neurons. *The Journal of neuroscience : the official journal of the Society for Neuroscience*, 17(12):4517–26, June 1997.

[147] Indira M Raman and Bruce P Bean. Ionic currents underlying spontaneous action potentials in isolated cerebellar Purkinje neurons. *The Journal of neuroscience : the official journal of the Society for Neuroscience*, 19(5):1663–74, March 1999.

[148] Indira M Raman and Bruce P Bean. Inactivation and recovery of sodium currents in cerebellar Purkinje neurons: evidence for two mechanisms. *Biophysical journal*, 80(2):729–37, February 2001.

[149] Lorena Rela and Lidia Szczupak. Gap junctions. *Molecular Neurobiology*, 30(3):341–357, 2004.

[150] Kenneth L. Rice, M.A. Bhuiyan, T.M. Taha, Christopher N. Vutsinas, and M.C. Smith. Fpga implementation of izhikevich spiking neural networks for character recognition. In *Reconfigurable Computing and FPGAs, 2009. ReConFig '09. International Conference on*, pages 451–456, 2009.

[151] J T Rokx and J D van Willigen. Organization of neuronal clusters in the mesencephalic trigeminal nucleus of the rat: fluorescent tracing of temporalis and masseteric primary afferents. *Neuroscience letters*, 86(1):21–26, March 1988.

[152] Arnd Roth and Armin Bahl. Divide et impera: optimizing compartmental models of neurons step by step. *Journal of Physiology*, 587:1369–1370, 2009.

[153] Brad S Rothberg and Karl L Magleby. Testing for detailed balance (microscopic reversibility) in ion channel gating. *Biophysical Journal*, 80(6):3025–3026, 2001.

[154] Yoram Rudy and Jonathan R. Silva. Computational biology in the study of cardiac ion channels and cell electrophysiology. *Quarterly Reviews of Biophysics*, 39:57–116, 2 2006.

[155] Ilya a Rybak, Krzysztof Ptak, Natalia a Shevtsova, and Donald R McCrimmon. Sodium currents in neurons from the rostroventrolateral medulla of the rat. *Journal of Neurophysiology*, 90(3):1635–42, September 2003.

[156] Mitsuru Saito, Yoshinaka Murai, Hajime Sato, Yong-Chul Bae, Tadashi Akaike, Masahiko Takada, and Youngnam Kang. Two opposing roles of 4-AP-sensitive K+ current in initiation and invasion of spikes in rat mesencephalic trigeminal neurons. *Journal of Neurophysiology*, 96(4):1887–901, October 2006.

Bibliography

[157] Y. Shigenaga, Y. Mitsuhiro, A. Yoshida, C. Q. Cao, and H. Tsuru. Morphology of single mesencephalic trigeminal neurons innervating masseter muscle of the cat. *Brain research*, 445(2):392–9, April 1988.

[158] Y Shigenaga, A. Yoshida, Y. Mitsuhiro, K. Doe, and S. Suemune. Morphology of single mesencephalic trigeminal neurons innervating periodontal ligament of the cat. *Brain research*, 448(2):331–8, May 1988.

[159] Masayoshi Shirasu, Takeshi Takahashi, Toshiharu Yamamoto, Kazuo Itoh, Sadao Sato, and Hiroyuki Nakamura. Direct projections from the central amygdaloid nucleus to the mesencephalic trigeminal nucleus in rats. *Brain research*, 1400:19–30, July 2011.

[160] George J. Siegel, editor. *Basic Neurochemistry*. Elsevier Academic Press, 7th edition edition, 2006.

[161] Jonathan R. Silva, Hua Pan, Dick Wu, Ali Nekouzadeh, Keith F. Decker, Jianmin Cui, Nathan A. Baker, David Sept, and Yoram Rudy. A multiscale model linking ion-channel molecular dynamics and electrostatics to the cardiac action potential. *Proceedings of the National Academy of Sciences*, 106(27):11102–11106, 2009.

[162] Frances Skinner, Gina Turrigiano, and Eve Marder. Frequency and burst duration in oscillating neurons and two-cell networks. *Biological Cybernetics*, 69(5-6):375–383, 1993.

[163] Roy M Smeal, G Bard Ermentrout, and John a White. Phase-response curves and synchronized neural networks. *Philosophical transactions of the Royal Society of London. Series B, Biological sciences*, 365(1551):2407–22, August 2010.

[164] Cristina Soto-Treviño, Pascale Rabbah, Eve Marder, and Farzan Nadim. Computational model of electrically coupled, intrinsically distinct pacemaker neurons. *Journal of Neurophysiology*, 94(1):590–604, 2005.

[165] David Sterratt, Bruce Graham, Andrew Gillies, and David Willshaw. *Principles of Computational Modelling in Neuroscience*. Cambridge University Press, 2011.

[166] Volker Steuber, NathanW. Schultheiss, R.Angus Silver, Erik Schutter, and Dieter Jaeger. Determinants of synaptic integration and heterogeneity in rebound firing explored with data-driven models of deep cerebellar nucleus cells. *Journal of Computational Neuroscience*, 30(3):633–658, 2011.

[167] Adam F. Strassberg and Louis J. DeFelice. Limitations of the hodgkin-huxley formalism: Effects of single channel kinetics on transmembrane voltage dynamics. *Neural Computation*, 5:843–855, 1993.

[168] Carl-Magnus Svensson, Stephen Coombes, and Jonathan Westley Peirce. Using evolutionary algorithms for fitting high-dimensional models to neuronal data. *Neuroinformatics*, 10(2):199–218, 2012.

[169] Torsten Söderström and Petre Stoica. *System Identification*. Prentice Hall, 2001.

[170] Susumu Tanaka, Nanping Wu, Chie-Fang Hsaio, Jack Turman, and Scott H Chandler. Development of inward rectification and control of membrane excitability in mesencephalic v neurons. *Journal of Neurophysiology*, 89(3):1288–98, March 2003.

[171] Adam L. Taylor, Timothy J. Hickey, Astrid A. Prinz, and Eve Marder. Structure and visualization of high-dimensional conductance spaces. *Journal of Neurophysiology*, 96(2):891–905, 2006.

[172] S.H. Thompson. Three pharmacologically distinct potassium channels in molluscan neurones. *The Journal of Physiology*, 265(2):465–488, 1977.

[173] W Van Geit, E De Schutter, and P Achard. Automated neuron model optimization techniques: a review. *Biological cybernetics*, 99(4-5):241–51, November 2008.

[174] Werner Van Geit, Pablo Achard, and Erik De Schutter. Neurofitter: a parameter tuning package for a wide range of electrophysiological neuron models. *Frontiers in Neuroinformatics*, 1(1), 2007.

[175] Marie Vandecasteele, Jacques Glowinski, and Laurent Venance. Electrical synapses between dopaminergic neurons of the substantia nigra pars compacta. *The Journal of Neuroscience*, 25(2):291–298, 2005.

[176] Stefania Vecchietti, Ilaria Rivolta, Stefano Severi, Carlo Napolitano, SilviaG. Priori, and Silvio Cavalcanti. Computer simulation of wild-type and mutant human cardiac na+ current. *Medical and Biological Engineering and Computing*, 44(1-2):35–44, 2006.

[177] Martin Vejmelka, Ingo Fründ, and Ajay Pillai. Traversing scales: Large scale simulation of the cat cortex using single neuron models. In Peterbeim Graben, Changsong Zhou, Marco Thiel, and Jürgen Kurths, editors, *Lectures in Supercomputational Neurosciences*, Understanding Complex Systems, pages 331–342. Springer Berlin Heidelberg, 2008.

[178] Dorly Verdier, James P Lund, and Arlette Kolta. Synaptic inputs to trigeminal primary afferent neurons cause firing and modulate intrinsic oscillatory activity. *Journal of Neurophysiology*, 92(4):2444–55, October 2004.

[179] Margaret L. Veruki and Espen Hartveit. Aii (rod) amacrine cells form a network of electrically coupled interneurons in the mammalian retina. *Neuron*, 33(6):935–946, 2002.

Bibliography

[180] Koen Vervaeke, Andrea Lorincz, Padraig Gleeson, Matteo Farinella, Zoltan Nusser, and R Angus Silver. Rapid desynchronization of an electrically coupled interneuron network with sparse excitatory synaptic input. *Neuron*, 67(3):435–51, August 2010.

[181] C. Wahl-Schott and M. Biel. Hcn channels: Structure, cellular regulation and physiological function. *Cellular and Molecular Life Sciences*, 66(3):470–494, 2009.

[182] Phil M.E. Waite and Ken W.S. Ashwell. Chapter 29 - trigeminal sensory system. In George Paxinos and Jürgen K. Mai, editors, *The Human Nervous System (Second edition)*, pages 1093 – 1124. Academic Press, San Diego, second edition edition, 2004.

[183] Chong Wang, P. Beyerlein, H. Pospisil, A. Krause, C. Nugent, and W. Dubitzky. An efficient method for modeling kinetic behavior of channel proteins in cardiomyocytes. *Computational Biology and Bioinformatics, IEEE/ACM Transactions on*, 9(1):40–51, 2012.

[184] Lu-Yang Wang, Li Gan, Ian D. Forsythe, and Leonard K. Kaczmarek. Contribution of the kv3.1 potassium channel to high-frequency firing in mouse auditory neurones. *The Journal of Physiology*, 509(1):183–194, 1998.

[185] N Wu, C F Hsiao, and S H Chandler. Membrane resonance and subthreshold membrane oscillations in mesencephalic V neurons: participants in burst generation. *The Journal of Neuroscience : the official journal of the Society for Neuroscience*, 21(11):3729–39, June 2001.

[186] Nanping Wu, Akifumi Enomoto, Susumu Tanaka, Chie-Fang Hsiao, Duane Q Nykamp, Eugene Izhikevich, and Scott H Chandler. Persistent sodium currents in mesencephalic v neurons participate in burst generation and control of membrane excitability. *Journal of Neurophysiology*, 93(5):2710–22, May 2005.

[187] RL Wu and ME Barish. Two pharmacologically and kinetically distinct transient potassium currents in cultured embryonic mouse hippocampal neurons. *The Journal of Neuroscience*, 12(6):2235–2246, 1992.

[188] J Yang, J-L Xing, N-P Wu, Y-H Liu, C-Z Zhang, F Kuang, V-Z Han, and S-J Hu. Membrane current-based mechanisms for excitability transitions in neurons of the rat mesencephalic trigeminal nuclei. *Neuroscience*, 163(3):799–810, October 2009.

[189] Y Yokomizo, Y Murai, E Tanaka, H Inokuchi, J Kusukawa, and H Higashi. Excitatory GABAergic synaptic potentials in the mesencephalic trigeminal nucleus of adult rat in vitro. *Neuroscience research*, 51(4):463–74, April 2005.

[190] Bo Zhang, Xiao-Yu Zhang, Pi-Fu Luo, Wei Huang, Fei-Peng Zhu, Tao Liu, Yi-Ru Du, Qi-Hui Wu, Jin Lü, Yun Xiu, Li-Na Liu, Hong-Ping Huang, Shu Guo, Hui Zheng, Claire Xi Zhang, and Zhuan Zhou. Action potential-triggered somatic exocytosis in mesencephalic trigeminal nucleus neurons in rat brain slices. *The Journal of Physiology*, 590(4):753–762, 2012.

[191] Y Zhao, S Inayat, D A Dikin, R S Ruoff, and J B Troy. Impedance characterization and modelling of an improved patch clamp device. *Proceedings of the Institution of Mechanical Engineers, Part N: Journal of Nanoengineering and Nanosystems*, 223(3-4):121–131, 2009.

[192] Eric A. Zilli and Michael E. Hasselmo. Coupled noisy spiking neurons as velocity-controlled oscillators in a model of grid cell spatial firing. *The Journal of Neuroscience : the official journal of the Society for Neuroscience*, 30(41):13850 –13860, 2010.

This page has been intentionally left blank

List of Tables

This page has been intentionally left blank

List of Figures

List of Figures

Esta es la última página.
Compilado el Tuesday 4$^{\text{th}}$ March, 2014.
http://iie.fing.edu.uy/